University of Arkansas, Fayetteville
ScholarWorks@UARK

Theses and Dissertations

8-2014

Effects of Nanoholes Grown by Molecular Beam Droplet Epitaxy on Electrical Properties of Two Dimensional Electron Gas

Yusuke Hirono
University of Arkansas, Fayetteville

Follow this and additional works at: http://scholarworks.uark.edu/etd

Recommended Citation
Hirono, Yusuke, "Effects of Nanoholes Grown by Molecular Beam Droplet Epitaxy on Electrical Properties of Two Dimensional Electron Gas" (2014). *Theses and Dissertations*. 2143.
http://scholarworks.uark.edu/etd/2143

This Thesis is brought to you for free and open access by ScholarWorks@UARK. It has been accepted for inclusion in Theses and Dissertations by an authorized administrator of ScholarWorks@UARK. For more information, please contact scholar@uark.edu, ccmiddle@uark.edu.

Effects of Nanoholes Grown by Molecular Beam Droplet Epitaxy on Electrical Properties of Two Dimensional Electron Gas

Effects of Nanoholes Grown by Molecular Beam Droplet Epitaxy on Electrical Properties of Two Dimensional Electron Gas

A thesis submitted in partial fulfillment
of the requirements for the degree of
Master of Science in Physics

By

Yusuke Hirono
University of Arkansas
Bachelor of Science in Physics, 2011
University of Arkansas
Bachelor of Science in Mathematics, 2011

August 2014
University of Arkansas

This thesis is approved for recommendation to the Graduate Council.

Dr. Gregory J. Salamo
Thesis Director

Dr. Reeta Vyas
Committee Member

Dr. William F. Oliver III
Committee Member

Abstract

The effects of nanoholes, grown by molecular beam droplet epitaxy, on the electrical properties of quantum well (QW) heterostructures are reported. To investigate how the depth of nanoholes affect the electrical properties of the QW heterostructures, the growth conditions for nanoholes were optimized with respect to their depth and density. Using the results of the optimization of the nanohole growth, three InGaAs pseudomorphic quantum wells with nanoholes were investigated with varied depth and a constant density. A QW heterostructure without nanoholes was grown as a reference structure. For all the samples, temperature dependent Hall effect measurements, noise studies as a function of both bias and temperature, and temperature dependent current-voltage (I-V) measurements have been carried out to examine the effects of nanoholes on the QW heterostructures. The Hall effect measurements revealed clear correlation between the depth of the nanoholes and the electrical characteristics of the QW systems such as Hall mobility and sheet electron density. Besides an increase in the mobility and carrier density, the nanoholes lead to a significant reduction of 1/f noise due to a decrease in the Hooge parameter, which can be advantageous for the fabrication of high performance electronic devices. In addition, it was shown that the nanoholes change the energy spectrum of the QW heterostructures which affects carrier transport in the QWs and metal-semiconductor interface. The changes of the energy spectrum were clued in by the variation of carrier activation energy, appearance of a new deep state in the band gap of an AlGaAs barrier layer that affect carrier kinetics and fluctuation phenomena in the present material system. The results of this thesis show a potential of nanoholes grown by droplet epitaxy as a promising candidate for modulation of material properties and fabrication of advanced material systems for electronic and optoelectronic application.

©2014 by Yusuke Hirono
All Rights Reserved

Acknowledgements

First of all, I would like to express my special gratitude to my thesis advisor, Dr. Gregory J. Salamo, who has always been supporting and encouraging me throughout my research. His passion and attitude toward science has always motivated me to work hard and think carefully. Without his guidance and support, I would not have been able to complete my thesis research. I hope that our work together over the last five years has been enjoyable. I would like to thank Dr. Reeta Vyas and Dr. William Oliver for serving on my committee.

My special thanks goes to Dr. Vasyl Kunets who has helped me conduct experiments, analyze data, and develop my understanding of MBE and electrical characterization. I am especially grateful for his willingness to help students conduct research and share his knowledge and experience. I would like to show my appreciation to Dr. Yuriy Mazur for encouraging and motivating me to work hard. His jokes have made my life so much fun. I am also grateful to Dr. Morgan Ware for his valuable advice in my research.

I would like to thank my colleagues for fruitful conversations regarding our research the names of which include, but are not limited to, Colin Furrow, Tim Morgan, Xian Hu, Paul Minor, Thomas White, Chen Li, and Sabina Koukourinkova. I wish them all the best in the future.

I am also thankful for my parents who always supported me and gave me such a great opportunity to study abroad in the United States. I feel very fortunate to study in a wonderful environment and join one of the best research groups in the world. Last, but not least, I am obliged to those who supported me in any aspect of my life at the University of Arkansas.

Table of Contents

Abstract ....

Acknowledgements ....

Table of Contents ....

List of Figures ....

List of Tables ....

List of Symbols ....

List of Abbreviations and Acronyms ....

Chapter 1: Introduction 1

Chapter 2: Growth 5

2.1. MBE 5

2.1.1. Principles 5

2.1.2. Experimental Setup 11

2.2. Droplet Epitaxy 13

2.3. Sample Description 17

2.3.1. Optimization of Nanoholes 17

2.3.2. QWs with Nanoholes 19

Chapter 3: Morphology Characterization 22

3.1. Atomic Force Microscopy 22

3.2. Results and Analysis 24

3.2.1. Optimization of Nanohole Growth 24

3.2.2. Nanoholes on QW 25

Chapter 4: Electrical Characterization 29

4.1. Fabrication ... 29
4.1.1. Principles of Photolithography ... 29
4.1.2. Metal-Semiconductor Contact ... 30
4.1.3. Experimental Setup and General Fabrication Procedure ... 32
4.2. Hall Effect Measurements ... 36
4.2.1. Theory ... 36
4.2.2. Experimental Setup ... 39
4.2.3. Results and Analysis ... 41
4.3. Noise ... 45
4.3.1. Theory ... 45
4.3.2. Experimental Setup ... 50
4.3.3. Results and Analysis ... 54
4.4. Current-Voltage Measurements ... 65
4.4.1. Theory ... 65
4.4.2. Experimental Setup ... 69
4.4.3. Results and Analysis ... 70
Chapter 5: Conclusion ... 75
Chapter 6: References ... 79

List of Figures

FIG. 2.1. Top down schematic of a typical MBE growth chamber [21]. 6

FIG. 2.2. Schematic of a typical effusion cell [21]. 7

FIG. 2.3. Schematic of a typical As valved cracker cell [21]. 8

FIG. 2.4. Three possible epitaxial growth modes at different coverage. (a) Layer by layer Frank-van de Merwe mode, (b) island and layer Stranski-Krastanov mode, and (c) island Volmer-Weber mode [41]. 9

FIG. 2.5. (a)-(e) Different stage of the Frank van der Merwe growth and (f) corresponding RHEED intensity oscillation [21]. 10

FIG. 2.6. Riber 32P MBE chamber. 12

FIG. 2.7. Schematic of etching process (a) just after droplet deposition, (b) at the beginning of etching , and (c) in the middle of etching [64]. 16

FIG. 2.8. Schematics of reference InGaAs QW. The doping density of the doped AlGaAs barrier is $2.4\times10^{18}cm^{-3}$. 20

FIG. 2.9. Calculated band diagrams of reference QW, SF120. E_C, E_V, E_F, E_{e1}, E_{e2}, and E_{hh1} represent the conduction band, valence band, Fermi energy, ground state for electrons, 1st exited state for electrons, and ground state for heavy holes, respectively. Ψ_{e1}, Ψ_{e2}, and Ψ_{hh1} show corresponding wave functions (a) both conduction and valence bands (b) only conduction band. 21

FIG. 3.1. SEM picture of a probe (a) sharp tip, (b) top-view, and (c) side view (ACTA model from App Nano) [86]. 22

FIG. 3.2. Schematic of basic AFM operation principle in the tapping mode [85]. 23

FIG. 3.3. (a) Density and (b) depth of nanoholes grown at different temperatures as a function of Ga coverage........ 25

FIG. 3.4. AFM pictures and line profiles of (a) and (b) SF121 (30ML), (c) and (d) SF122 (60ML), and (e) and (f) SF123 (90ML). The size of pictures is 2μm×2μm. 28

FIG. 4.1. Schematics of general photolithography (a) during exposure, and after development by using (b) positive photoresist and (c) negative photoresist........ 29

FIG. 4.2. (a) A SEM picture and (b) schematic of TLM structure. (c) The expected total resistance between two contacts of TLM structure as a function of contact-spacing, d_i........ 31

FIG. 4.3. Contact resistance as a function of (a) annealing temperature and (b) annealing time. 35

FIG. 4.4. Schematic of Hall effect measurement configuration. 36

FIG. 4.5. Hall effect measurement setup. Samples were placed between the electromagnets and parallel to the magnet poles so that the magnetic field was perpendicular to the surface of the samples........ 40

FIG. 4.6. (a) Hall mobility and (b) sheet carrier density of SF120, SF121, SF122, and SF123... 41

FIG. 4.7. (a) Arrhenius plots for SF120, SF121, SF122, and SF123 above 200K, and (b) activation energy of carriers as a function of Ga coverage for nanohole growth. Each straight line in (a) is a linier fitting to each carrier density curve. The Ga coverage of 0ML corresponds to SF120 in (b)........ 43

FIG. 4.8. Two different representation of noise data as a function of (a) frequency and (b) temperature [136]........ 47

FIG. 4.9. Setup for noise studies and SEM pictures of Greek Cross structure........ 50

FIG. 4.10. Room temperature noise spectra for (a) SF120, (b) SF121, (c) SF122, and (d) SF123 with different applied voltages. R_L is the resistance of a load resistor, V_S is the voltage applied to the sample, and V_B is the voltage of the DC battery. 54

FIG. 4.11. Noise spectra and their fitting functions for (a) SF120, (b) SF121, (c) SF122, and (d) SF123. The black solid line is experimental data, red solid line is fitting function. The dash lines represent the noise spectra of 1/f, 1st GR, 2nd GR, and thermal noise of the fitting function for dark blue, light pink, dark pink and light blue, respectively. The load resistor is 82kΩ for all samples. 55

FIG. 4.12. Plots of A as a function of V_S^2 with linear fitting lines for (a) SF120, (b) SF121, (c) SF122, and (d) SF123. Based on the slopes of the liner fitting lines and the results of the Hall effect measurements, the Hooge parameters were calculated. 57

FIG. 4.13. Hooge parameters as a function of Ga coverage for the growth of nanohole growth. The Ga coverage of 0ML corresponds to SF120 58

FIG. 4.14. Relative noise spectra as a function of temperature at different frequencies of (a) SF120, (b) SF121, (c) SF122, and (d) SF123. The straight lines are guides to the eyes only. Numbers labeled on each peak correspond the name of peak. 59

FIG. 4.15. (a) S_{Max} and (b) $1/k_BT_{Max}$ of SF120 for all four peaks as a function of angular frequency in log-log scale and linear-log scale, respectively. Lines are linear fits for each data set. 61

FIG. 4.16. (a) S_{Max} and (b) $1/k_BT_{Max}$ of SF121 for all four peaks as a function of angular frequency in log-log scale and linear-log scale, respectively. Lines are linear fits for each data set. 61

FIG. 4.17. (a) S_{Max} and (b) $1/k_BT_{Max}$ of SF122 for all four peaks as a function of angular frequency in log-log scale and linear-log scale, respectively. Lines are linear fits for each data set. 62

FIG. 4.18. (a) S_{Max} and (b) $1/k_BT_{Max}$ of SF123 for all four peaks as a function of angular frequency in log-log scale and linear-log scale, respectively. Lines are linear fits for each data set. ... 62

FIG. 4.19. E_1 for all peaks as a function of Ga coverage for the nanohole growth. 64

FIG. 4.20. Formation of a barrier between an n-type semiconductor and a metal (a) before and (b) after contact. E_C, E_V, and E_F are the energy levels of the conduction band minimum, the valence band maximum, and Fermi energy. 66

FIG. 4.21. Three transport mechanisms in a forward biased Schottky contact. (a) Thermionic emission, (b) thermionic-field emission, and (c) filed emission. Black dots represent electrons. 67

FIG. 4.22. A SEM picture of a typical circular diode structure. 69

FIG. 4.23. I-V characteristics of SF120, SF121, SF122, and SF123 (a) in both forward and reverse bias and (b) forward bias between 0V to 0.5V. Straight lines are linear fits to each data set between 0.15V and 0.35V. 71

FIG. 4.24. Richardson plots with fitting curves of (a) SF120, (b) SF121, (c) SF122, and (d) SF123. 73

List of Tables

TABLE 3.1. Dimension of nanoholes of all samples. 26

TABLE 4.1. Details of lithography to fabricate Greek Cross structures for noise measurements. 51

TABLE 4.2. Summary of slopes of S_{Max} and $1/k_BT_{Max}$ plots and E_1 for all samples and all peaks. 63

TABLE 4.3. Details of lithography to fabricate circular diode structures for I-V measurements.70

TABLE 4.4. Fitting parameters for all samples. 74

List of Symbols

A	Amplitude of 1/f Noise
A^*	Effective Richardson Constant
A_C	Area of Contact
A_S	Active Area of Device
B_i	Amplitude of ith Generation Recombination Noise
B_z	z Component of Magnetic Field
C_{TE}	Arbitrary Constant for Thermionic Current
C_{TFE}	Arbitrary Constant for Thermionic-Field Current
d_i	Spacing Between Contacts of TLM Structure
$\vec{E}$	Electric Field
E_0	Energy Level Position of Deep Level with respect to Fermi Level
E_1	Emission Activation Energy of Capture Cross Section
E_A	Activation Energy of Carriers
E_x	x Component of Electric Field
E_y	y Component of Electric Field
f	Frequency
fi	Corner Frequency of ith Generation Recombination Noise
g	Degeneracy Factor
h	Planck Constant
$\hbar$	Reduced Planck Constant
I_{TE}	Current due to Thermionic Emission
I_{TFE}	Current due to Thermionic-Field Emission

I_S	Saturation Current
$I_{S,\,TE}$	Saturation Current due to Thermionic Emission
$I_{S,\,TFE}$	Saturation Current due to Thermionic-Field Emission
I_y	Current in the *y*-direction
j_y	*y* Component of Current Density
k_B	Boltzmann Constant
l	Distance between Two Contacts
m_0	Free Electron Mass
m^*	Effective Electron Mass in Semiconductor
n	Electron Density
n	Ideality Factor
n_{2D}	Sheet Electron Density
n_i	Intrinsic Carrier Concentration
N	Total Number of Carriers in Device
N_a	Acceptor Density
N_C	Effective Density of States in Conduction Band
N_d	Donor Density
N_t	Trap Density
p	Hole Density
q	Electron Charge
R	Resistance
R_C	Contact Resistance
R_H	Hall Coefficient

R_L Resistance of Load Resistor

r_S Sheet Resistance of Semiconductor

S Relative Noise Spectral Density

S_{Max} Relative Noise Spectral Density Peak Value

S_V Noise Spectral Density in Voltage

$S_{V,\ 1/f}$ Noise Spectral Density in Voltage by 1/f Noise

$S_{V,\ i,\ GR}$ Noise Spectral Density in Voltage by i^{th} GR Noise

$S_{V,\ Th}$ Noise Spectral Density in Voltage by Thermal Noise

t Thickness of Samples

T Temperature

T_{Max} Temperature of Relative Noise Spectral Density Peak

$\vec{v}$ Drift Velocity

v_y Drift Velocity in the y-direction

V Sample Volume

V Voltage

V_{bi} Schottky Barrier for Electrons in Semiconductor

V_C Voltage Across Two Contacts Parallel to Current

V_H Hall Voltage

V_S Voltage Applied to Sample

w Width of Sample

α Hooge Parameter

ε_S Permittivity of Semiconductor

μ Mobility

σ	Electron Capture Cross Section
σ_0	Pre-exponential Factor for Electron Capture Cross Section
τ	Time Constant of Trap Center
τ_c	Capture Time Constant of Trap Center
τ_{c0}	Pre-exponential Factor for Capture Time Constant of Trap Center
τ_e	Emission Time Constant of Trap Center
ϕ_B	Schottky Barrier Height with respect to Fermi Energy of Metal
ϕ_m	Work Function of Metal
ϕ_S	Work Function of Semiconductor
χ_S	Electron Affinity of Semiconductor
ω	Angular Frequency

List of Abbreviations and Acronyms

2D	Two Dimensional
2DEG	Two Dimensional Electron Gas
3D	Three Dimensional
AFM	Atomic Force Microscopy
Al	Aluminum
AlGaAs	Aluminum Gallium Arsenide
As	Arsenic
$AsBr_3$	Arsenic Tribromide
Be	Beryllium
BEP	Beam Equivalent Pressure
DI	Deionized
DLNS	Deep Level Noise Spectroscopy
DLTS	Deep Level Transient Spectroscopy
FFT	Fast Fourier Transformation
FM	Frank-van der Merwe
Ga	Gallium
GaAs	Gallium Arsenide
GR	Generation-Recombination
I-V	Current-Voltage
IC	Integrated Circuit
In	Indium
InAs	Indium Arsenide

InGaAs	Indium Gallium Arsenide
IPA	Isopropyl Alcohol
MBE	Molecular Beam Epitaxy
ML	Monolayer
P	Phosphorus
PID	Proportional-Integral-Derivative
UHV	Ultra-High Vacuum
UV	Ultra Violet
QD	Quantum Dot
QR	Quantum Ring
QW	Quantum Well
RHEED	Reflection High Energy Electron Diffraction
SEM	Scanning Electron Microscopy
Si	Silicon
SK	Stranski-Krastanov
SPM	Scanning Probe Microscopy
TEM	Transmission Electron Microscopy
TLM	Transmission Line Model
VW	Volmer-Weber

Chapter 1: Introduction

Since the invention of the transistor by Bardeen and Brattain in 1947 [1,2], many different semiconductor devices have been invented and developed at an astonishing pace. The invention of the Integrated Circuits (ICs), which are an assembly of several billion transistors in a single device, changed the world literally [3] since ICs are one of the most fundamental building blocks in today's world. In addition to ICs, optoelectronic semiconductor devices, such as laser diodes and light-emitting diode, have been achieved and applied in a wide range of uses [4,5].

To fabricate semiconductor devices, one should modulate properties of semiconductors so that the devices work as they are designed. The most fundamental and popular way to modulate the properties of semiconductors is impurity doping. Intrinsic semiconductors are usually a poor conductor and not useful for devices. However, modification of both type and number of carriers is possible by providing impurities called dopants to intrinsic semiconductors [6,7]. For example, if silicon (Si) is doped by arsenic (As), some As atoms will replace some Si atoms in the crystal structures. Since an As atom has five valence electrons while an Si atom has four electrons, an extra electron is easily donated to the conduction band, and Si becomes n-type. On the other hand, if Si is doped by boron, each atom of which has three valence electrons, a hole can be generated easily, and Si becomes p-type. In these cases, each dopant atom creates one free electron or hole, and thus, by controlling the number of dopants, one can control the number of carriers.

Besides impurity doping, nanostructures have been introduced into material systems to modulate their properties. Thanks to the development of sophisticated growth techniques, the fabrication of nano-scale structure is now possible. For example, quantum dots (QDs) have been

widely used for optoelectronic device application [8–10]. When electrons are confined in a material whose dimension is close to their Bloch wavelength, their energy is not continuous anymore and consists of discrete levels. Therefore, the transition energy between the conduction band and valence band is larger than its band gap. Moreover, a quantum well (QW) is used to modulate the mobility of carriers for high electron mobility transistors [11,12].

In addition to QDs and QWs, nanoholes have recently received much attention for site controlled growth and fabrication of complex three dimensional (3D) nanostructures. Several growth methods have been proposed to fabricate nano-scale holes on the surface of substrates. For example, nanoholes were fabricated by preferential etching of indium arsenide (InAs) QDs which are partially capped by gallium arsenide (GaAs) using arsenic tribromide ($AsBr_3$) as an etchant gas [13]. Recently, Wang *et al.* reported the fabrication of nanoholes by droplet epitaxy [14]. In his growth protocol, gallium (Ga) droplets were formed on GaAs substrates by supplying Ga without As. Then, these Ga droplets were crystalized by exposing them to an As flux. During the crystallization, As atoms in the substrate dissolve into the Ga droplets, and the nanoholes were formed below the droplets. This nano-scale drilling effect has been observed by using aluminum (Al) [15], AlGa [16], and indium (In) droplets [17].

For these previous studies, nanoholes have been mainly used as a template for subsequent growth of QDs because it is easier to control the density of nanoholes. For example, Heyn *et al.* achieved the growth of strain-free GaAs QDs by filling nanoholes on aluminum gallium arsenide (AlGaAs) substrates with overgrowth of GaAs [18]. Moreover, by growing InAs on a substrate with nanoholes, InAs QDs were formed inside the nanoholes. Hence, the density of QDs can be more easily controlled by first growing the desired density of nanoholes [19]. Furthermore, an

increase of the InAs coverage leads to the formation of InAs QD clusters around the nanoholes [20].

Although nanoholes as templates are a promising way to control the dimension of QDs and fabricate complex nanostructures, effects of nanoholes themselves on material properties have not been explored. Similar to other nanostructures, nanoholes can be expected to exhibit new effects on the properties of materials. Moreover, even for the application of nanoholes as templates, it is quite important to understand how nanoholes affect material properties to differentiate the effect of the nanoholes and other nanostructures grown using the nanoholes as templates. Therefore, this thesis investigated the effects of nanoholes on electrical properties of a two dimensional electron gas (2DEG) and QW heterostructures and proposed using nanoholes as a new way to modulate the properties of semiconductors.

To explore the effects of nanoholes, samples were grown by molecular beam epitaxy (MBE), and their electrical properties were investigated. In Chapter 2, the principles and experimental setup of MBE are explained as well as growth details of samples. A set of samples consist of four indium gallium arsenide (InGaAs) QWs with and without nanoholes. To study the effects of nanoholes in a consistent way, the growth conditions of nanoholes were optimized. The results of the optimization are applied to the growth of the QWs with nanoholes so that the nanoholes on the QWs have different depth but similar density. The surface morphology of all samples grown by MBE is examined in Chapter 3. This chapter starts with the results of the optimization of the nanohole growth and focuses on the analysis of dimensions of nanoholes grown on the surface of the QWs by atomic force microscopy (AFM). Chapter 4 focuses on electrical characterization such as Hall effect measurements, noise studies ,and current voltage characteristics. Photolithography was used to prepare samples for electrical characterization, and

thus, the detail of the fabrication is also described in this chapter. The theoretical background and experimental setup of each electrical characterization technique is discussed, and the experimental results are analyzed subsequently. Finally, Chapter 5 concludes this thesis with a brief review of the experimental results and analysis as well as future work to investigate in detail the physics behind the effects of nanoholes.

Chapter 2: Growth

2.1. MBE

2.1.1. Principles

Molecular beam epitaxy (MBE) is an epitaxial crystal growth technique under ultra-high vacuum (UHV), in which source materials are used to form either atomic or molecular beams with a long mean free path [21–25]. These atomic or molecular beams impinge on the surface of heated substrates, and adsorbed atoms migrate on the surface to lattice sites and are incorporated into the crystal. Since its invention by J. R. Arthur and A. Y. Cho at the end of 1960s [26,27], MBE has been developed significantly. This includes advanced developments of complex and precise apparatus as well as deep understanding of the material growth mechanism. These achievements in MBE technology allows us to (i) grow high quality materials with reduced concentration of impurities and defects, (ii) change and control composition and doping accurately, (iii) build abrupt interfaces between dissimilar material systems, and (iv) control the layer thickness precisely on the atomic scale [21]. Hence, development of MBE has opened the way to study new physical phenomena and innovative devices which resulted in Nobel prizes [28–34]. A typical MBE growth chamber is illustrated in Fig. 2.1.

To provide a long enough mean free path so that atomic or molecular beams of source materials arrive at the surface efficiently without collisions, high vacuum is required. However, to minimize the incorporation of impurities and optimize the surface morphology, an ultra-high vacuum is desired. UHV is typically achieved by combinations of different types of pumps such as ion pumps, titanium sublimation pumps, cryopumps, and turbomolecular pumps depending on the type of MBE and materials [24]. In addition, liquid nitrogen cryopanels are extensively equipped around substrate holder and cells in order to condensate residual gases, insulate cells

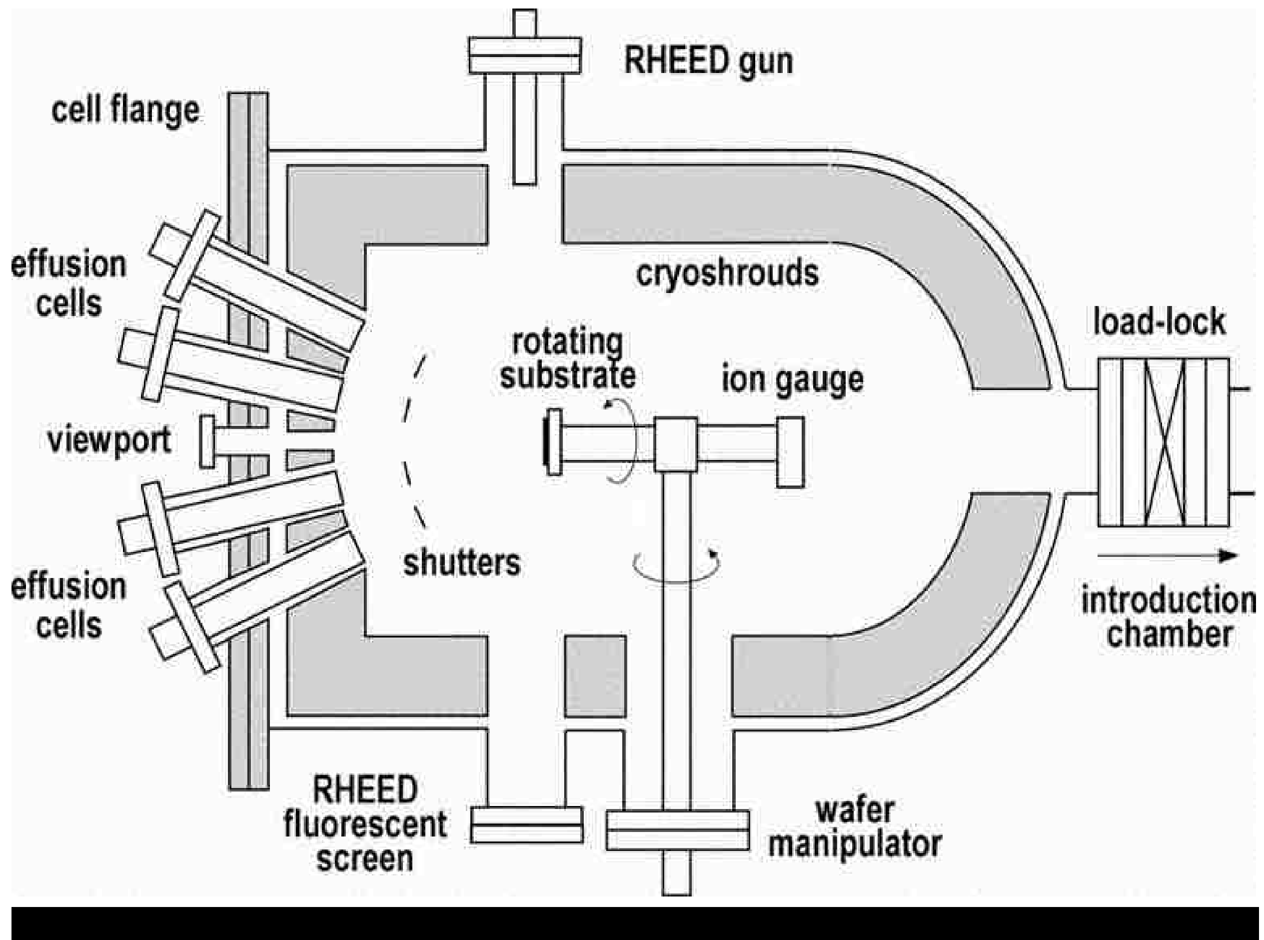

thermally, and prevent outgassing the cell flanges on which materials are built up. Moreover, implementation of a small chamber connected with a growth chamber though UHV with a gate valve between them also improves throughput and the vacuum inside the growth chamber since samples can be transferred out and in from UHV without breaking UHV of the growth chamber [35,36]. This chamber for sample exchange is usually called a load-lock chamber.

As well as a load-lock chamber, several other material analysis chambers are also connected to the growth chamber under UHV in many laboratories. In the material analysis chambers, a number of sophisticated experiments studies can be done to understand growth mechanisms and material properties. Examples of such analysis are scanning tunneling microscopy, Auger electron spectroscopy, secondary ion mass spectrometry, and X-ray

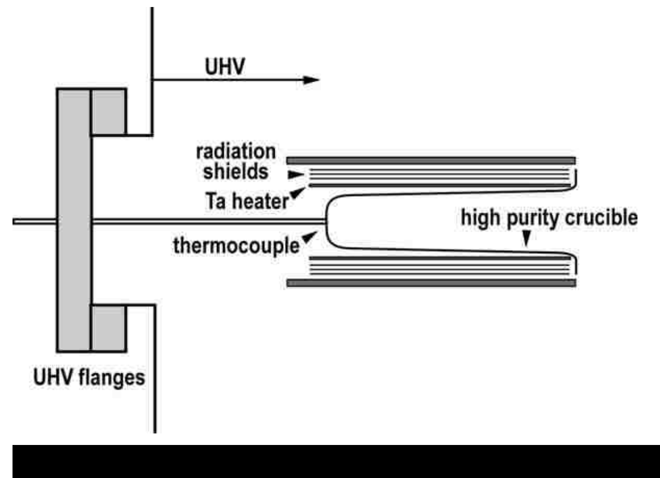

photoemission spectroscopy [21]. In most cases, reflection high-energy electron diffraction (RHEED) systems are installed directly onto the growth chamber to study growth dynamics *in-situ*. Scanning electron microscopy (SEM) can be implemented with the MBE chamber to monitor the growth in real time [37,38]. Availability of many different analytical techniques during the growth has substantially contributed to the development and understanding of MBE.

As explained above, grown materials by MBE are supplied in a form of atomic or molecular beams to the surface of substrates. To grow high quality and uniform crystals, the sources of atomic and molecular beams are quite important since they should have high purity and uniformly cover the substrate. Even though source material purity is quite high, great attention should be paid to how the atomic and molecular beams are formed. The most common way used in traditional MBE is the thermal evaporation of the source materials. In this case, the source materials are placed in crucibles, usually made of pyrolytic boron nitride, and radiatively heated by tantalum filaments wound around the crucibles. This type of cell is known as a effusion cell or Knudsen cell. The flux of the materials are controlled by the temperature of each effusion cell and a mechanical shutter equipped in front of an aperture of the cell. By opening and closing the mechanical shutters, the compositions and doping profiles of the crystals can be

modulated abruptly. In the case of the growth of group III-arsenide semiconductors, effusion cells are generally used for group III materials such as Al, Ga, and In, and dopants such as Si and Beryllium (Be) [21,24]. One can also use the effusion cell for As if only As_4 flux is required. A typical effusion cell is shown in Fig. 2.2.

For more precise control of flux of the source materials and usage of more efficient dimers instead of tetramers of group V materials, a valved cracker cell has been developed. As the name implies, a valved cracker cell is equipped with a needle valve where a flux of the source material passes though. By adjusting the position of the needle valve as well as a mechanical shutter, the flux of the source materials can be controlled precisely. The valved cracker cell has another heating zone where tetramers of group V materials such as As and phosphorus (P) can be cracked into dimers. Either dimers or tetramers can be selected by the temperature of the cracking zone. Since dimers have different surface kinetics from tetramers [26,39,40], the resulting III-V semiconductor crystals grown by dimers of the group V materials have a different quality. A typical valved cracker cell for As is shown in Fig. 2.3.

As shown in Fig. 2.1, all cells have some angle with respect to the surface of a substrate. Therefore, there should be the angular distribution of the flux on the substrates whichever type of cell is used. Hence, the substrate holder is continuously rotated azimuthally during the growth to

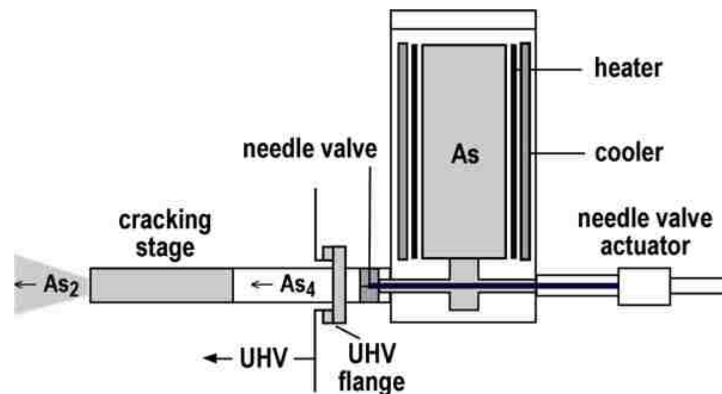

improve the uniformity of the crystal. Furthermore, the sample manipulator is usually equipped with an ion gauge on the opposite side of the substrate holder so that the flux of each material can be measured.

So far, the main components of the MBE-UHV system have been reviewed. The growth mechanisms of MBE will now be briefly mentioned. Since this thesis deals with III-arsenide semiconductors, the growth of III-arsenide semiconductors will primarily be discussed.

Generally, there are three different epitaxial growth modes depending on how strongly deposited materials interact with the substrate and themselves [41] (Fig. 2.4). If a deposited material interacts strongly with a substrate, crystal growth proceeds two dimensional (2D) layer by layer, which is called the Frank-van der Merwe (FM) growth mode [42]. Homoepitaxial layers, lattice match systems such as GaAs and AlGaAs, and pseudomorphic layers with a small lattice mismatch are generally grown by the FM growth mode.

The FM growth mode is characterized by the oscillation in the intensity of diffracted RHEED patterns, in particular, of the zero order diffracted beam due to a periodic change in surface roughness as shown in Fig. 2.5. In the case of GaAs growth, the period of each oscillation corresponds to the time required to grow one monolayer (ML) of GaAs, which is 0.283nm for GaAs (100) [43]. The surface before the growth is assumed atomically flat as in Fig.

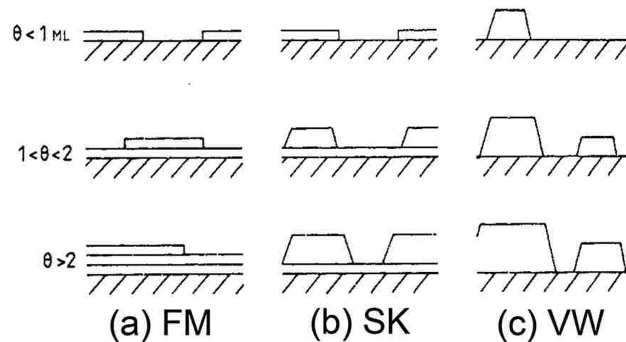

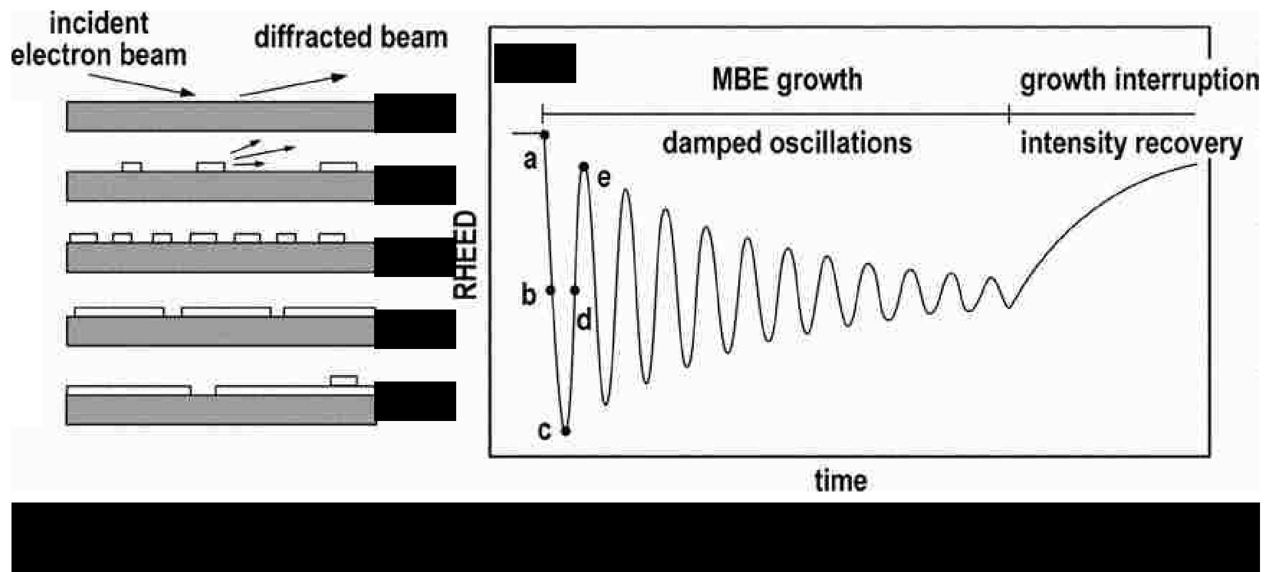

2.5(a). Once the growth is initiated, 1ML high islands nucleate on the surface (Fig. 2.5(b)). Since these ML high islands scatter the RHEED electron beam, the intensity of the RHEED diffraction patterns decreases. The intensity reaches the minimum when the density of the ML high islands reaches maximum as in Fig. 2.5(c). As the growth goes on, the ML high islands expand laterally and coalesce with other islands. Thus, the intensity increases and reaches the maximum when 1ML growth is completed (Fig. 2.5(d) and (e)). The damped oscillations are attributed to the nucleation of new ML high islands on top of incomplete layers as in Fig. 2.5(e). The growth rate of III-arsenide semiconductors is generally determined by observing the periods of the RHEED intensity at different growth conditions. Moreover, the recovery of the RHEED intensity during the growth interruption indicates the improvement of the surface flatness due to the migrations of atoms [43] (Fig. 2.5(f)).

A second growth mode is called the Stranski-Krastanov (SK) growth mode and is characterized by the coexistence of a 2D layer and three dimensional (3D) structures as in Fig. 2.4(b) [44]. The SK growth mode takes place in the growth of lattice mismatched materials systems. A typical example of such material systems is InAs and GaAs, in which the lattice

mismatch is about 7%. When InAs is deposited on a GaAs substrate, first a few MLs of InAs form a 2D layer as in the FM growth mode, and this 2D layer is called the wetting layer. Due to the lattice mismatch between InAs and GaAs, there is a compressive strain accumulating in the InAs wetting layer. When this compressive strain reaches the maximum and the 2D growth is not favorable energetically any more, 3D structures are formed to relax the comprehensive strain in the wetting layer. This transition can be observed easily by RHEED since the 2D layers show streaky RHEED patterns while the 3D structures show spotty RHEED patterns [45]. Since this growth mode is inherently associated with 3D structures, it has been extensively studied to grow self-assembled nanostructures in many different material systems [46–51].

When deposited atoms or molecules interact stronger with each other than with the substrate, they form 3D structures from the beginning of the growth as in Fig. 2.4(c). This growth mode is called the Volmer-Weber (VW) growth mode [52] and commonly observed in the growth of metals on insulators or semiconductors. The nucleation of 3D islands is followed by the coalescence of these islands and results in a rough 2D layer. Even though this growth mode was studied before the other two growth modes, it is just recently that the VW growth mode has been utilized to grow 3D semiconductor crystals called droplet epitaxy [53–55]. The detail of droplet epitaxy will be discussed in Section 2.2.

2.1.2. Experimental Setup

The UHV system used to carry out experiments in this thesis consists of the load-lock chamber, degas chamber, transfer chamber, and growth chamber, which is a solid source MBE Riber 32P system as shown in Fig. 2.6. Between each chamber, there is a gate valve to protect the vacuum of each chamber. For the normal operation, only the load-lock chamber is vented to take out the samples from the UHV system and to introduce new samples into the UHV system.

The degas chamber is equipped with a heater so that samples can be degassed to remove water molecules and other organic contaminations before loading to the growth chamber. Both the load-lock and degas chambers are pumped down by turbomolecular pumps while both the transfer chamber and growth chamber are pumped down by a detachable turbomolecular pump only at the beginning, and vacuum is kept by ion pumps and titanium sublimation pumps.

The growth chamber is equipped with six effusion cells and one valved cracker cell for As. We have two effusion cells for Ga, and each of the other cells contains Al, In, Si, and Be. During the growth, the cryopanels are cooled down by liquid nitrogen to improve the vacuum inside the growth chamber. The vacuum quality is confirmed by both an ion gauge equipped on the growth chamber and the Stanford Research Systems RGA200 residual gas analyzer. The

sample manipulator has another ion gauge for the flux measurements and the substrate holder with a heater. The temperatures of the heater and all the cells are measured by thermocouples and controlled by a computer program though a proportional-integral-derivative (PID) feedback loop. The growth is monitored by RHEED, and the temperature of the samples is also measured by the *k*SA BandiT temperature system which is a highly accurate optical transmission thermometry system.

Before the growth, the growth rate of each element was calibrated by observing the RHEED oscillation as explained in the previous section. Dopant cells were calibrated by the growth of four 1.5μm thick samples with different cell temperatures and Hall effect measurements.

2.2. Droplet Epitaxy

Droplet epitaxy is an alternative method to the SK growth mode for the creation of nanostructures. In the studies of the growth of flat GaAs layers, it was found that the supply of Ga without As or the growth under Ga rich conditions forms metal Ga droplets on the GaAs surface based on the VW growth mode and makes the surface rougher [56,57]. Thus, the typical 2D growth of III-arsenide semiconductors takes place under As rich conditions by using the group V to group III flux ratio of ~20 to prevent droplet formation anywhere on the surface. However, an astonishing growth protocol using these undesired droplets was proposed by Koguchi *et al.* [53,54]. In these papers, metal Ga droplets were applied to the growth of quantum dots, and this new growth method was named droplet epitaxy.

Unlike the traditional growth of III-arsenide semiconductors in which both group III materials and As are supplied to the surface concurrently, droplet epitaxy splits the supply of the

group III materials and As. The supply of the group III materials, such as Ga, Al, and In, forms nano-scale metal droplets of the group III materials on the surface of III-arsenide semiconductors. This step plays a main role in determining the size and density of resulting 3D nanostructures. Available growth parameters for the control of dimension of droplets are the substrate temperature, growth rate, and coverage of the group III materials. Before the deposition of droplets, a buffer or barrier layer is usually grown on substrates under traditional As rich conditions. Therefore, the surface has an As rich surface reconstruction. For example, GaAs (100) substrates usually have the c(4×4) and (2×4) surface reconstructions at low temperature and high temperature, respectively [58,59]. Hence, the first few MLs of the group III materials are incorporated into the surface and change the surface from As rich to Ga rich. In the case of the formation of Ga droplets on the GaAs (100) substrates, 1.75ML and 0.75ML of Ga are consumed to convert the surface from As rich to Ga rich for c(4×4) and (2×4) surface reconstructions, respectively [21,58]. Then, the nucleation of Ga droplets start only after the Ga rich (4×6) surface reconstruction is established. This conversion of the surface reconstruction enables the growth of 3D structures without WLs which cannot be avoided in the SK growth mode [60]. In the case of the deposition of Ga on AlGaAs, the first few layer of Ga form a thin GaAs WL on the AlGaAs substrate. However, if AlGa is supplied to the surface just to convert the As rich reconstruction to the group III rich reconstruction, subsequent deposition of Ga forms metal droplets from the very beginning. Thus, the resulting GaAs structures after the crystallization do not have the WL.

The density of droplets strongly depends on the substrate temperature since the thermally activated surface diffusion of adatoms which depends on the substrate temperature exponentially determines the density of droplets [61,62]. At high temperature, Ga adatoms on the surface can

effectively migrate on the surface and find existing droplets. Hence, the formation of new droplets is suppressed, and the density of droplets remains small at high substrate temperatures. The droplet density is also as a function of the growth rate [61]. The growth rate corresponds to how many Ga atoms impinge upon the surface per unit time. Hence, the higher the growth rate, the more Ga adatoms are on the surface. At a fixed substrate temperature, the diffusion length decreases as the density of the surface adatoms increases. Therefore, the density of droplets increases with the growth rate. According to the classical nucleation theory, the density of droplets shows a power dependence on the growth rate [41,63]. At a fixed temperature and growth rate, an increase in the coverage of Ga simply enlarges each existing droplet without changing the density.

The second step of droplet epitaxy is the supply of the group V materials (As in the case of III-arsenide growth) to crystallize metal group III droplets on the surface. This crystallization process is in charge of determining the shape of final 3D structures and can be controlled by adjusting the substrate temperature and As flux. During the supply of As, several different physical phenomena occur on the surface. The first one is a reaction between impinging As and Ga in the droplets. Once the concentration of As in Ga droplets exceed the solubility of As in Ga, As and Ga atoms form GaAs molecules and deposit themselves at the interface between the Ga droplets and the substrate, especially around the perimeter of the droplets. This process is enhanced by the high As flux since more As dimers or tetramers are supplied to Ga droplets and react with Ga atoms in the droplets quickly. The second process is the diffusion of Ga atoms from droplets. As soon as the As flux is supplied to the surface, the surface reconstruction changes from the Ga rich (4×6) reconstruction to the As rich (2×4) or c(4×4) reconstruction depending on the substrate temperature and crystallization time. Then, Ga atoms in the droplets

diffuse on the As rich surface and bond to As atoms on the surface. The diffusion length is longer at higher substrate temperature because of the thermal activation of Ga atom diffusion. In addition, the diffusion is suppressed by high As flux since the surface is always As terminated even around the droplets, and Ga atoms from the droplets immediately find As atoms and stop the diffusion to form new bonds to As atoms.

The last physical phenomenon associated with the crystallization step is local etching of the substrate underneath the droplets. In 2005, Wang *et al.* reported the etching of the substrate by Ga droplets [14]. According to them, As atoms in the GaAs substrate below Ga droplets dissolve into the droplets and escape to vacuum or recrystallize with Ga atoms in the droplets at the perimeter. Thus, as long as there are Ga droplets on the surface, they drill nanoholes on the substrate. Hence, the etching of the substrate by droplets by *in-situ* annealing in the growth chamber without the supply of As was also observed [64,65]. A simple model of the etching

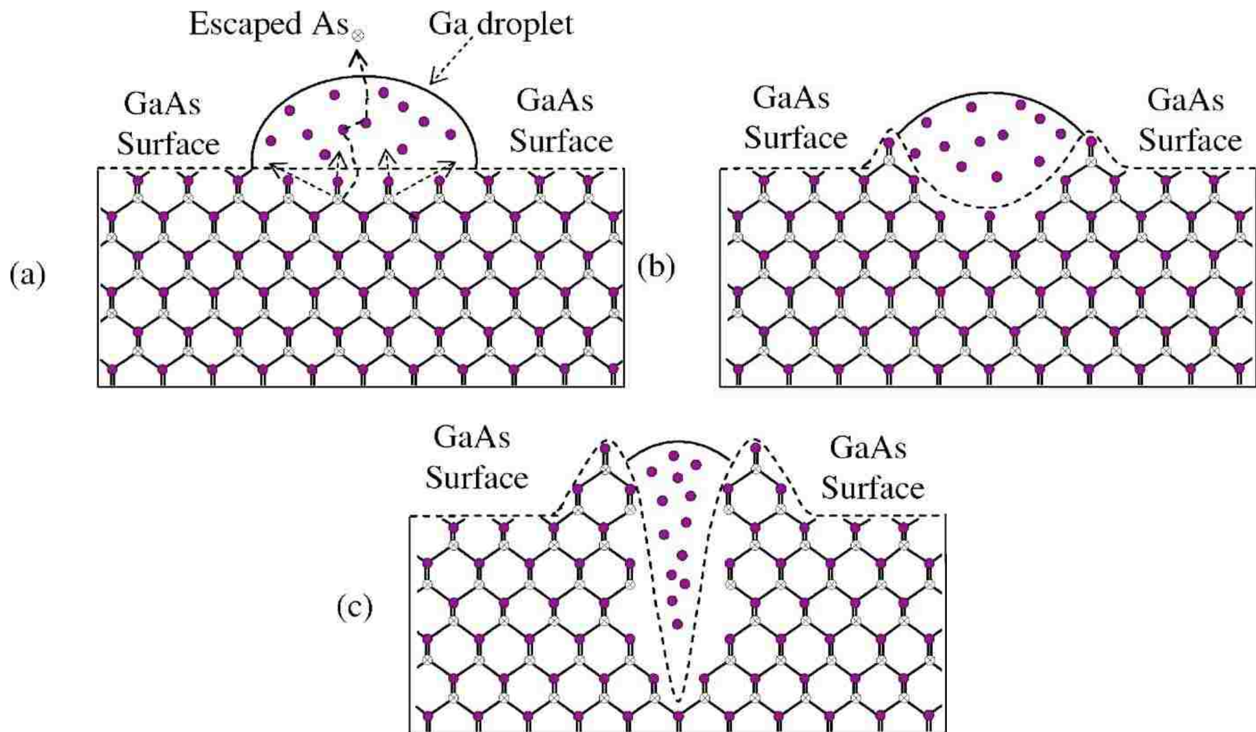

process is shown in Fig. 2.7. This process is enhanced at a high substrate temperature because of the thermal activation of the dissolution of As atoms in the substrate.

There are mainly three advantages of droplet epitaxy over the traditional 3D growth based on the SK growth mode. First of all, droplet epitaxy enables fabrications of 3D structures in both lattice matched such as GaAs and AlGaAs, and lattice mismatched systems such as InAs and GaAs. Since droplet epitaxy does not require strain on contrary to the SK growth mode, one can grow 3D nanostructures in lattice matched material systems. In addition, the density of 3D nanostructures can be easily controlled over three orders of magnitudes in droplet epitaxy. Since the density of 3D structures is determined by that of droplets, which depends on temperature exponentially, one can tailor the density of nanostructures simply by controlling the substrate temperature for the droplet deposition. The last one is capability of fabricating various types of complicated nanostructures such as quantum dots (QDs) [55,66], quantum rings (QRs) [67,68], coupled QD pairs [69,70], concentric QRs [71,72], nanoholes [14,64], and QD molecules [73,74]. The growth conditions for the crystallization step change the contribution of three different physical phenomena, namely reactions of Ga and As atoms, Ga diffusion, and etching, to the crystallization. Hence, by carefully controlling the substrate temperature and As flux, one can engineer the shape of 3D nanostructures.

2.3. Sample Description

2.3.1. Optimization of Nanoholes

To study effects of nanoholes on the electrical properties of QW heterostructures in a consistent way, optimization of the growth conditions of nanoholes was carried out to control density and depth of nanoholes so that either density or depth of nanoholes is fixed, and the other

parameter is varied. In addition, nanoholes should be deep enough to observe their effects on a 2DEG in the QW. All samples for the optimization of nanohole growth are grown on GaAs (001) semi-insulating substrates by MBE. The GaAs substrates mounted on a molybdenum holder were annealed at 350°C for 1 hour in the degas chamber and then loaded into the growth chamber. Subsequently, the substrates were ramped up to 610°C and annealed under a constant As_4 beam equivalent pressure (BEP) of 5.0×10^{-6} Torr for 10 mins to remove the native amorphous oxide layer. Before the growth of Ga droplets, a 500nm GaAs buffer layer was grown at 580°C to make the surface atomically flat. After the buffer layer growth, the (2×4) surface reconstruction was observed by RHEED for all samples. So as to be ready for Ga deposition to form droplets, the substrate temperature was reduced to the growth temperature while the As flux was shut off at 450°C or 455°C in the case of growth temperature of 450°C. Then, a Ga flux was supplied to the surface to form Ga droplets with 0.5ML/s. Before the Ga deposition, the growth was paused for several minutes at the growth temperature to remove residual As molecules in the growth chamber so that the background pressure was kept less than 1.5×10^{-8}Torr during the Ga deposition in order to minimize interactions between As and Ga atoms during the droplet deposition [75–77]. After the Ga deposition, a halo RHEED pattern was observed since electrons from the RHEED electron gun were scattered by the Ga droplets [54]. Just after the Ga deposition, the metal droplets were exposed to the As_4 flux of 5.0×10^{-6}Torr for 1 minute to form nanoholes on the surface. To prevent Ostwald ripening of the droplets before crystallization, the As flux was applied to the surface immediately after the Ga deposition [61,62,78]. Then, all samples were quenched and taken out of the UHV chambers for morphology characterization by AFM.

The coverage of Ga is 10ML, and the growth temperatures for Ga droplets and subsequent crystallization by As were 350, 400, and 450°C. Also, at 450°C, the Ga coverage was varied to 20, 30, 60, and 90ML. The coverage of Ga for droplets corresponds to the amount of Ga required to grow the same thickness of GaAs as the coverage. Nanoholes are grown at the same growth condition several times to obtain good statistics of their physical parameters. The results are summarized in Section 3.2.1.

2.3.2. QWs with Nanoholes

In order to investigate effects of the depth of nanoholes on the QW heterostructures, four samples of InGaAs QWs with and without nanoholes were analyzed. The growth conditions for nanoholes are determined based on the results of the optimization to grow nanoholes with the same density but different depth, which are discussed in Section 3.2.2.

All four samples were grown on GaAs (001) semi-insulting substrates with a miscut angle smaller than 0.1°. All the substrates were mounted on a molybdenum holder and degased at 350°C for 1 hour in the degas chamber to remove water and other organic contaminations and annealed under a constant As_4 flux for 10 minutes at 610°C in the growth chamber to remove the native oxide layer. Then, a 200nm GaAs buffer layer and 15 periods of 1.5nm GaAs/1.5nm $Al_{0.3}Ga_{0.7}As$ superlattice were grown at 580°C with 0.7ML/s for GaAs and 1ML/s for $Al_{0.3}Ga_{0.7}As$ to achieve a smooth surface and prevent segregation of impurities from the substrates at the interfaces [79–82]. Then, another 300nm GaAs buffer layer was grown. During the growth of the last 36nm of the second GaAs buffer layer, the substrate temperature was reduced to 560°C for the InGaAs QW growth. Then, a 12nm $In_{0.12}Ga_{0.88}As$ QW layer was grown at 560°C with 0.81ML/s. Before and after the QW layer growth, 20s and 15s growth

interruptions were adopted to achieve smooth interfaces, respectively. Subsequently, a 15nm $Al_{0.2}Ga_{0.8}As$ spacer, 25nm Si doped $Al_{0.2}Ga_{0.8}As$ barrier layer, and 2.5nm GaAs capping layer were grown. The substrate temperature was ramped up to 610°C during the growth of the doped $Al_{0.2}Ga_{0.8}As$ barrier layer. The doping density of the Si doped $Al_{0.2}Ga_{0.8}As$ barrier layer and GaAs capping layer was $2.4\times10^{18}cm^{-3}$ and $3.0\times10^{18}cm^{-3}$, respectively. Right after the GaAs capping layer growth, the sample without nanoholes was quenched and removed from the UHV system for subsequent characterization. Figure 2.8 shows a schematic of this reference QW, and calculated band diagrams are shown in Fig. 2.9. The band diagrams are calculated by the 1D Poisson Schrödinger equation solver programed by Dr. Gregory Snider [83]. This reference QW was named as SF120.

After growing the same structure, nanoholes were formed on the surface for the other three samples. Right after the growth of the GaAs capping layer, the substrate was cooled down to 450°C while the As shutter and valve were closed at 455°C to reduce the background As pressure. The RHEED pattern changed from (2×4) to c(4×4) around 480°C, and went back to

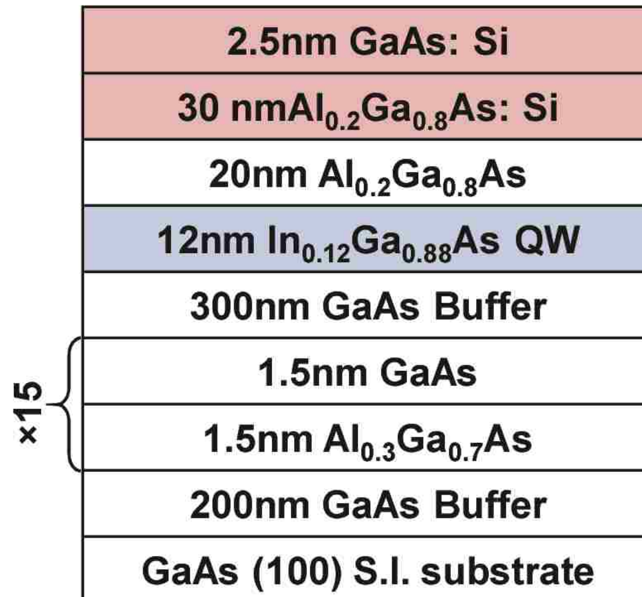

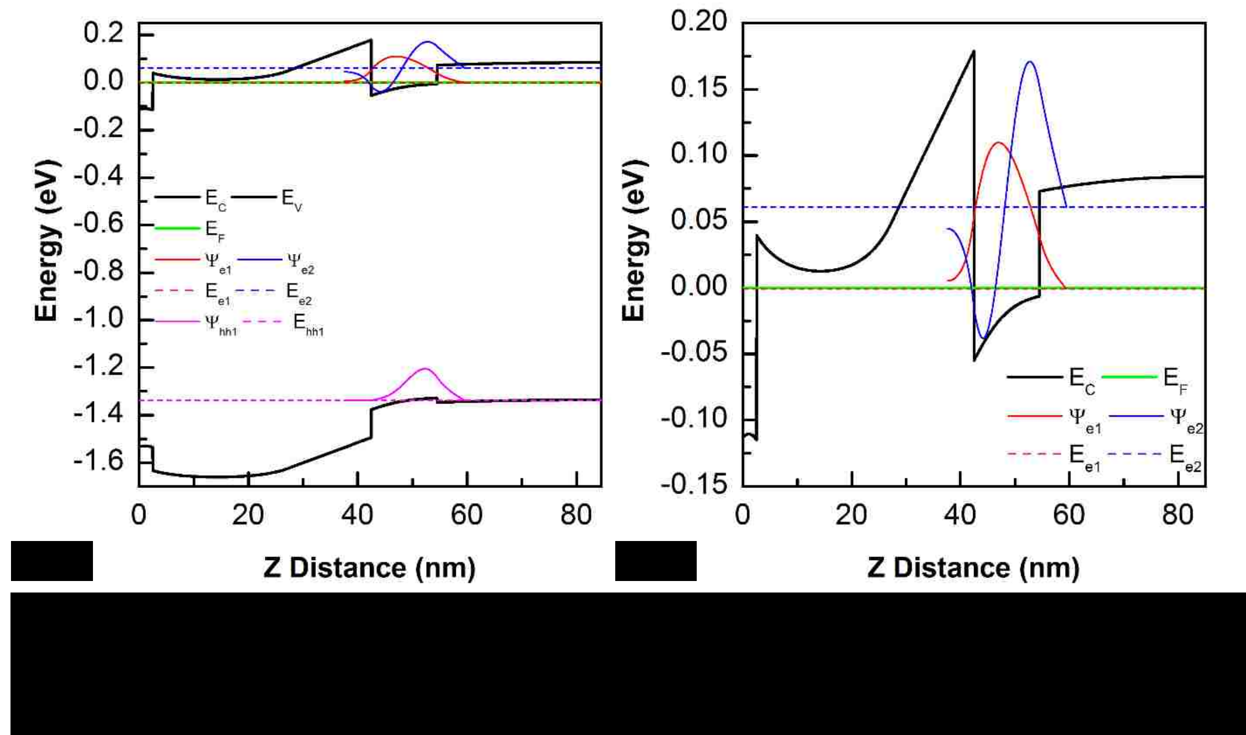

(2×4) when As was turned off [58,59]. After waiting for 5mins to reduce the background pressure less than 1.5×10^{-8} Torr, a Ga flux is supplied to the surface to form metal Ga droplets with 0.5ML/s on the surface of the GaAs capping layer. The Ga coverages were 30ML, 60ML, and 90ML for Sample SF121, SF122, and SF123, respectively. After the deposition of Ga droplets, a halo RHEED pattern was observed due to the scattering of electrons by Ga droplets. Then, a As_4 flux is supplied to the surface for 1 minute to crystalize Ga droplets. The BEP of the As_4 flux was 5.0×10^{-6} Torr. An unclear spotty RHEED pattern was observed after 1 minute crystallization by As. Then, all samples were quenched and removed from the UHV systems for subsequent characterization after annealing by As.

Chapter 3: Morphology Characterization

3.1. Atomic Force Microscopy

Atomic force microscopy (AFM) is one type of scanning probe microscopy (SPM) which has sub-nm resolution [84]. In SPM, a sharp probe scans over the surface of samples, and interactions between a probe and the samples are measured. The interactions to be measured in SPM should be dependent on the distance between a probe and the samples exponentially and dominant in nm range. One examples is tunneling current which is utilized to measure the interactions between the samples and a probe in scanning tunneling microscopy. AFM measures atomic forces between samples and a probe which consists of a cantilever with a sharp tip as shown in Fig. 3.1. The amount of the interactions is kept constant during the scan by moving probe up and down vertically though a PID feedback loop, and the vertical position of each point in x-y plane is recorded to create AFM images. The precise vertical and lateral position control is usually provided by applying appropriate voltages to a piezoelectric material. Since these interactions depend on the distance between a probe and the samples exponentially, a small change in the height of structures on the sample surface changes the amount of the interactions

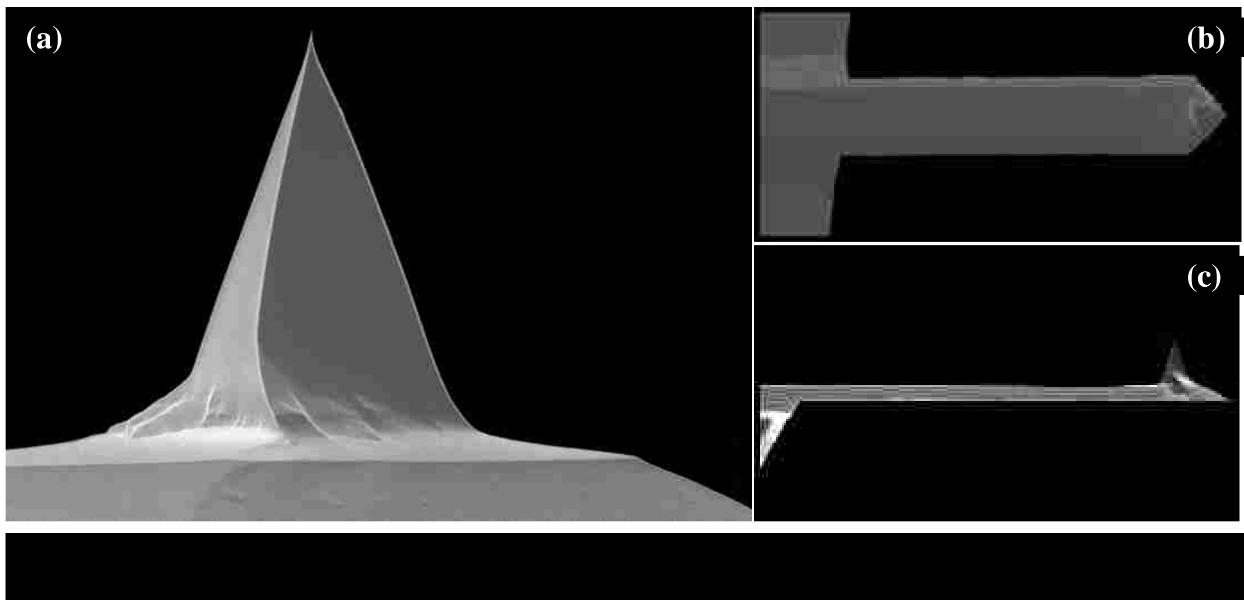

remarkably. Thus, the changes in the interactions are big enough to be measured accurately. This is why SPM achieves sub-nm resolution successfully.

In AFM, there are three different operation modes: contact, non-contact, and tapping mode. In the contact mode, a probe is always in contact with the surface, and deflection of the cantilever is measured by a laser as the interaction between samples and a probe. This mode has the highest resolution and a high scan speed but also easily contains measurement errors due to lateral forces and capillary forces due to a thin layer of water which is present on many surfaces in air [85]. Moreover, a probe will sometimes scratch and damage the surface of the samples in the contact mode. As its name implies, the non-contact mode operates measurements without contact between a probe and the samples. The cantilever is driven to oscillate at the resonant frequency just above the surface of the samples without contact. Since the probe is in proximity to the surface, it feels the van der Waals forces from the surface, and the frequency of the oscillation becomes off resonant. Thus, the amplitude of the oscillation decreases, and this

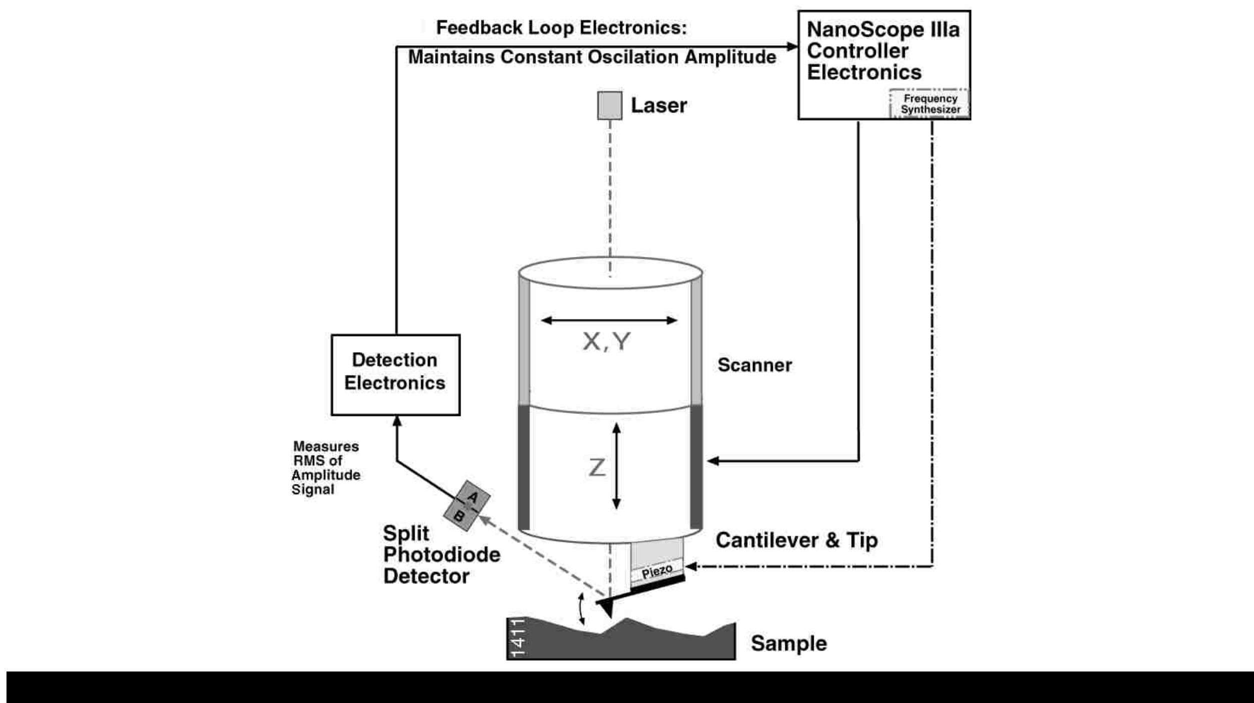

decrease in the amplitude is measured as the interaction. In this mode, the surface is protected from damage since there is no force exerted on the surface, but the non-contact mode has low lateral resolution and a low scan speed. Moreover, a thin layer of water on the surface plays an important role in this mode. Thus, the non-contact mode usually works only on extremely hydrophobic samples [85].

The tapping mode is currently the most popular. In this mode, the cantilever is driven to oscillate at or slightly below the resonance frequency. Then, a probe lightly taps the surface of the sample during measurements, and the amplitude of the oscillation is measured as the interaction. The operation principle is illustrated in Fig. 3.2. The tapping mode has high lateral resolution and causes less damage to the samples, although the scan speed is slightly slower than the contact mode.

The model of AFM used in this study is a Veeco Dimension V with tapping mode under ambient conditions. Probes are Applied NanoStructures, Inc. ACTA Model, which have a tip radius of curvature of 6nm, a resonant frequency of 300±100Hz, and a spring constant of 37±40N/m [86]. SEM pictures of this probe are shown in Fig. 3.1. All AFM pictures were analyzed suing NanoScope Analysis 1.5 software(Bruker).

3.2. Results and Analysis

3.2.1. Optimization of Nanohole Growth

The samples for the optimization of nanohole growth, which are described in Section 2.3.1, were studied first. Density and depth of nanoholes grown at different growth conditions as a function of Ga coverage are summarized in Fig. 3.3. As discussed in Section 2.2, the density of nanoholes depends just on the growth temperature under a constant growth rate. The Ga

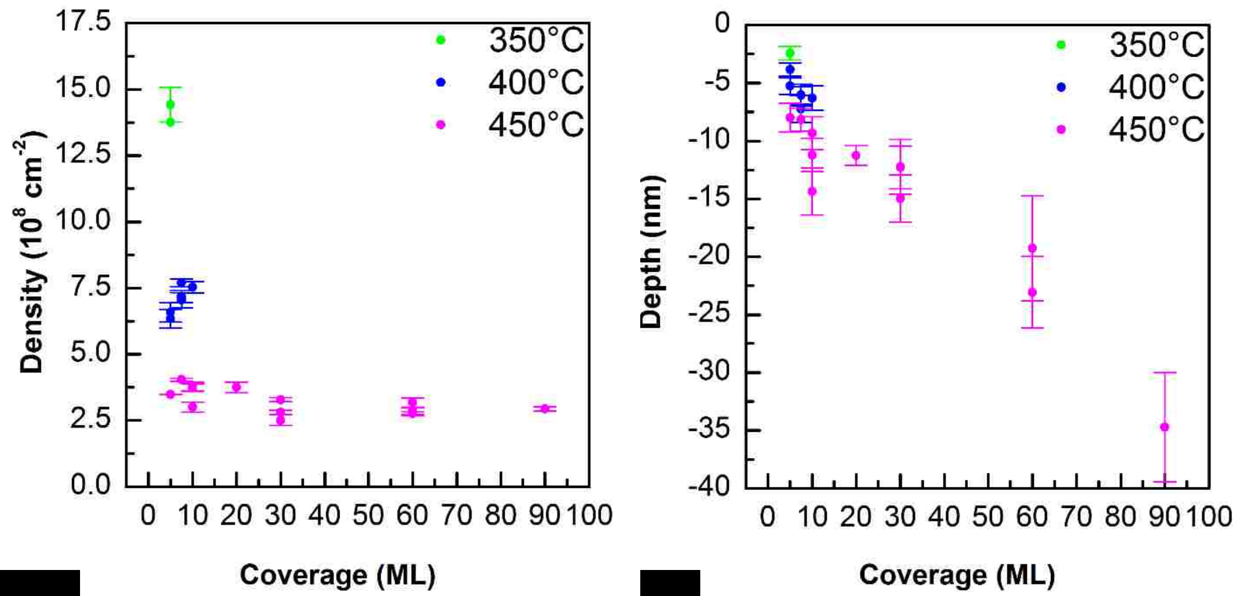

coverage has almost no effects on the density of nanoholes grown at 450°C. However, as shown Fig. 3.3(b), the depth of nanoholes strongly depends on the coverage. Also, the depth of nanoholes grown by 90ML Ga droplets is between 30nm and 40nm. Since the distance between the surface and the top interface of the QW is 52.5nm as shown in Fig. 2.8, these nanoholes seem to be deep enough to affect the QWs. Therefore, the growth temperature for nanoholes is chosen as 450°C to keep the same density while the Ga coverage is varied to change the depth of nanoholes. It is worth mentioning that this is the first observation of nanoholes as deep as about 35nm. The depth of the nanoholes keeps increasing with the coverage; hence we expect that even deeper holes can be fabricated by deposit more Ga for the droplet formation.

3.2.2. Nanoholes on QW

Figure 3.4 shows 2μm×2μm AFM pictures and line profiles along [110] and [-110] crystallographic direction of SF121, SF122, and SF123. The dimension of these nanoholes is also summarized in Table 3.1. Both density and depth of nanoholes agree with the results of the

optimization of the growth conditions of nanoholes. Since the optimization was carried out on the GaAs buffer layer, this result indicates that the etching rate by Ga droplets does not depend on the material below the droplets. The deviation in depth is about 14%, which agrees with previously reported results [21]. As shown in the previous section, the more Ga is deposited, the deeper the nanoholes. The density of nanoholes also increases with Ga coverage. This can be explained as following. At the beginning of the deposition of Ga, the density of droplets starts to increase and saturate after the deposition of a certain amount of Ga when the distance between the droplets is twice as long as the diffusion length of Ga adatoms. After the saturation of the density, Ga adatoms on the surface will find pre-existing droplets before they find another adatom. However, there are some possibilities that they will find another adatom and nucleate a new droplet. This process will happen more often as Ga is deposited on the surface. Thus, the density also increases with the coverage. However, the deviation in density is still small, so this set of samples enables us to investigate effects of just the depth of nanoholes on the electrical properties of the QW.

TABLE 3.1. Dimension of nanoholes of all samples.

Sample Name	Ga Coverage (ML)	Depth (nm)	Diameter (nm)	Density (10^8cm^{-2})
SF120 (Reference QW)	0	-	-	-
SF121	30	12.27±1.83	107.38±13.98	2.50±0.20
SF122	60	23.07±3.09	109.08±18.26	2.86±0.12
SF123	90	34.72±4.72	105.38±22.04	2.94±0.08

Based on the AFM analysis, the nanoholes reach the interface between the doped $Al_{0.2}Ga_{0.8}As$ barrier layer and undoped $Al_{0.2}Ga_{0.8}As$ spacer layer for SF122, and the middle of the doped barrier and undoped spacer layers for SF121 and SF123, respectively. In addition, anisotropy of nanoholes is observed for all the samples. This is because the difference in the

diffusion on the anisotropic reconstructed (2×4) surface. The (2×4) reconstructed GaAs surface possesses highly anisotropic structures due to its reconstructed dimer rows running along [-110] direction [58,59,87].

In summary of this section, it was found that the growth temperature for the Ga deposition controls the density of nanoholes on GaAs (100) substrates at a constant growth rate of Ga. Besides, at the growth temperature of 450°C, the coverage of Ga droplets does not affect the density of the nanoholes. However, the morphology analysis demonstrates that the coverage and the growth temperature affect the depth of the nanoholes which is critical to modulate the properties of the 2DEG and QW heterostructures. We successfully fabricate nanoholes as deep as about 35nm for the first time by 90ML of the Ga deposition. Our result indicates that it is possible to grow even deeper nanoholes by increasing the Ga coverage. In addition, the developed growth recipes allow for the fabrication of the nanoholes with constant density on the surface but with varied depth.

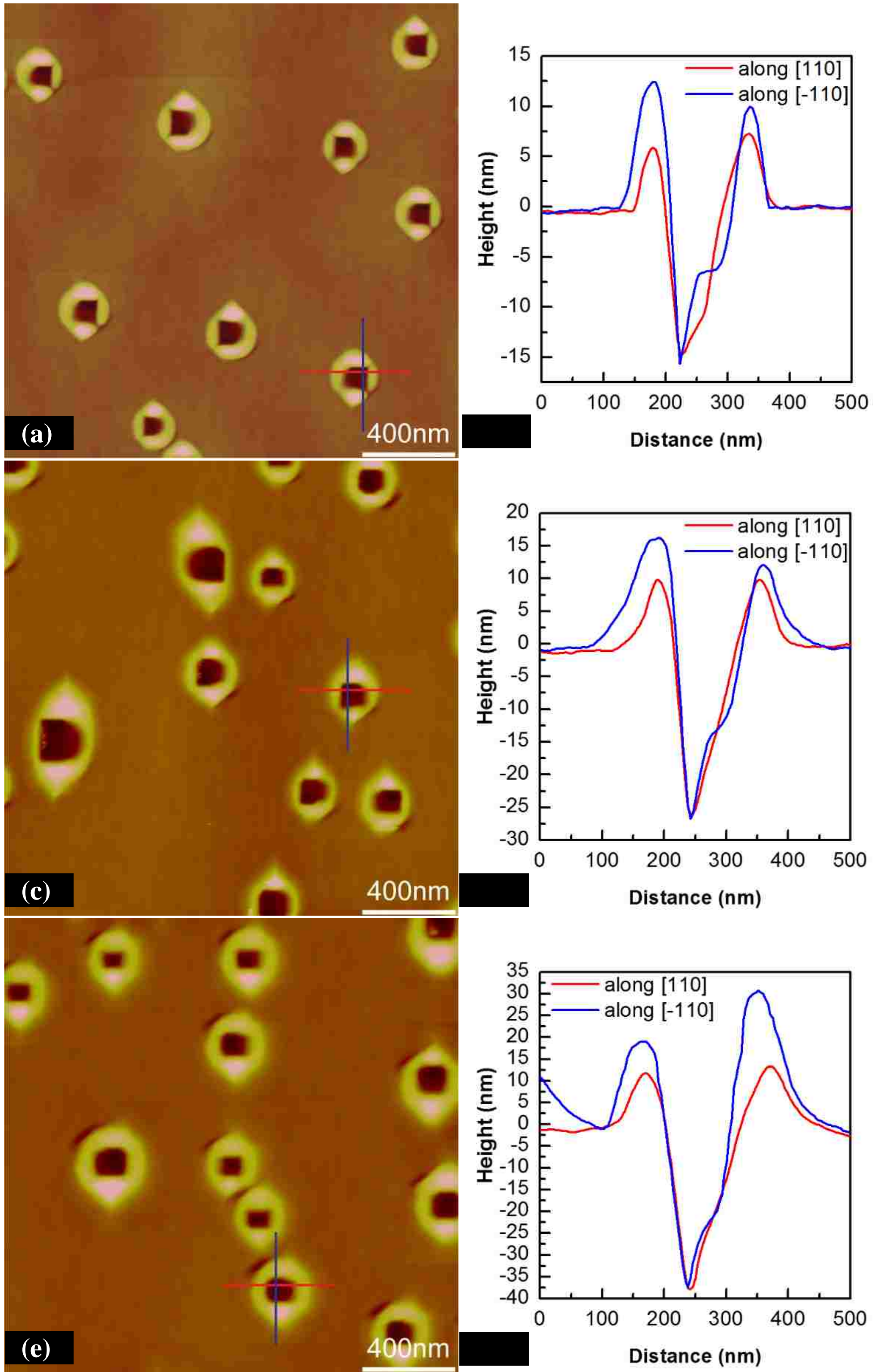

(a)
400nm
along [110]
along [-110]
Height (nm)
Distance (nm)
(c)
400nm
along [110]
along [-110]
Height (nm)
Distance (nm)
(e)
400nm
along [110]
along [-110]
Height (nm)
Distance (nm)

Chapter 4: Electrical Characterization

4.1. Fabrication

4.1.1. Principles of Photolithography

Photolithography is a process to pattern micron-scale features on semiconductors with high precision. In general, as the first step of photolithography, a light sensitive material called a photoresist is spun on samples after cleaning the surface. A photoresist is generally a mixture of complex hydrocarbon molecules. Only a portion of the total mixture is actually sensitive to light, and its chemical bonds are broken by the energy from the light. Then, the exposed photoresist reforms a new stable chemical structure. Based on what kinds of chemicals are used for the light sensitive material, the photoresist can be classified into two types: positive and negative photoresist [88]. For a positive resist, a new chemical structure formed in the exposed photoresist

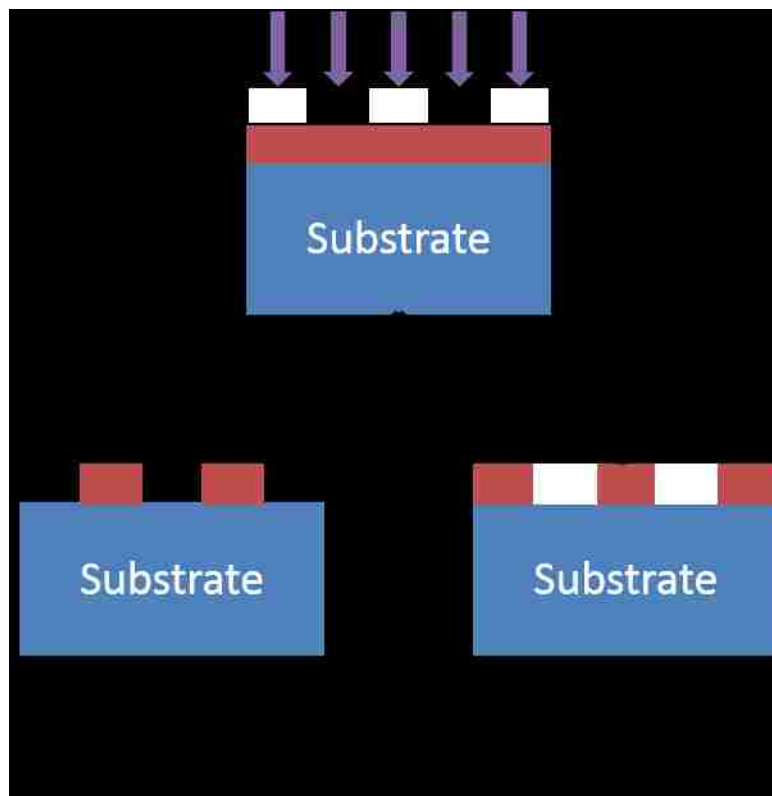

is soluble to a special solution called developer and will be removed after the development. On the other hand, for a negative resist a new chemical structure formed in the exposed photoresist is insoluble to a developer. Hence, unexposed part of the photoresist will be removed after the development. This difference is illustrated in Fig. 4.1.

After the application of the photoresist on the surface, it is exposed to light through a photomask which has desired patterns. The patterns of the photomask are completely transferred in the photoresist when the samples are immersed into a developer. The photoresist with the patterns can be used as a mask for selective etching or a sacrificial layer for patterning metal layers on the surface in lift off process. Details of photolithography carried out for the samples are described in Section 4.1.3.

4.1.2. Metal-Semiconductor Contact

When a metal and semiconductor come into close contact, the Fermi levels in both the metal and semiconductor should be constant throughout the system at thermal equilibrium. Since electrons redistribute around the contact to bring the system into equilibrium in almost all the cases, the band structure of the semiconductor is deformed and forms a potential barrier at the metal-semiconductor junctions. The barrier height depends on metals, semiconductors, doping type and densities, surface defects, how the metal-semiconductor junctions are prepared, etc. Since all semiconductor devices have metal-semiconductor contacts, the formation of barrier and transport mechanisms have been studied extensively. In practical terms, metal-semiconductor contacts are classified into two types. One is Schottky contacts, and the other is Ohmic contacts.

Schottky contacts show rectifying or diode behavior. In fact, one of the oldest semiconductor devices is the Schottky diode made by copper and iron sulfide [89]. Physical mechanisms behind the barrier formation were developed by Schottky, and thus, this type of

metal-semiconductor contacts is referred to as Schottky contacts [90]. Schottky contacts have similar current-voltage (I-V) characteristics to p-n junctions. However, Schottky diodes are unipolar while the p-n junction diodes are bipolar. Hence, Schottky diodes are suitable for fast switching devices [7]. Another example of device applications of Schottky contacts is gate contacts for field effect transistors [91]. The transport mechanisms of currents across Schottky contacts will be discussed later in Section 4.4.1.

Ohmic contacts follows Ohm's law in I-V measurements. This means that current through Ohmic contacts linearly increases with the applied voltage. Since Ohmic contacts are used to supply a current to devices, the contact resistance should be negligible compared to the resistance of the devices. Therefore, it is really important to characterize and measure the contact resistance to make sure that Ohmic contacts have sufficiently small contact resistance and do not disturb the device performance.

Contact resistances of Ohmic contacts can be measured by several different methods using different geometric structures. One of these methods is the transmission line model (TLM)

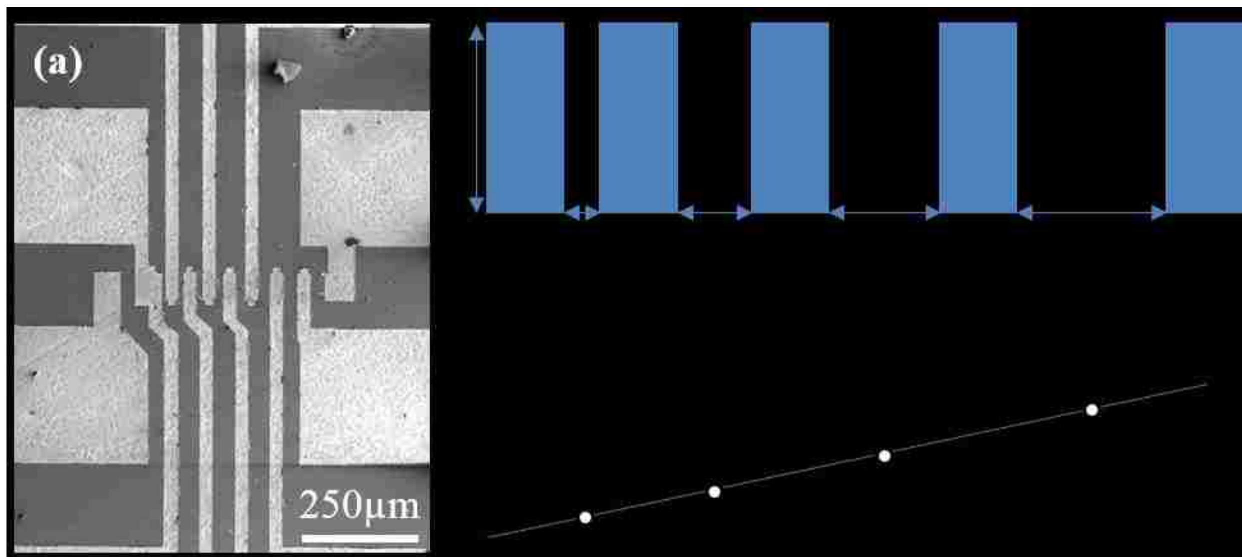

technique. The TLM technique was proposed by Shockley [92] and has been widely accepted to obtain contact resistances. The TLM test structure is a series of identical contacts whose width is *w* and spacing between two contacts, d_i, is varied as shown in Fig. 4.2(a) and (b). Assuming the contact resistance of all contacts is identical, the total resistance between two of these contacts is given by

$$R = 2R_C + r_S \frac{d_i}{w} \tag{4.1}$$

where R is the total resistance between two contacts, R_C is the contact resistance of each contact, and r_S is the sheet resistance of the semiconductor material between the contacts [93–95]. Hence, if the total resistance, R, is plotted as a function of the spacing between two contacts, d_i, the slope of the fitting line is r_S/w and the intercept is $2R_C$ as in Fig. 4.2(c).

4.1.3. Experimental Setup and General Fabrication Procedure

All QW samples (SF120, SF121, SF122, SF123) are fabricated to form appropriate metal contacts for electrical characterization. The fabrication of each structure, including both etched structure and metal contacts, is explained in each section of characterization. Hence, a brief description of the basic procedures, equipment, and chemicals used in the fabrication are outlined next.

Before spin coating photoresist onto the surface, all samples were cleaned in acetone, methanol, and isopropyl alcohol (IPA) for 5minutes each with ultrasonic agitation to remove both organic and inorganic contaminations on the surface. Each sample was then mounted on a 2inch Si wafer with glue for ease in handling samples. A positive photoresist AZ4330 (Hoechst Celanese) was spun onto the surface by a spin coater (Brewer Scientific CEE-100). The spin coater is programmable so that the thickness of the photoresist is constant over the entire surface except the edges. After the application of the photoresist, the samples were baked in an oven

(Lindberg/Blue M Gravity Convection Oven GO1330SA) for several minutes to increase its thermal, chemical, and physical stability for subsequent steps [88]. After the bake, the photoresist was exposed with a simple Greek Cross structure mask and developed to measure its thickness. The spin coater program was optimized to achieve the thickness thicker than 3μm before processing actual samples.

The next step is an exposure of the photoresist to the UV light. For this purpose, the Karl Suss MJB-3 Mask Aligner and glass plate masks for specific structures were used. The intensity of the UV light was 10.8mW/cm^2, and the exposure time was calculated based on the thickness of the photoresist and the material parameters [96]. After the exposure, the samples were immersed into the developer AZ400K diluted by deionized (DI) water in ratio 1:3. The development time was also optimized experimentally and determined to be 1min 45s.

For Hall effect measurements and noise studies, devices of accurate dimensions should be insulated from each other laterally. This can be done by defining mesa structures by photolithography and wet chemical etching. The etchant solution was H_3PO_4: H_2O_2: H_2O (1:1:20) [95,97], and the etching rate was calibrated by etching identical structures as SF120 grown separately for the calibration. For the QW structure studied in this thesis, the etching rate is 190nm/min using this acid solution. After etching, the residual photoresist was removed by acetone and cleaned by methanol and IPA.

Subsequently, metal contacts were prepared by an additional photolithography step and followed by a lift-off process. Again, all steps described above were repeated with a different mask to define contact pads. To provide high quality contacts, the surface native oxide was removed by etching with HCl:H_2O (1:1) [95].Then, samples were loaded into a vacuum chamber of an electron beam evaporator (Edward Auto 306 Vacuum Coater). In order to prevent

oxidization of the GaAs surface, the samples were loaded into the electron evaporator chamber right after they were removed from the etchant and dried by dry N_2 gas. Several layers of thin metals were deposited on the surface of the samples with the patterned photoresist. The thickness was monitored by a quartz crystal microbalance equipped on the electron beam evaporator. The thickness and type of metals depend on whether Ohmic or Schottky contact is required. The details of metallization are illustrated in Section 4.3.2 and 4.4.2 for each characterization. In general, AuGe eutectic/Ni/Au and Ti/Au are applied for Ohmic and Schottky contacts, respectively [98–101].

After the deposition of the metals, the excess metals were removed by dissolving the photoresist underneath the excess metals by acetone with ultrasonic agitation. The acetone was kept at 40°C to ensure high quality lift-off process. Once the metal contact structures were well defined and not shorted by the excess metals, the samples were cleaned by methanol and IPA and dried with dry N_2 gas.

In the case of Ohmic contact, the samples were annealed to let metals diffuse into the substrate. This annealing was carried out under N_2 ambient since oxygen can cause several hurtful problems [95]. As discussed in Ref. 94 and 95, the annealing process is quite complicated, and thus, the standard annealing conditions to obtain the minimum contact resistance have not been established yet. Therefore, I studied the annealing conditions to optimize Ohmic contact of the reference QW.

The structure used for this optimization is identical to SF120, and the details of the fabrication are summarized in Section 4.3.2. Each sample has eight TLM structures at different position of the surface, and the contact resistance was measured for all eight structures. Typically, the thermal anneal is executed near 400°C for several minutes [95]. Hence, the

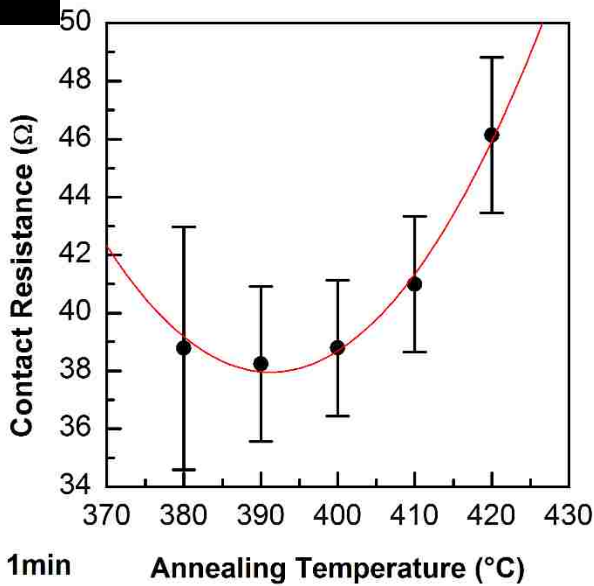

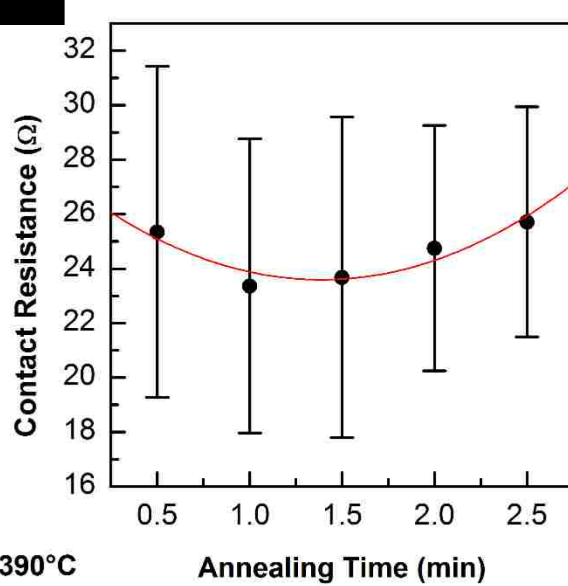

annealing temperature was studied from 380°C to 420°C with annealing time of 1min, and the contact resistance was measured for each annealing condition with the TLM structure in the way explained in the previous section.

Figure 4.3(a) shows the contact resistance as a function of annealing temperature. Based on this analysis, the contact resistance is minimum when the samples were annealed at 390°C. Then, the annealing time was varied from 30s to 2.5mins with the annealing temperature of 390°C to optimize the annealing time. The contact resistance of the samples annealed for 1 minute and 1.5 minute is the almost same as shown in Fig. 4.3(b). However, from the fitting curve, the optimal annealing time is determined to be 1.5 minute. Therefore, the annealing for all Ohmic contacts by AuGe/Ni/Au was carried out at 390°C for 1.5 minute. If both Ohmic and Schottky contacts were required for the same sample, Ohmic contacts were prepared and annealed at the optimized conditions first, and then, Schottky contacts were fabricated since annealing was not desired for Schottky contacts.

4.2. Hall Effect Measurements

4.2.1. Theory

Since E. H. Hall discovered the classical Hall effect in 1879 [102], the Hall effect measurements have been adopted in almost all laboratories because of the simplicity of the experiment and the importance of the information about the specimen that can be measured by the Hall effect, namely the type of carriers, mobility, and carrier density.

The mobility, μ, is a proportionality coefficient between the drift velocity, $\vec{v}$, and the electric field, $\vec{E}$, and defined as

$$\vec{v} = \mu\vec{E} . \tag{4.2}$$

Thus, the mobility characterizes how quickly electrons are transported in a metal or semiconductors in response to the electric field. The carrier density is just the number of carriers

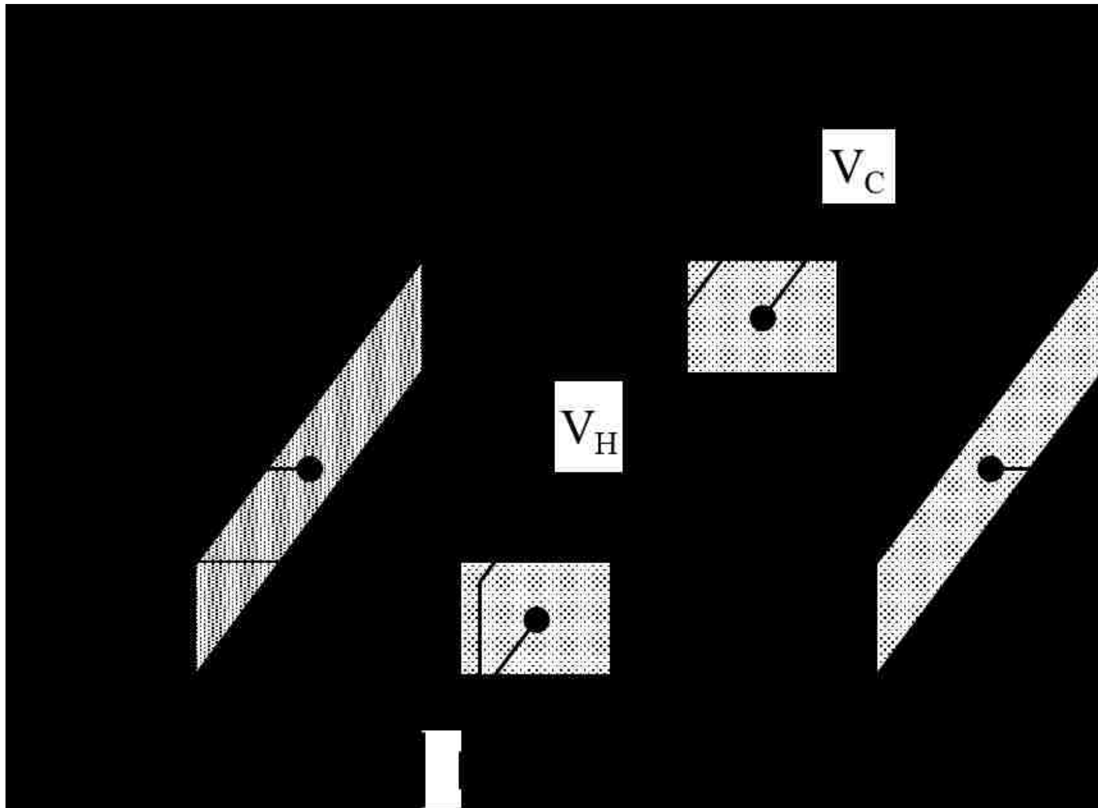

per unit volume. In semiconductors, there are two types of carriers, namely, negatively charged electrons and positively charged holes.

Hall effect measurements are illustrated in Fig. 4.4 where an electric field, E_y, is applied to an n-type semiconductor in the y-direction by a battery, and the magnetic field, B_z, is applied in the z-direction. Electrons in the semiconductor move in the negative y-direction with a drift velocity, v_y. If the electron density is n, the total current density, j_y, is

$$j_y = nqv_y \tag{4.3}$$

where q is the electron charge, and v_y is the y component of the drift velocity. Since the electrons move in the magnetic field, they experience a Lorentz force and deflect to the positive x-direction. The accumulation of the electrons at the positive x face creates an electric field, E_x, from the positive to negative x faces and continues until the force exerted by the x-direction electric field, E_x, due to the electron accumulation balances the Lorentz force. In this case, the x component of the net force on the electrons satisfies

$$-q\vec{v} \times \vec{B} - q\vec{E} = qv_y B_z + qE_x = 0\,. \tag{4.4}$$

By combining Eq. 4.3 and 4.4, the Hall coefficient, R_H, is defined as

$$R_H = \frac{E_x}{j_y B_z} = \frac{-v_y B_z}{j_y B_z} = -\frac{1}{j_y} \cdot \frac{j_y}{qn} = -\frac{1}{qn}\,. \tag{4.5}$$

Notice that if the majority carrier is holes, they also accumulate on the positive x face and create the electric field, E_x. However, E_x has an opposite sign to the case in which the electrons are the majority carrier. As a result, the Hall coefficient, R_H, is given by

$$R_H = \frac{E_x}{j_y B_z} = \frac{v_y B_z}{j_y B_z} = \frac{1}{j_y} \cdot \frac{j_y}{qp} = \frac{1}{qp} \tag{4.6}$$

where p is the hole density. Therefore, the sign of the Hall coefficient directly represents the type of carriers. Moreover, the Hall coefficient is

$$R_H = \frac{E_x}{j_y B_z} = \frac{V_H wt}{B_z I_y w} = \frac{V_H}{BI_y} \cdot t = -\frac{1}{qn} \tag{4.7}$$

where V_H is the voltage across the contact on the x-z planes and called the Hall voltage, I_y is the current in the y-direction, w is the width of the sample, and t is the thickness of the sample. Since the Hall voltage, the current in the y-direction, and the magnetic field can be measured, the Hall coefficient and the carrier density can be calculated experimentally. In many cases, the sheet electron density, n_{2D}, defined as $n_{2D}=nt$ is shown as measurement results.

Then, the mobility is calculated as

$$\mu = \frac{v_y}{E_y} = -\frac{j_y}{qnE_y} = \frac{j_y}{E_y} \cdot \frac{E_x}{j_y B_z} = \frac{1}{B_z} \cdot \frac{E_x}{E_y} = \frac{1}{B_z} \cdot \frac{V_H}{V_C} \cdot \frac{l}{w} \tag{4.8}$$

where V_C is the voltage across the contacts parallel to the current, and l is the distance between these two contacts as defined in Fig. 4.4. Hence, knowing the dimensions of the sample and contacts, one can calculate the mobility from the Hall effect measurements. For this reason, special structures such as Hall bars and Van der Pauw structures are prepared for the Hall effect measurements. Geometrical effects and correction due to the difference in geometries have been discussed elsewhere [93,94].

In general, measurements of the Hall voltage include several spurious voltages [94]. For instance, if the contacts for the Hall voltage measurements are not aligned perpendicular to the current, a voltage appears between the contacts even without a magnetic field. Moreover, if there is a temperature gradient between the contacts, a thermoelectric voltage shows up between these two contacts due to the Seebeck effect [103]. Even if there is no external temperature gradient, the sample can set it up by itself. Since the Lorentz force depends on the velocity of the carriers,

fast and hot carriers are deflected more than slow and cold carriers. Therefore, an internal temperature gradient is generated. This effect is called Ettingshausen effect [104]. All spurious voltages except Ettingshausen effect voltage can be eliminated by flipping the directions of the current and magnetic field and taking the average of these four measurements [94].

Simple room temperature Hall effect measurements provide the carrier density and the mobility of the samples, and performing temperature dependent measurements provided additional information about the sample such as the activation energy of carriers. The temperature dependence of the electron density is given by

$$\frac{n(n+N_a)-n_i^2}{N_d-N_a-n-n_i^2/n}=\frac{N_C}{g}\exp(-\frac{E_A}{k_BT}) \tag{4.9}$$

where N_a is the density of acceptors, n_i is the intrinsic carrier concentration, N_C is the effective density of states in the conduction band, g is the degeneracy factor for donors, and E_A is the activation energy of the donors [105]. Equation 4.9 can be simplified if N_a is negligibly small, which is the case for the samples studied in this thesis, as

$$n \approx \sqrt{\frac{(N_d-N_a)N_C}{g}}\exp(-\frac{E_A}{2k_BT})\ . \tag{4.10}$$

Hence, if the carrier concentration is plotted as a function of $1/T$ in the semilog scale, the plot should be linear, and the slope is $-E_A/2k_B$. This Arrhenius analysis enable us to calculate the activation energy from the slope of the carrier concentration.

4.2.2. Experimental Setup

Temperature dependent Hall effect measurements were carried out by the Lake Shore Hall Measurement System with the Janis 10K Closed Cycle Refrigerator system (CCS-450ST) using the Van der Pauw method as depicted in Fig. 4.5. After the growth of SF120, SF121, SF122, and SF123, the samples were cleaved into 5cm×5cm square pieces. At the four corners of

each sample, a small ball of indium (In) was applied, and the samples were annealed at 420°C for 2mins under N_2 ambient to form Ohmic contacts. For the Hall effect measurements, In was used to form Ohmic contacts instead of AuGe/Ni/Au for ease in sample preparation. Then, the samples were loaded into the cryostat and kept in a vacuum achieved by a turbomolecular pump. The temperature was controlled by the Lake Shore 340 Temperature Controller by adjusting the current through two heaters inside the cryostat. The Hall effect measurements were conducted between 295K and 8K in steps of 15K. For each measurement, a current of 10μA was supplied by the Keithley 220 Current Source to the sample through two contacts at diagonal corners with a magnetic field ramped up to 0.5T by an electromagnet, and the Hall voltage across the other diagonal contacts was measured by the Keithley 2182 Nanovoltmeter. Then, the contacts for the current supply and Hall voltage measurement were switched as well as the polarities of the magnetic field and current in order to eliminate spurious voltages which cause measurement errors as explained in the previous section. Finally, all the measured Hall voltages were averaged

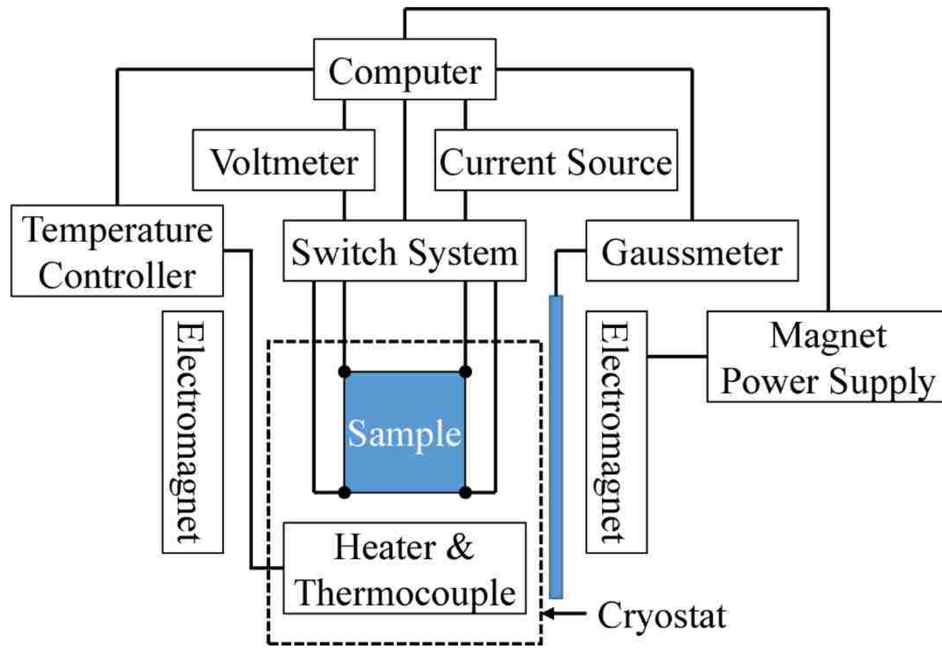

to determine the measurement value at each temperature. The entire measurement was controlled through the Lake Shore Hall Measurement System Software. From these measurements, the mobility and sheet carrier density of each sample at each temperature were calculated using the theory explained in Section 4.2.1.

4.2.3. Results and Analysis

The results of the temperature dependent Hall effect measurements for SF120, SF121, SF122, and SF123 are summarized in Fig. 4.6. As in Fig. 4.6(a), the QWs with nanoholes have higher mobility than the reference QW even though the QW with the deepest nanoholes have almost the same mobility as the reference QW over the entire temperature range. In addition to the mobility, the sheet carrier density increases with the depth of nanoholes. It is worth mentioning that the carrier density in QWs with nanoholes is higher than that of reference QW in the low temperature. This means that both mobility and carrier density can be tailored by controlling the depth of nanoholes. The physics behind the increase in the Hall mobility and

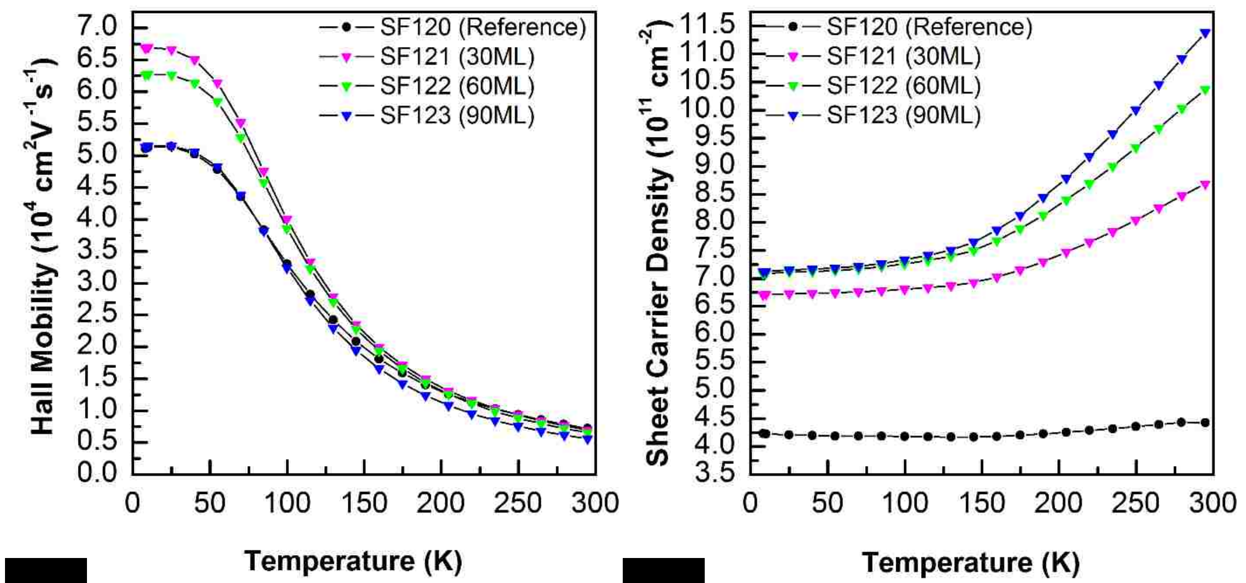

carrier density is not really clear. However, possible mechanisms which are consistent with physics are suggested.

In terms of the increase in carrier density, the effects of surface states or the possibility of metal Ga left inside nanoholes are considered. A concept of band structures and band gaps of semiconductors is based on an ideal infinitely large semiconductor. However, the assumption of an infinitely large semiconductor is not appropriate once the surface should be taken into account. The presence of a surface introduces new energy states in a band gap [106], and these surface states can be occupied by electrons. GaAs especially has a high density of surface states ($\sim 10^{12}$cm^{-2}eV^{-1}) [107]. Since the nanoholes bring the surface closer to the QW layer, these electrons occupying the surface states have a higher probability of tunneling and contributing to conduction in the QW. Hence, the carrier density can increase with the depth of nanoholes. If metal Ga is left inside the nanoholes, then electrons in the Ga droplets can contribute directly to conduction in the QW as well, and thus, the carrier density will also increase as observed.

Walukiewicz *et al.* modeled the electron density dependence of carrier mobility in a 2DEG for the modulation doped $Al_{0.3}Ga_{0.7}As$/GaAs heterojunction, and reported that the mobility of the electrons in the 2DEG increased with the carrier density up to about 8×10^{11}cm^{-2} and decreased with further increase of the carrier density [108]. Similar theoretical and experimental results have been reported in different material systems elsewhere [109–113]. In highly doped samples, ionized impurities are the main source of scattering the electrons in the 2DEG through the Coulomb interaction. However, the Coulomb interaction is screened out by rearranging the local density of the electrons in the QWs. The effect of this screening is determined by the Debye length, λ_D, which is given by

$$\lambda_D = \sqrt{\frac{\varepsilon_S k_B T}{q^2 n}} \tag{4.11}$$

where ε_S is the permittivity of the semiconductor, k_B is the Boltzmann constant, T is the temperature in kelvin, q is the electron charge, and n is the electron density [94]. Since the shorter Debye length indicates higher screening, the increase in the carrier density can also increases the mobility in the 2DEG. However, if nanoholes are too deep, they enhance scattering and degrade the mobility since the electrons in the 2DEG feel more electrons either in the negatively charged surface states or in metal Ga left in the nanoholes. To investigate these postulates, regrowing this set of samples and passivating the surface to reduce the density of surface states [107,114,115], and also take cross sectional transmission electron microscopy (TEM) pictures of the nanoholes are the next steps in this research.

One more distinct difference in the carrier density between the QWs with nanoholes and the reference QW is the slope of the curve above 200K. As explained in Section 4.2.1, the slope of the temperature dependent carrier density curve ***corresponds to the activation energy of carriers.*** Therefore, the activation energy of carriers in each sample is calculated based on the

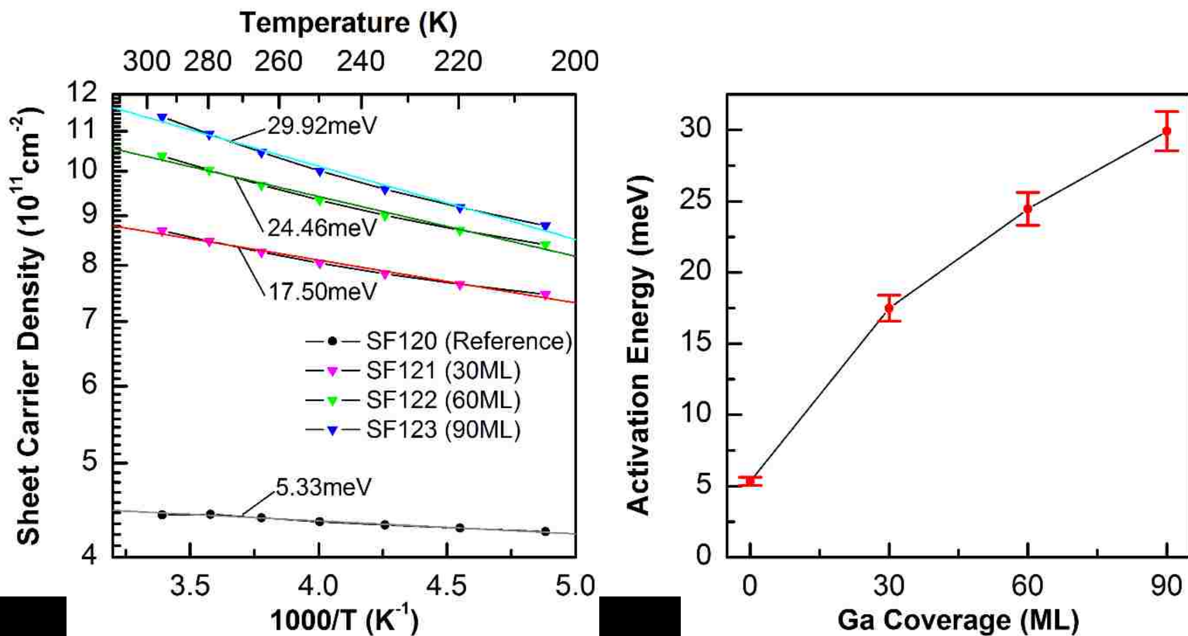

Arrhenius plots of the sheet carrier density in the way explained in Section 4.2.1. Figure 4.7(a) shows the Arrhenius plots of SF120, SF121, SF122, and SF123 between 200K and 300K, and the activation energies are shown as a function of the Ga coverage for the nanohole growth in Fig. 4.7(b). The activation energy of SF120 agrees with the previously reported values for Si doped AlGaAs [116,117]. It is clearly observed that the activation energy also increases with the depth of nanoholes. This observation implies that the nanoholes modify the energy spectrum of the samples and probably create new deep states so that the carriers need more energy to be activated. Since the Hall effect measurements are suitable for detecting shallow levels, deep levels created by the nanoholes are characterized by noise studies and discussed in Section 4.3.

In Section 4.2.1, I assumed that the Lorentz force on the carriers by the magnetic field balances with the electric field built up due to the accumulation of the carriers at the two sides. However, the balance between the Lorentz force and the electric field would be disturbed if there is metal Ga left inside the nanoholes since the metal Ga is a huge reservoir of electrons and creates an additional electric field. Therefore, in order to confirm the validity of our analysis, other electrical characterization such as Shubnikov-de Hass measurements are required [118–120]. Otherwise, a new set of samples should be grown to study how fast Ga droplets are consumed and make sure there is no Ga left inside the nanoholes, perhaps by cross sectional TEM. This set of samples may also answer whether our postulates about the increase in both the Hall mobility and carrier density are valid or not in case there is metal Ga left inside the nanoholes of the samples.

What we have learned in this section is that by using the temperature dependent Hall effect measurements, ***the nanoholes can modulate the mobility and electron density***. Indeed, the density of electrons increases with an increase in the nanohole depth. This increase is

suggested as a result of influence of surface states or possible Ga leftover inside the nanoholes. To distinguish the role of each possible mechanism, further experiments are required. At the same time, the increase in the electron mobility measured by the Hall effect is a result of the increase in the carrier density, which enhances the screening of the effects of the impurity donors and suppress the scattering of the electron in the QWs. For very deep nanoholes, the transport in the 2D channel degrades due to enhanced carrier scattering. The temperature dependent studies of the carrier density demonstrate changes in the energy spectra of the QW heterostructures, namely, that activation energies calculated from the Arrhenius plot show a consistent increase with the depth of the nanoholes. This behavior suggests the formation of electrically active deep states in the AlGaAs barrier layer.

4.3. Noise

4.3.1. Theory

Noise is spontaneous fluctuations in a current or voltage and is present in all semiconductor devices. Since noise determines the sensitivity and detection limits of devices, the effect of holes is investigated to understand if they improve transport but at cost of increased noise and a low signal to noise ratio that affects the performance of devices. Also, thanks to its sensitivity to deep levels and material qualities, noise can be a diagnostic tool for the characterization of these deep levels and material qualities. There are many noise sources, and the resulting noise is expressed as a superposition of noise due to these different sources [121]. Hence, in this section, the most important noise source-thermal noise, 1/f noise, and generation-recombination noise-are described. ***Perhaps surprisingly, we will learn that the noise actually improves with holes.***

4.3.1.1. Thermal Noise

Thermal noise, also known as Johnson-Nyquist noise after J. Johnson who first measured thermal noise in 1928 [122] and H. Nyquist who formulated thermal noise spectra [123], is due to random thermal motion of carriers and thus, unavoidable except at the absolute zero temperature. The concept of thermal noise was first proposed by Einstein in 1906 based on Brownian motion of carriers [124]. The noise power spectral density of thermal noise in voltage, $S_{V,\,Th}$, is given by

$$S_{V,\,Th}=4k_BTR \tag{4.12}$$

where k_B is the Boltzmann constant, T is the absolute temperature of the sample in kelvin, and R is the sample resistance [93]. Since thermal noise is independent of frequency, it is also called a white noise. If the resistance is known accurately, thermal noise can be used to measure the temperature of the sample based on Eq. 4.12.

4.3.1.2. 1/f Noise

1/f noise, also known as flicker noise, was first observed in vacuum tubes in 1925 [125]. The noise spectral density of this noise is inversely proportional to frequency, and thus, 1/f noise dominates at low frequencies. There are still controversial arguments about the sources of 1/f noise. One of two competing models is based on the fluctuation of number of carriers developed by A. L. McWhorter [126]. In simple terms, McWhorter proposed that 1/f noise is a superposition of many different spectra of generation-recombination noise, which is explained in the next section. The other model proposed by F. N. Hooge is based on the fluctuation of mobility [127]. In his model, Hooge assumed that the source of 1/f noise is scattering on crystal lattices, not on impurities, and derived the voltage noise spectral density, $S_{V,\,1/f}$, as

$$S_{V,1/f} = \frac{\alpha V^2}{Nf} \tag{4.13}$$

where α is the Hooge parameter, V is an applied voltage, N is the total number of carrier, and f is frequency [128]. Therefore the 1/f noise spectrum is a straight line with an apparent slope of -1 in the log-log scale as shown in Fig. 4.8(a). From the definition, the Hooge parameter is 1/f noise created by one electron at each frequency and depends on the quality of a crystal. In general, the McWhorter model is applied to metal-oxide-semiconductor field effect transistors while the Hooge model is used for bipolar junction transistors [121].

4.3.1.3. Generation-Recombination Noise

Generation-Recombination (GR) noise is due to the fluctuation of number of carriers caused by GR process between the bands and trap centers in the band gap. The fluctuation of carriers creates noises in conduction and thus, voltage and current. GR noise is characterized by a characteristic time constant, τ, of each trap center. This time constant, τ, is expressed by

$$\frac{1}{\tau} = \frac{1}{\tau_e} + \frac{1}{\tau_c} \tag{4.14}$$

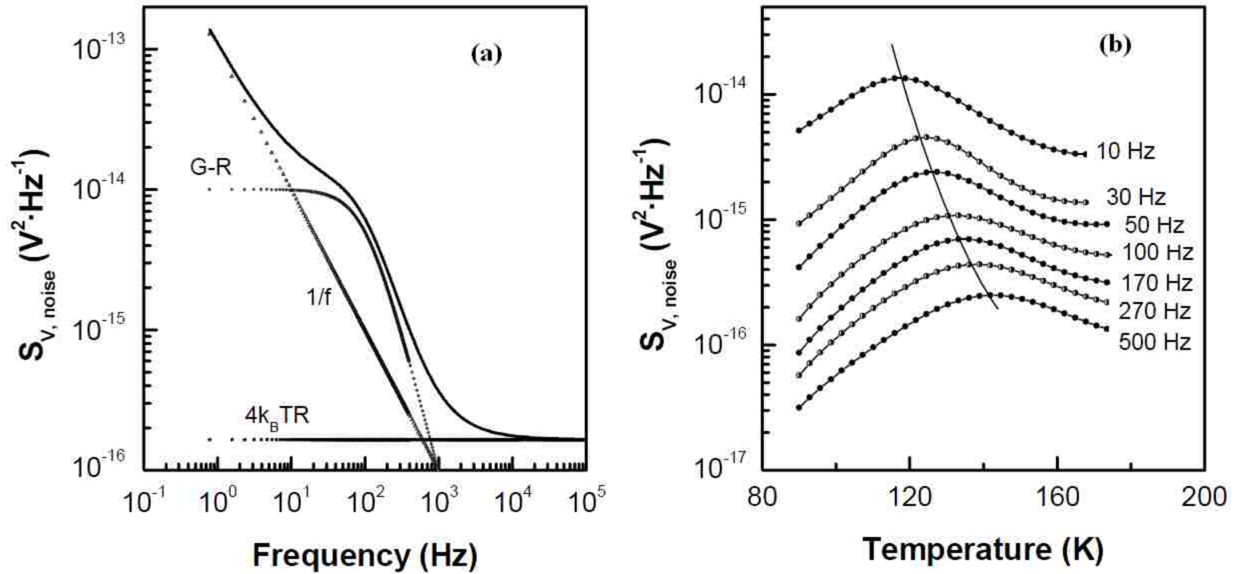

where τ_e is the time constant for emission from the trap and τ_c is the time constant for capture. Thus, if there are several trap centers in the sample with different time constants, their contribution to the noise is also different. The noise spectral density for GR noise, $S_{V, GR}$, is expressed as a superposition of noises due to different traps such as

$$S_{V,GR} = \sum_i \frac{B_i}{1+(f/f_i)^2} \tag{4.15}$$

where B_i is the amplitude of ith GR noise, f_i is the corner frequency of ith GR noise and $f_i=1/(2\pi\tau_i)$. Hence, the noise spectrum curve for each ith GR noise as a function of frequency in the log-log scale has a plateau at $S_V=B_i$ below the corner frequency and decreases linearly with a slope of -2 above the corner frequency as shown in Fig. 4.8(a).

Levinshtein and Rumyantsev investigated GR noise further and developed a method of noise spectroscopy known as deep level noise spectroscopy in order to characterize trap centers in the case of their electron capture cross sections, σ, depending exponentially on temperature [129–131]. In this case, the electron capture cross section of a deep level whose trap density is N_t can be expressed as

$$\sigma=\sigma_0\exp(-E_1/k_BT) \tag{4.16}$$

where σ_0 is an pre-exponential factor and E_1 is the emission activation energy. Then, the capture time constant is

$$\tau_c=\tau_{c0}\exp(E_1/k_BT) \tag{4.17}$$

where τ_{c0} is an pre-exponential factor.

Assuming the deep level is far below the Fermi level, the GR relative noise spectral density due to the deep level is given by [129]

$$S = \frac{4N_t}{VN_d^2}\tau_{c0}\frac{N_C}{N_d}\frac{\exp[(E_1-E_0)/k_BT]}{1+\omega^2\tau_{c0}^2\exp(2E_1/k_BT)} \tag{4.18}$$

Where N_t is the density of the deep level, V is the volume of the sample N_d is the donor density, N_C is the effective density of states in the conduction band, E_0 is the energy level of the deep level with respect to the conduction band minimum, and ω is the angular frequency $\omega=2\pi f$. If the relative noise spectral density, S, is plotted as a function of temperature, the noise density has a peak with S_{Max} at T_{Max} as in Fig. 4.8(b). T_{Max} can be determined by differentiating Eq. 4.18 with respect to $1/T$ and setting the derivative equal to zero. Then, if $E_1>E_0$, we have

$$\frac{1}{k_B T_{Max}} = \frac{1}{2E_1} \ln \frac{E_1 - E_0}{(E_1 + E_0)\omega^2 \tau_{c0}^2} \tag{4.19}$$

or

$$\frac{1}{k_B T_{Max}} = \frac{1}{2E_1} \ln \frac{E_1 - E_0}{(E_1 + E_0)\tau_{c0}^2} - \frac{1}{E_1} \ln \omega\,. \tag{4.20}$$

The max noise density, S_{Max}, at $T= T_{Max}$ is

$$S_{Max} = \frac{4N_t}{VN_d^2} \tau_{c0} \frac{N_C}{N_d} \frac{(a/\omega^2 \tau_{c0}^2)^{(E_1-E_0)/2E_1}}{1+a} \tag{4.21}$$

where $a=(E_1-E_0)/(E_1+E_0)$.

Then,

$$\ln S_{Max} = \ln\left(\frac{4N_t}{VN_d^2} \tau_{c0} \frac{N_C}{N_d} \frac{(a/\tau_{c0}^2)^{(E_1-E_0)/2E_1}}{1+a} \right) - \frac{E_1 - E_0}{E_1} \ln \omega\,. \tag{4.22}$$

Therefore, from Eq. 4.20 and 4.22, the slope of $1/k_B T_{Max}$ versus $\ln\omega$ is $-1/E_1$, and the slope of $\ln S_{Max}$ versus $\ln\omega$ is $-(E_1-E_0)/E_1$. This means that E_1 and E_0 can be calculated from the slopes of these two plots.

4.3.2. Experimental Setup

For the noise measurements, the Greek Cross structure was prepared on all four samples using standard photolithography as explained in Section 4.1.3. The detail of the fabrication is summarized in Table 4.1, and SEM pictures of the Greek Cross structure are shown in Fig. 4.9. The photolithography mask used for the Greek Cross structure have the TLM structure as well. Hence, the contact resistance was measured before the noise experiments and confirmed below 20Ω for all samples.

After the fabrication and the contact resistance measurements, the samples were loaded into the MMR D2500 cryostat and kept in a vacuum achieved by a mechanical pump. Two

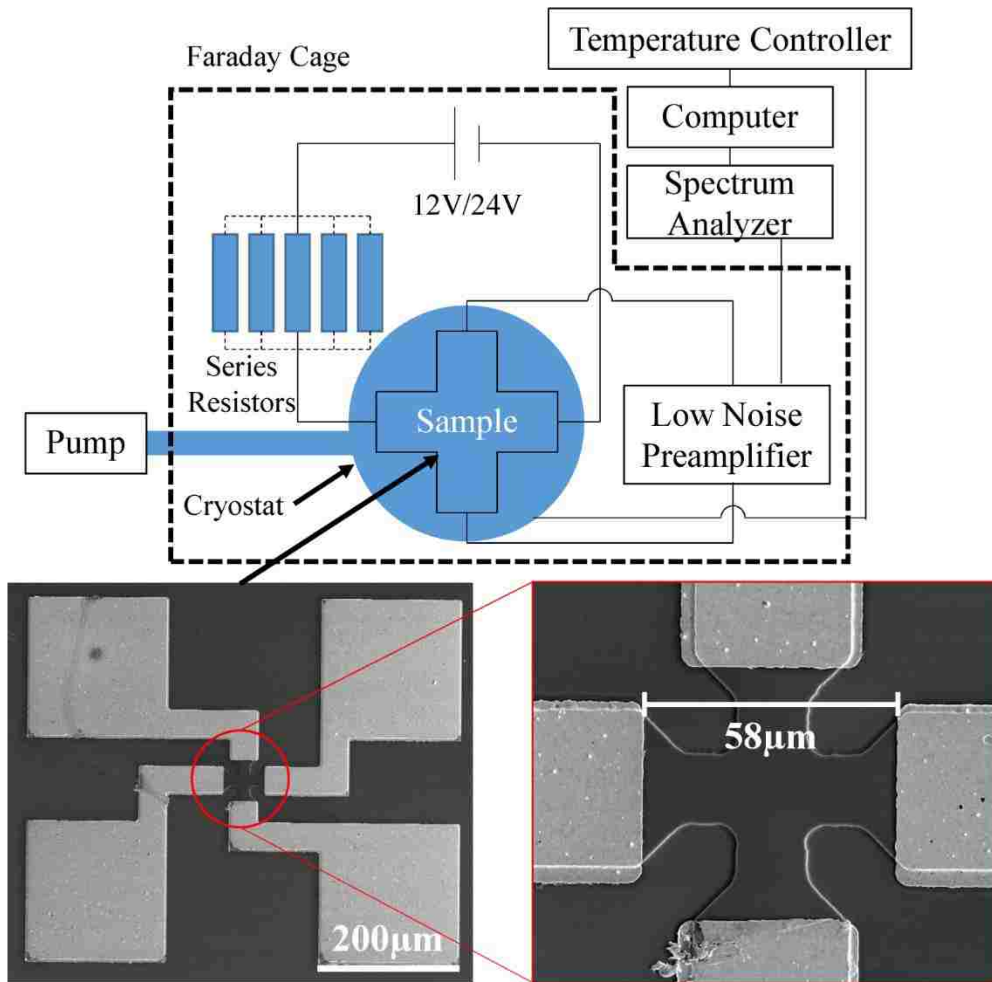

contacts on the opposite arms of the Greek Cross structure were connected to the DC 12/24V power supply with a load resistance in series, and the other two opposite contacts were connected to the SRS low noise voltage preamplifier (SR560). The amplified signal was fed into the SRS spectrum analyzer (SR785), and the data were acquired by the program written in LabView (National Instruments). The cryostat was cooled down by Joule-Thomson cooling with ultra-high purity N_2 gas flowing in the capillaries in the cryostat [132–134], and the temperature inside the cryostat was controlled by computer program through the MMR K-20 programmable temperature controller by adjusting the heater power. To remove undesired interfering noises from external sources, all the devices except the computer, temperature controller, and spectrum analyzer were placed in the Faraday cage. The entire setup is illustrated in Fig. 4.9.

TABLE 4.1. Details of lithography to fabricate Greek Cross structures for noise measurements.

	Step Description	Details
1	Surface Cleaning	Acetone, Methanol, and IPA in 5mins each with ultrasonication
2	Photoresist Application	AZ4330 with 5000rpm (Thickness=3.7μm)
3	Baking	110°C for 3mins
4	Exposure	9.5s with a mask of Greek Cross and TLM for mesa definition
5	Development	AZ400K:H_2O (1:3) in 1min 45s
6	Etching	H_3PO_4: H_2O_2: H_2O (1:1:20) for 2min 30s (Depth=470nm)
7	Photoresist Removal	Acetone, Methanol, and IPA in 5mins each with ultrasonication
8	Photoresist Application	AZ4330 with 5000rpm (Thickness=3μm)
9	Baking	110°C for 3mins
10	Exposure	9.5s with a mask of Greek Cross and TLM for metallization
11	Development	AZ400K:H_2O (1:3) in 1min 45s
12	Etching	HCl:H_2O (1:1) for 15s (surface oxide)
13	Metallization	AuGe/Ni/Au (100nm/20nm/200nm)
14	Lift off	Acetone at 40°C for 100mins with ultrasonication
15	Annealing	390°C for 1min 30s under N_2 ambient

In order to measure the noise spectra, the voltage was applied across the two opposite arms, and the voltage fluctuations across the other opposite arms were measured. The preamplifier applied a filter which passes signals within the frequency range of 3Hz to 300kHz and amplified them by 1000 times. Then, the measured voltage signals in time domain were

transformed into frequency domain by the Fast Fourier Transformation (FFT). The spectrum analyzer allows measurements of the noise power spectral density in frequency range of 1Hz and 102.4kHz [135]. To obtain accurate data, the measurement was repeated 200 times, and the average values of the 200 measurements were acquired by the computer.

For the room temperature noise studies, the voltage applied to the samples was varied by changing a resistance of series resistors between 82kΩ and 1MΩ, and the voltage noise spectra were measured with each series resistor. For the temperature dependent noise studies, the series resistor was fixed to 82kΩ, and the voltage noise spectra were measured between 85K and 445K in steps of 15K. After the measurements, the resistance between two opposite arms of the Greek Cross devices for both configuration was measured in the same temperature range. Voltages applied across the Greek Cross devices can be calculated for further analysis of the noise spectra.

The apparent measured noise contains noise due to the cables, a load series resistance, amplifier, and spectrum analyzer as well as the samples. Therefore, the measured voltage noise spectra are given by

$$S_{V,\ Total} = S_{V,\ Sample} + S_{V,\ Cables} + S_{V,\ Analyzer} + S_{V,\ Amplifier} \tag{4.23}$$

where $S_{V,Total}$, $S_{V,Cables}$, $S_{V,Analyzer}$, and $S_{V,\ Amplifier}$ are the voltage noise spectral densities of the measured total signals, sample, cables, spectrum analyzer, and low noise preamplifier, respectively. In order to extract the noise spectrum due to the samples only , the noise level of our apparatus must be obtained, which can be done experimentally by measurements of the noise spectra of a known resistor and a shorted input of the preamplifier [136–138]. Then, the voltage noise spectrum of the sample can be extracted from

$$S_V = \frac{S_{V,Total} - S_{V,Short}}{S_{V,CalR} - S_{V,Short}} \cdot 4k_B T R_{CalR} \tag{4.24}$$

where R_{CalR} is the resistance of the calibration resistor, $S_{V, Short}$, $S_{V,CalR}$ are the voltage noise spectra of a shorted input of the preamplifier and the calibration resistor, respectively.

4.3.3. Results and Analysis

4.3.3.1. Room Temperature Noise

The room temperature noise spectra for SF120, SF121, SF122, and SF123 for different applied voltages are shown in Fig. 4.10. The voltage noise spectral density decreases with a

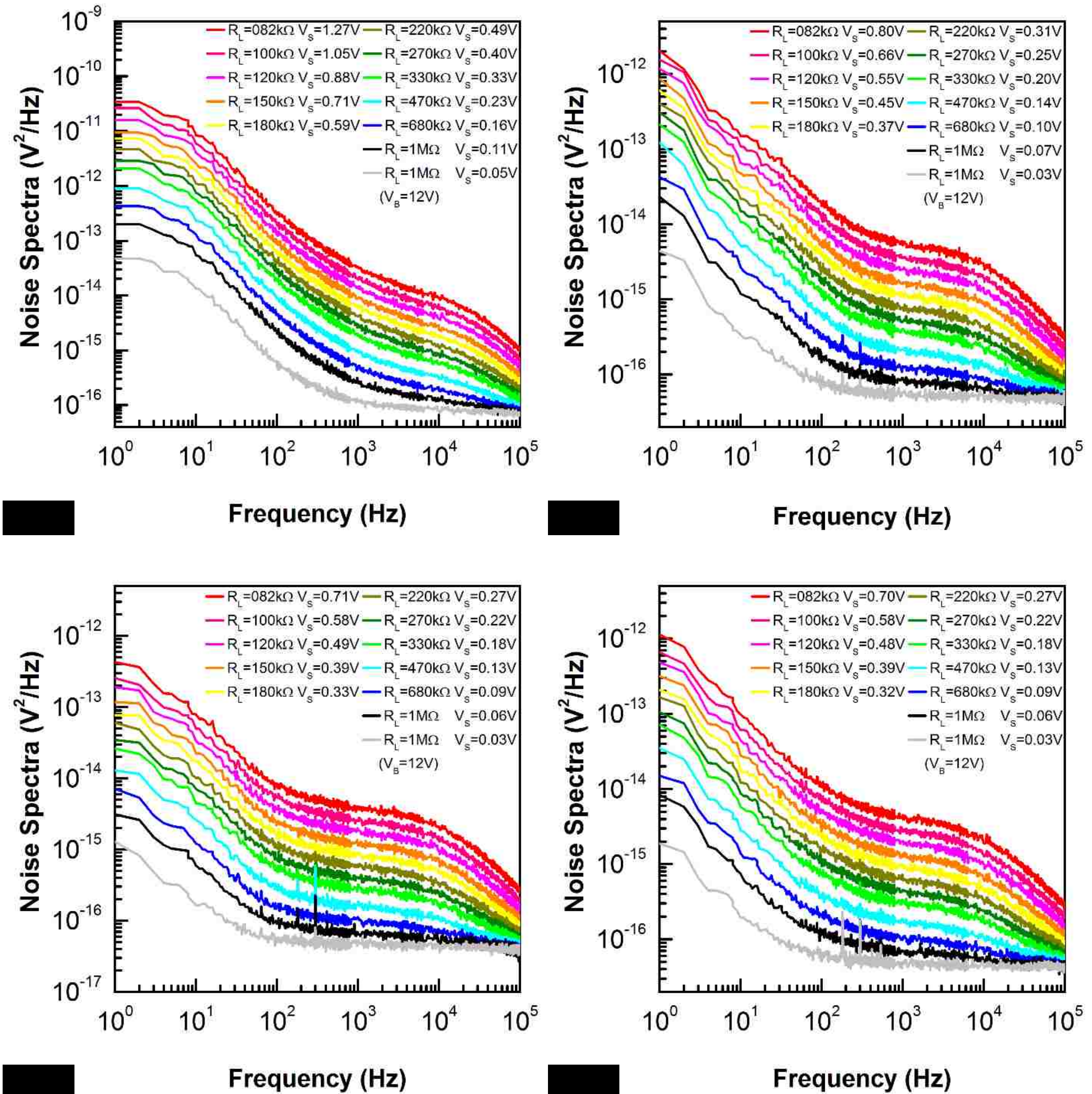

frequency increase and converges to a certain value at high frequency. Also, two shoulders are detected in the noise spectra which indicate the presence of GR noises due to electrically active two traps at different energies inside of the structures. Therefore, the voltage noise spectrum can be described by Eq. 4.15 as

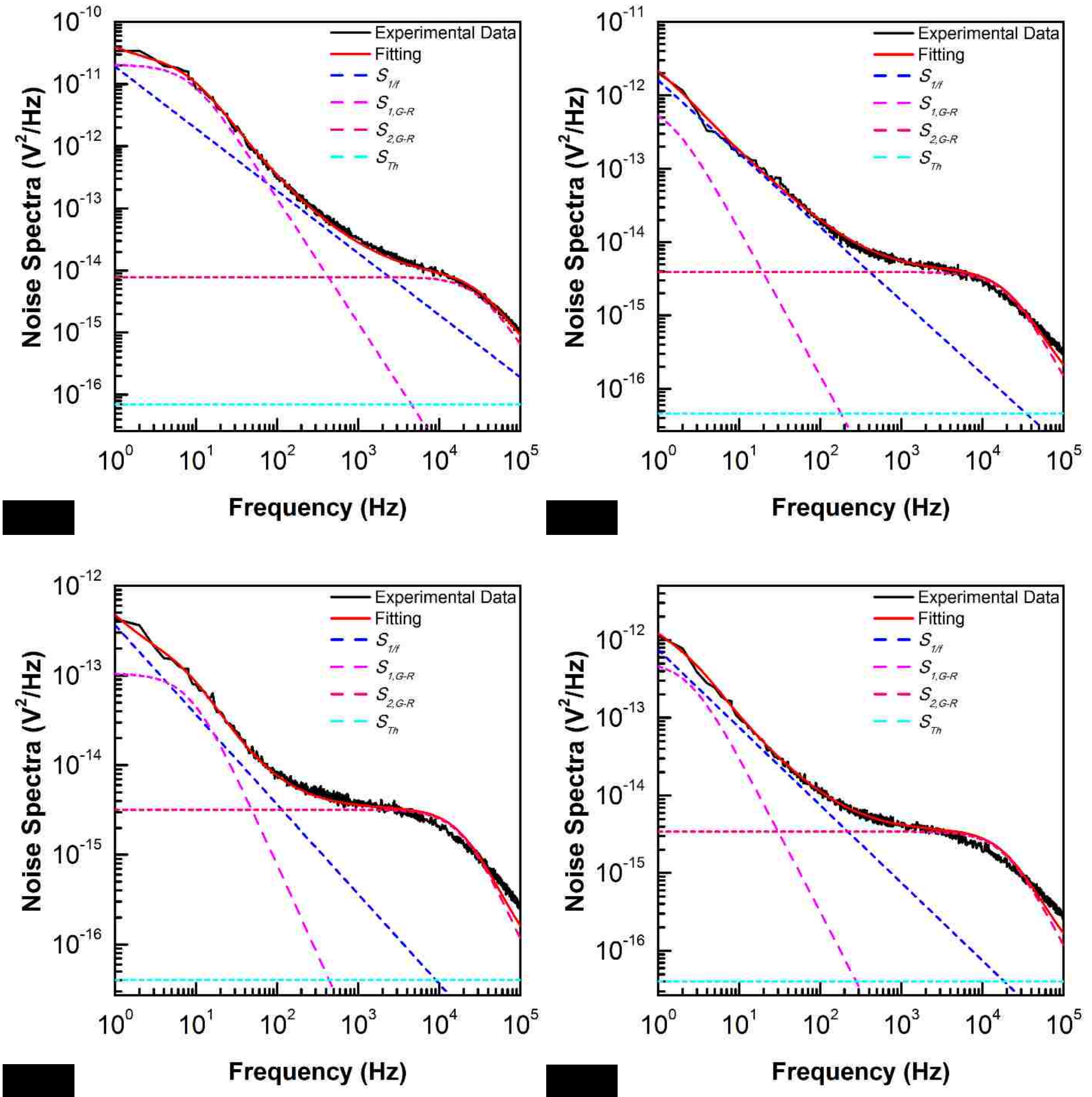

$$S_V = \frac{A}{f} + \frac{B_1}{1+(f/f_1)^2} + \frac{B_2}{1+(f/f_2)^2} + 4k_B TR \quad (4.25)$$

where f is frequency, A, B_1, and B_2 are the amplitudes of 1/f noise, the 1st GR noise, and 2nd GR noise, respectively, f_1 and f_2 are the corner frequencies of the 1st GR noise and 2nd GR noise, respectively, k_B is the Boltzmann constant, T is the temperature of the measurement, and R is the sample resistance. To deconvolute the measured noise spectra into each component and analyze each type of noise in detail, all the noise spectrum curves were fitted by using Eq. 4.25 with A, B_1, B_2, f_1, and f_2 as variables. Figure 4.11 is the examples of the noise spectrum fitting.

Comparing Eq. 4.13 and Eq. 4.25, the amplitude, A, of the 1/f noise is given by

$$A = \frac{\alpha V_S^{\ 2}}{N} \quad (4.26)$$

where N is the total number of carriers, Vs is the voltage applied to the sample, and α is the Hooge parameter. Here, the number of carriers, N, is not the carrier density measured in the Hall effect measurements. The total number of carriers involved in the noise spectrum measurements was calculated from

$$N = \frac{A_S}{qR\mu} \quad (4.27)$$

where As is the active area of the device, q is the electron charge, R is the sample resistance, and μ is the mobility of the sample. For the calculation of the Hooge parameter, the mobility measured by the Hall effect was used. From Eq. 4.26, the Hooge parameters can be calculated by plotting A as a function of V_S^2 and fitting the data linearly.

Plots of A as a function of V_S^2 and their linear fit for all four samples are shown in Fig. 4.12. The Hooge parameter, α, was calculated for each sample as a product of the total number of carriers, N, and the slope of the liner fit (see Eq. 4.26). The voltage range of each curve is

different since the resistance of each sample is different, and thus the voltage applied to each sample is also different even when using the same load resistors.

The Hooge parameter as a function of Ga coverage is plotted in Fig. 4.13. All QW samples with nanoholes have smaller Hooge parameters than the reference QW. As explained in

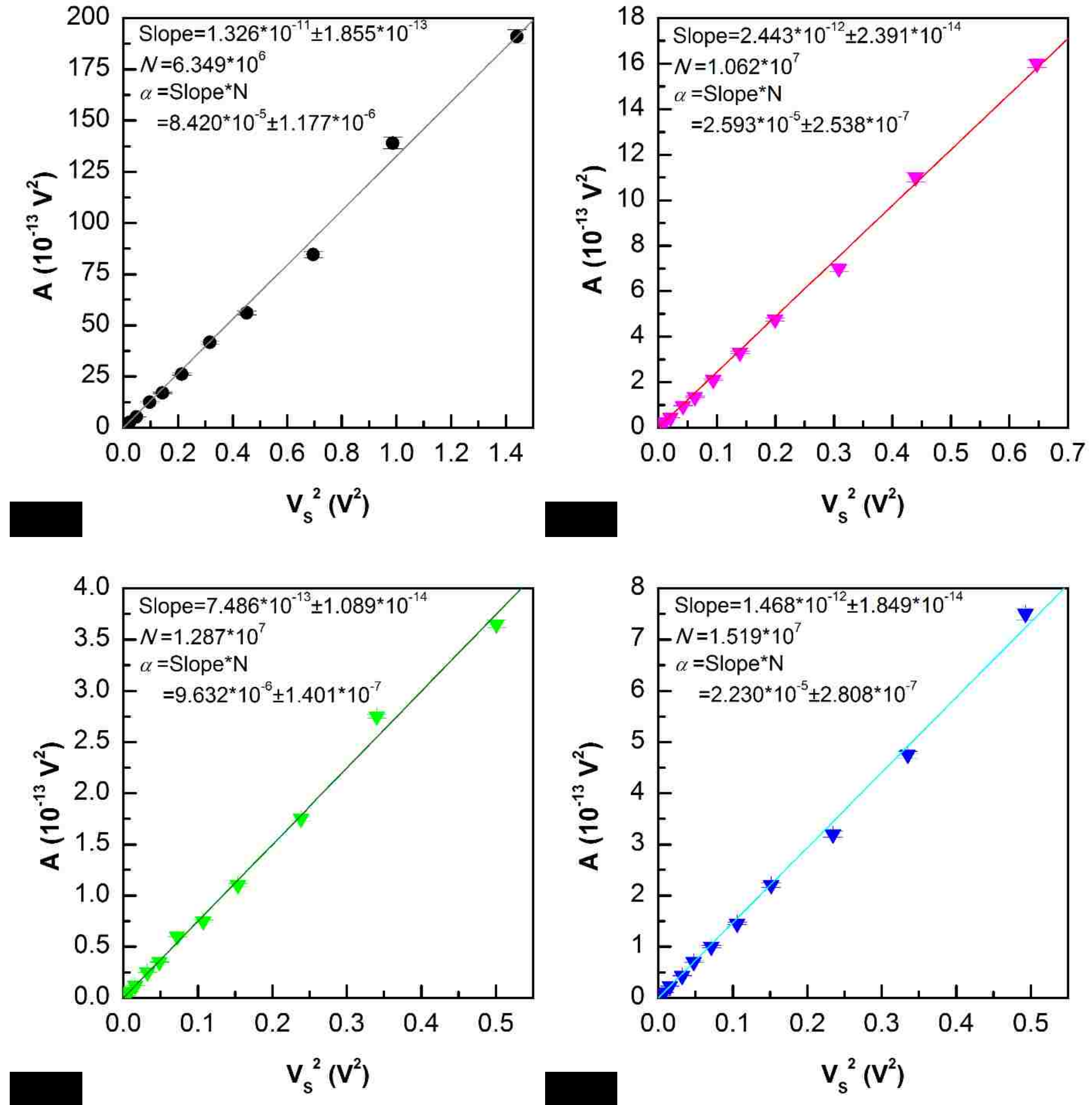

Section 4.3.1.2, the Hooge parameter is the amount of 1/f noise created by one electron at each frequency, and thus the contribution of an electron in the samples with nanoholes to the 1/f noise is smaller than that in the reference QW. Moreover, 1/f noise is inversely proportional to the number of carriers in the device as shown in Eq. 4.25 and Eq. 4.26. According to the Hall effect measurements in Section 4.2.3, the nanoholes lead to an increase in the carrier density in the QW. Hence, for the same area of the device, the increase in the carrier density by nanoholes further enhances the reduction of the 1/f noise. Therefore, the nanoholes reduce the 1/f noise in the QW. At the same time, the Hooge parameter exhibits the minimum at the coverage of 60ML. This means that if nanoholes are too deep and too close to the QW, they can cause an opposite effect and lead to an increase in 1/f nose even though the noise is still smaller than the reference sample. To take advantage of nanoholes to minimize the 1/f noise to the full extent, optimization of the depth of nanoholes with more data points should be carried out, and even deeper nanoholes or nanoholes penetrating the active InGaAs QW layer are desired in order to study effects of the nanoholes on the QW heterostructures in more detail.

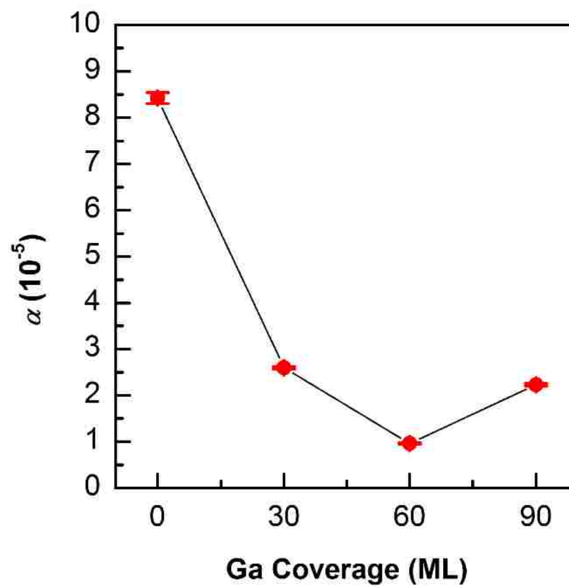

4.3.3.2. Temperature Dependent Noise

In the last section, the 1/f noise was characterized through the room temperature noise measurements. To investigate the GR noise, the room temperature noise measurements are not sufficient since the GR noise has both the temperature and applied voltage dependence. As

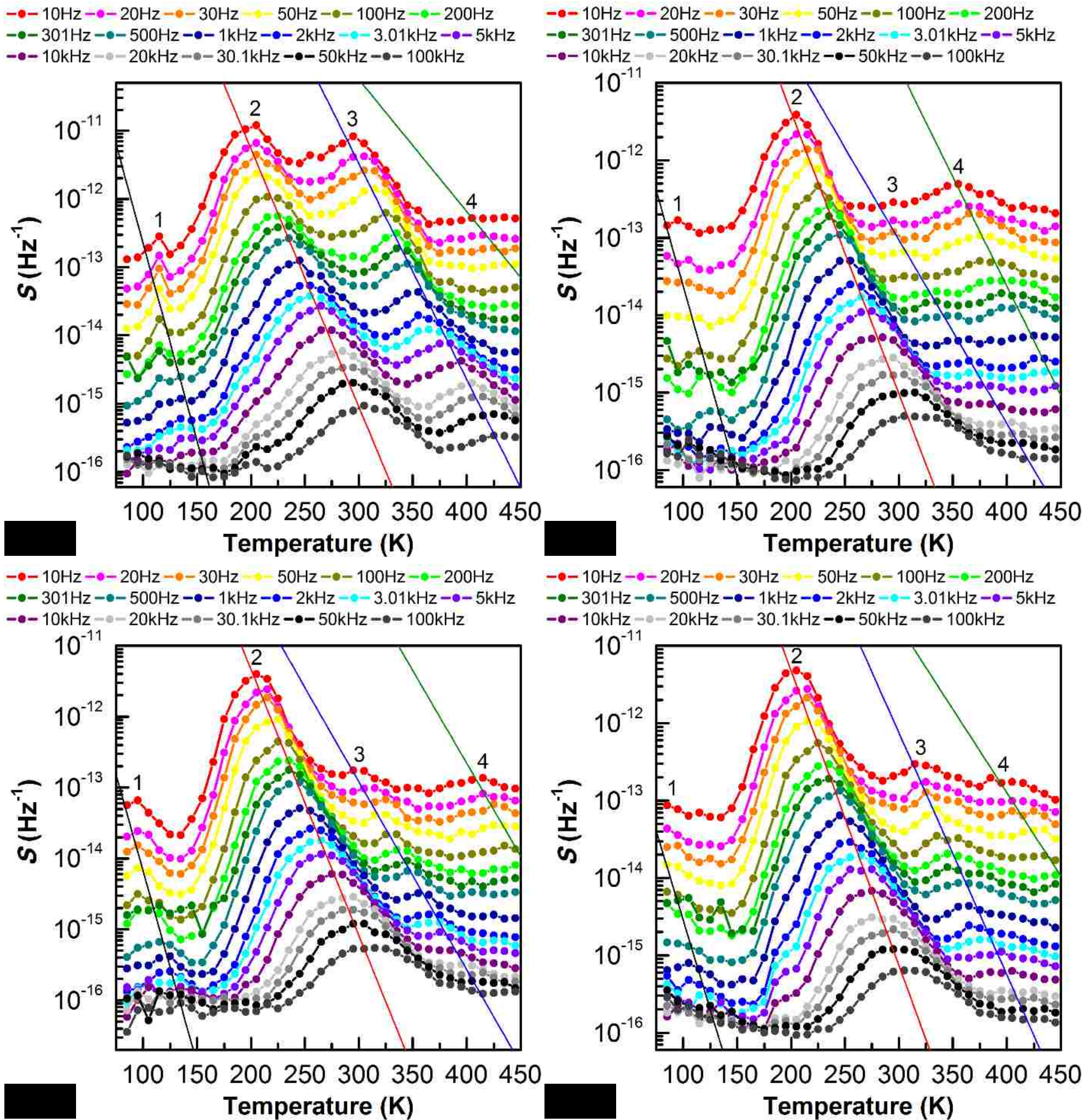

explained in Section 4.3.1.3, the GR noise due to a trap center shows a peak if its relative noise spectral density is plotted as a function of temperature (see Fig. 4.8(b)). If this peak does not show up around room temperature, this trap center does not contribute to the total noise as an active GR noise source at room temperature. In this case, the GR noises caused by such a trap center by the room temperature measurements cannot be obtained. Therefore, in order to characterize more deep levels, the temperature dependent noise measurements were required.

The temperature dependent noise measurements are summarized in Fig. 4.14. All samples show one distinct peak between 200K and 300K and small peak at low temperature. These two peaks are named Peak 2 and Peak 1, respectively. The reference sample SF120 has another distinct peak between 300K and 400K, which is named Peak 3. The other three samples with the nanoholes also have Peak 3 in the same temperature range, but the ratio of Peak 3 to Peak 2 is dramatically decreased. Hence, around room temperature, the deep levels corresponding to Peak 2 and Peak 3 were detected as GR noise sources. This observation agrees with the results of the room temperature measurements, which show two GR noises. At high temperature, one more small peak is observed especially in the QW with nanoholes, which is named Peak 4. In the reference sample, it is hard to define Peak 4. This indicates that the nanoholes enhance the noise level of Peak 4. However, it is worth mentioning that it is difficult to observe Peak 4 in the reference sample even though it has the same magnitude as Peak 4 in the samples with the nanoholes since the base noise level in the reference sample is higher than the magnitude of Peak 4 in the samples with the nanoholes.

The noise spectra of SF120, 121, 122, and 123 in the temperature domain were analyzed as explained in Section 4.3.1.3 to characterize deep levels in the samples. The peak values of the relative noise spectra, S_{Max}, and its peak positions, T_{Max}, were determined by fitting each curve in

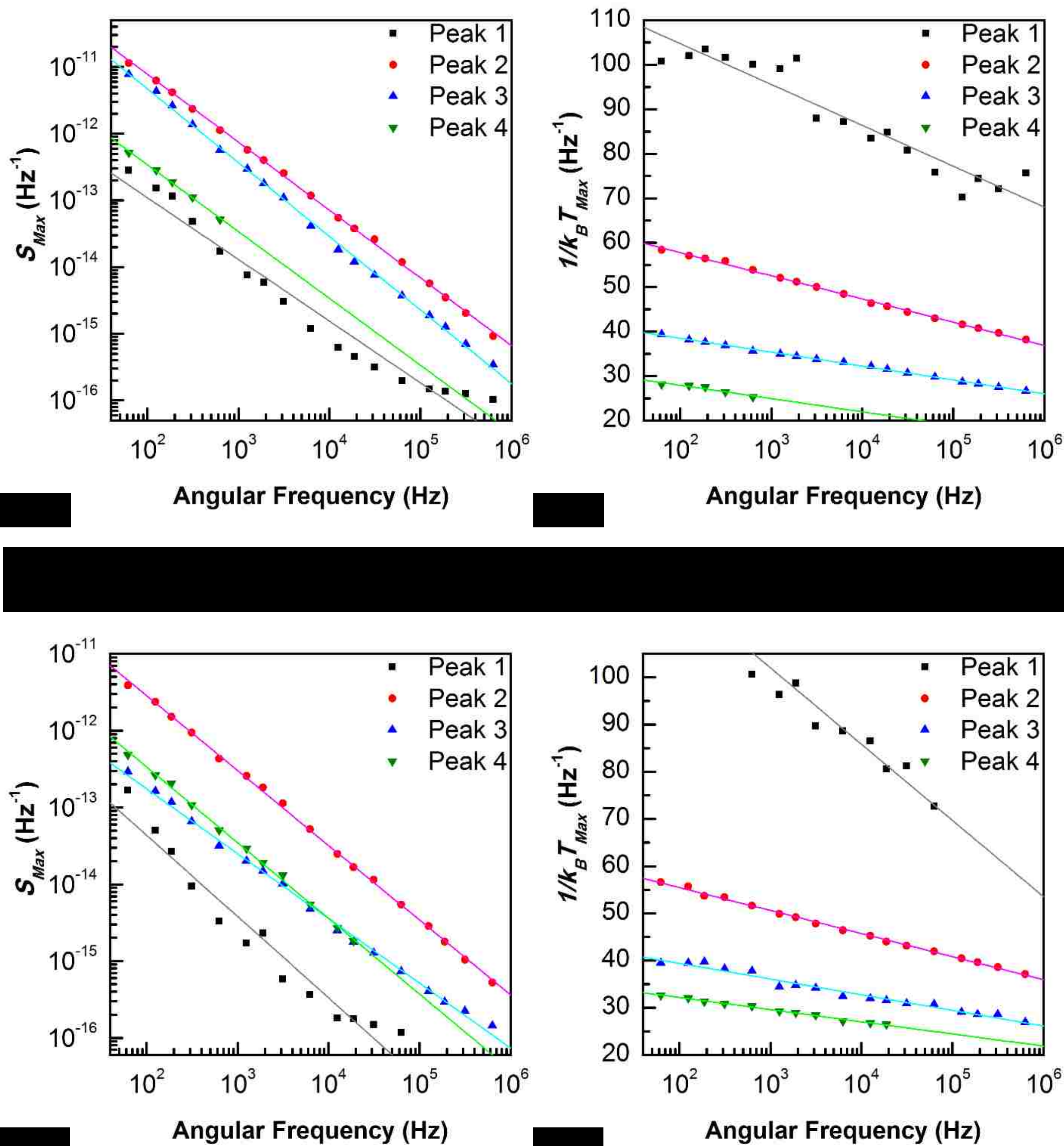

Fig. 4.14 using the Lorentzian function. S_{Max} and $1/k_BT_{Max}$ of all peaks as a function of angular frequency, ω, for SF120, 121, 122, and 123 are plotted in Fig. 4.15, Fig. 4.16, Fig. 4.17, and Fig.

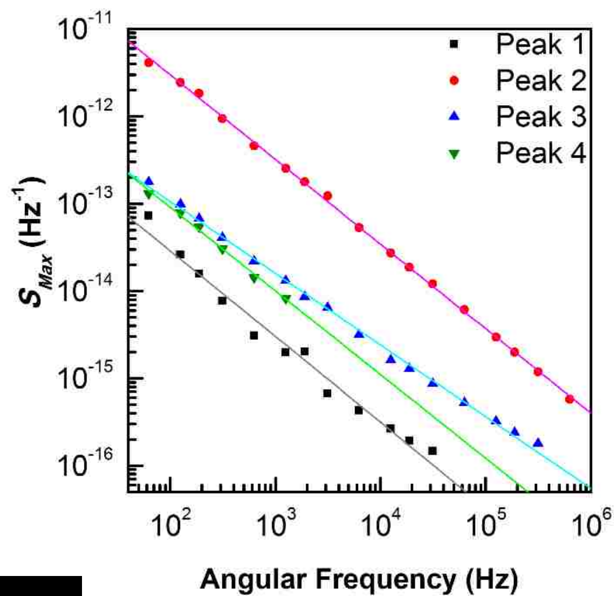

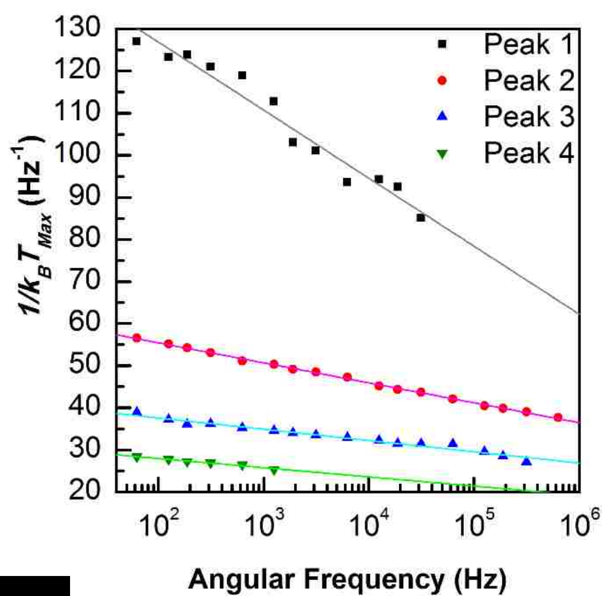

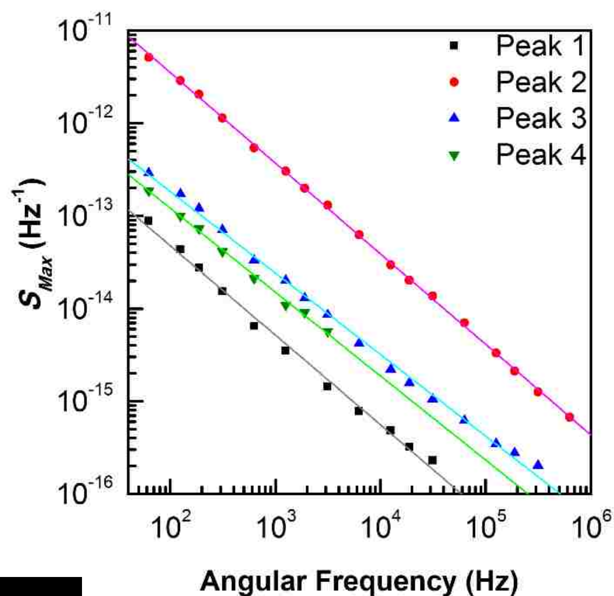

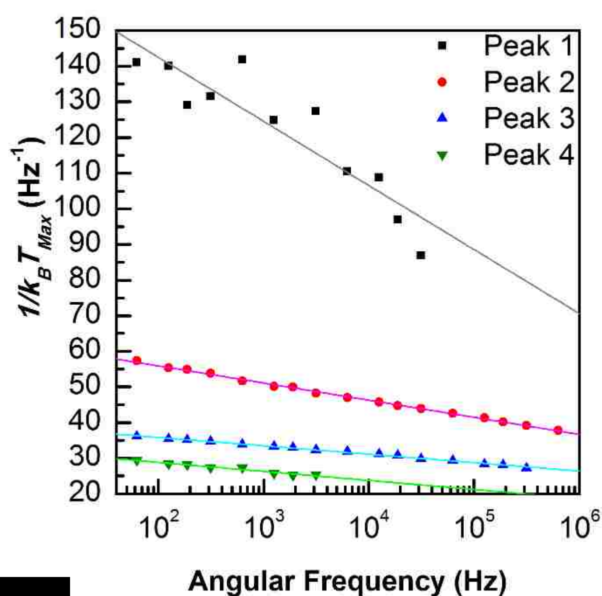

4.18, respectively. For Peak 1 and Peak 4, peaks could not be defined at some frequencies since they were out of the temperature range. This is why Peak 1 and Peak 4 have fewer data points.

From the slope of the linear fits of the S_{Max} and $1/k_BT_{Max}$ plots, the activation energy for each trap was calculated for all samples and for all peaks as explained in Section 4.3.1.3. The slope of each curve and corresponding energy is summarized in Table 4.2 and Fig. 4.19. As shown in Table 4.2, all peaks of all samples have the slope of the S_{Max} plot close to -1. According to Levinshtein *et al.*, in this case, the energy level positions, E_0, of the traps cannot be estimated accurately [129,130]. Hence, the activation energies, E_1, are used to characterize the deep levels which contribute to the GR noises.

TABLE 4.2. Summary of slopes of S_{Max} and $1/k_BT_{Max}$ plots and E_1 for all samples and all peaks.

Sample	Ga Coverage (ML)	Slope of S_{Max} Plot				Slope of $1/k_BT_{Max}$ Plot			
		Peak 1	Peak 2	Peak 3	Peak 4	Peak 1	Peak 2	Peak 3	Peak 4
SF120	0	-0.926	-1.018	-1.105	-1.003	-9.182	-5.233	-3.123	-2.983
SF121	30	-1.059	-0.974	-0.844	-0.987	-16.15	-4.896	-3.316	-2.570
SF122	60	-0.982	-0.969	-0.822	-0.959	-16.16	-4.745	-2.677	-2.182
SF123	90	-0.968	-0.978	-0.881	-0.907	-17.97	-4.806	-2.353	-2.530

Sample	Ga Coverage (ML)	E_1 (meV)			
		Peak 1	Peak 2	Peak 3	Peak 4
SF120	0	250.8	434.0	737.2	772.0
SF121	30	142.6	470.3	694.4	895.8
SF122	60	142.5	485.3	860.0	1055.4
SF123	90	128.2	479.1	978.7	910.2

Earlier works by DLTS [139–141] and deep level noise spectroscopy (DLNS) [142] reported that the DX center in Si doped AlGaAs has an emission activation energy of about 430meV. Since the activation energy, E_1, of Peak 2 agrees well with this earlier reported value of the DX center, Peak 2 is identified as the GR noise due to the DX center in the Si doped AlGaAs barrier. The amplitude of this noise spectral density due to this trap was relatively constant for all samples. This suggests that the nanoholes do not affect the DX center effectively because of its nature. It is known that the DX center in Si doped AlGaAs is associated with the L valley of the

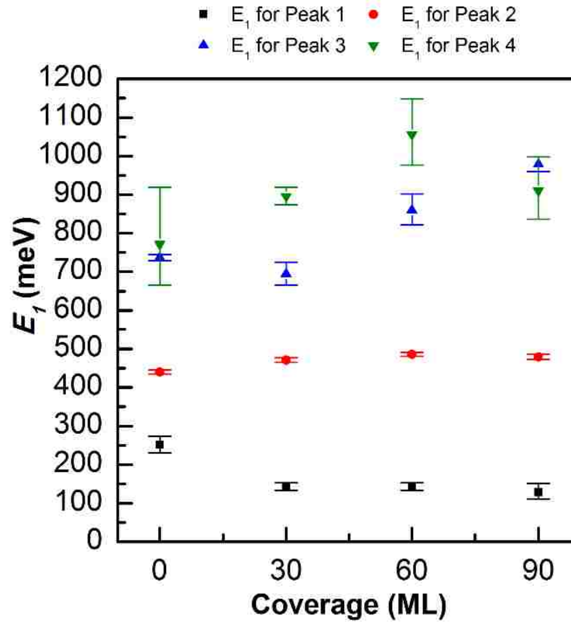

band structure instead of the Γ valley [116,139]. This implies that the noise measured in the conductivity is most sensitive to GR process of carriers with respect to the Γ valley.

Peak 3 of the reference QW SF120 has an emission activation energy of 737.2meV, which has a good agreement with a well-known value of EL2 defect emission activation energy of GaAs and AlGaAs [143–145]. Therefore, I would like to identify Peak3 as the GR noise due to the EL2 defect. This peak was affected by the nanoholes even though it is difficult to find a general trend of the effects of nanoholes on Peak 3.

In conclusion, we have learned that 1/f noise in the presence of the nanoholes decreases ***at most by 2 orders of magnitude compared to the reference sample***. This two order of magnitude decrease in 1/f noise comes from the combination of decrease in the Hooge parameter and the increase in the carrier density. The temperature dependent noise measurements carried out in the range of 85K-445K revealed the existence of four electronic defects. The defect with the highest activation energy of about 900meV is attributed to the presence of the nanoholes. Moreover, the noise signal related to the defect with the activation energy of 737meV, which is

considered as the EL2 center in this work, was reduced by the nanoholes. At the same time, the negligible changes in the noise signal related to the DX center were attributed to the nature of the defect and carrier kinetics related to GR process.

4.4. Current-Voltage Measurements

4.4.1. Theory

As explained in Section 4.1.2, Ohmic contacts require a small potential barrier at the metal-semiconductor junctions. On the other hand, Schottky contacts need a potential barrier to apply voltage to the devices without free current flow through the contacts. To achieve the barrier height which is required for different applications, it is important to understand physics behind the formation of the barrier at the contacts and current transport mechanisms.

The band formation is depicted in Fig. 4.20 for an n-type semiconductor and a metal whose work function is higher than that of the semiconductor. If a wire connects the metal and semiconductor electrically, electrons in the semiconductor will flow to the metal since they have higher energy in the semiconductor. As a result, a depletion layer is formed at the semiconductor surface. Since the semiconductor is n-type, a depletion layer is charged positively due to uncompensated donor ions. Hence, there are electrons accumulating on the suface of the metal, and the donor ions and the electrons on the surface of the metal create an electric field from the semiconductor to the metal which is accosicated with a potential difference at the contact. Since the concentraton of electrons in the metal is much higher than the doping density of the semiconductor, the depletion layer has an appreciable thickeness, and the energy band is bent up as in the case of p-n junctions [146].

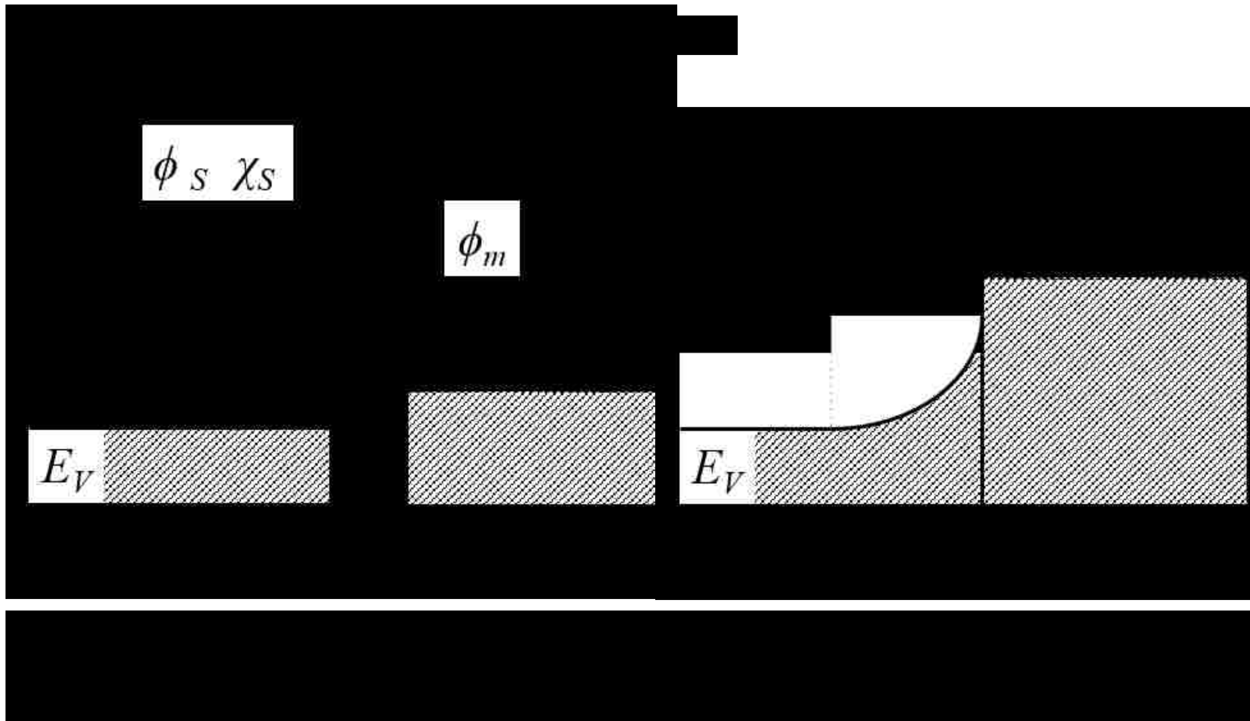

According to the Schottky model, the barrier hight relative to the Fermi level of the metal, ϕ_B, is given by

$$\phi_B = \phi_m - \chi_S \tag{4.28}$$

where ϕ_m is the work function of the metal and χ_S is the electron affinity of the semiconductor. The bending of the energy band is equal to the difference between the work functions of the metals and semiconductors. Thus, the potential barrier for the electrons in the semiconductor, V_{bi}, is

$$V_{bi} = \phi_m - \phi_S \tag{4.29}$$

where ϕ_S is the work function of the semiconductor. Unfortunately, it is experimentally observed that the Schottky barrier height does not follow Eq. 4.28 and 4.29 and is relatively independent of a choice of metal mainly due to effects of surface states and Fermi level pinning [6,146].

Under a forward applied bias condition, there are generally three transport mechanisms across a metal-n-type semiconductor contact as illustrate in Fig. 4.21. If electrons in the

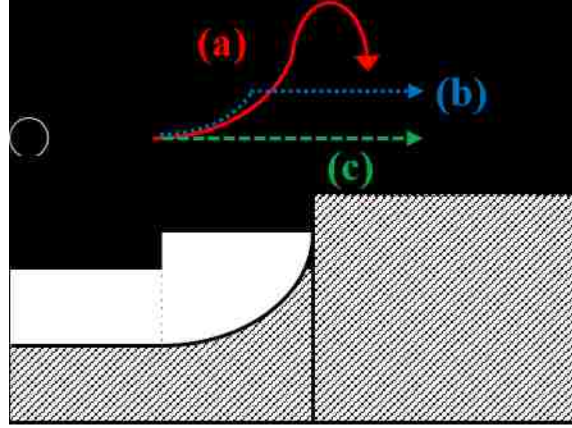

semiconductor have sufficient thermal energy, they transport over the top of the barrier. This transport mechanism is called thermionic emission and illustrated in Fig. 4.21(a). For a heavily doped semiconductor, the depletion layer is so narrow that the electrons penetrate the barrier by quantum mechanical tunneling. This transport mechanism is called field emission, and the combination of these two mechanisms, where the electrons are thermally excited to the middle of the barrier and then tunnel the barrier, is called thermionic-field emission (Fig. 4.21(c) and (b), respectively).

In the case of thermionic emission, the current, I_{TE}, is given by

$$I_{TE} = A_C A^* T^2 \exp(-\frac{\phi_B}{k_B T})(\exp(\frac{qV}{nk_B T}) - 1) = I_{S,TE}(\exp(\frac{qV}{nk_B T}) - 1) \tag{4.30}$$

where A_C is the area of the contact, A^* is the effective Richardson constant, T is the temperature, q is the electron charge, k_B is the Boltzmann constant, V is the applied voltage, n is the ideality factor, and

$$I_{S,TE} = A_C A^* T^2 \exp(-\frac{\phi_B}{k_B T}) \tag{4.31}$$

is the saturation current due to thermionic emission [6,146,147]. The difference between the traditional Richardson constant, A, and the effective Richardson constant, A^*, is the substitution of the effective mass of electrons, m^*, in the semiconductor instead of free electron mass. Thus, A^* is given by

$$A^* = \frac{4qm^* k_B^2 \pi}{h^3} \tag{4.32}$$

where h is the Planck constant. For n-type GaAs, A^*=8.03AK^{-2}cm^{-2} based on Eq. 4.32 using m^*=0.067m_0 where m_0 is the free electron mass [148].

In both thermionic-field and field emission, the electrons in the semiconductor are transported to the metal through the quantum mechanical tunneling. Since both mechanisms are governed by the same physical phenomenon, namely tunneling, the current can be described by the same equation. According to Padovani *et al.* and Crowell *et al.* [149,150], the tunneling current is of the form

$$I_{TFE} = I_{S,TFE} \exp(\frac{qV}{E_0})(1 - \exp(-\frac{qV}{k_B T})) \tag{4.33}$$

where

$$E_0 = E_{00} \coth(\frac{E_{00}}{k_B T}) \tag{4.34}$$

and

$$I_{S,TFE} = \frac{A_C A^* T^2 \exp(-\frac{q(E_C - E_F)}{k_B T})\{\pi E_{00}(\phi_B - (E_C - E_F))\}^{1/2}}{k_B T \cosh(E_{00}/k_B T)} \exp(-\frac{\phi_B - (E_C - E_F)}{E_0}) . \tag{4.35}$$

In these expressions, E_{00} is a characteristic energy and plays an important role in tunneling theory given by

$$E_{00} = \frac{q\hbar}{2}\left(\frac{N_d}{m^* \varepsilon_S}\right) = 1.99 \times 10^{-11}\sqrt{N_d} \qquad (4.36)$$

for n-type GaAs where $\hbar$ is the reduced Planck constant, N_d is the donor density, ε_S is the permittivity of the semiconductor. This characteristic energy determines which mechanism is dominant under certain conditions. As a rough guide, the dominant mechanism is thermionic emission if $k_B T \gg E_{00}$, thermionic-field emission if $k_B T \approx E_{00}$, and field emission if $k_B T \ll E_{00}$ [146].

4.4.2. Experimental Setup

For the I-V measurements, circular diode patterns with different diameter were fabricated on the surface of all samples using standard photolithography as explained in Section 4.1.3. These diode patterns have both Schottky and Ohmic contacts, so that this device works as Schottky diode. The details of the fabrication are summarized in Table 4.3, and a SEM picture of a typical circular diode structure is shown in Fig. 4.22.

The samples with the circular diode patterns were loaded into the MMR D2500 cryostat and kept in a vacuum achieved by a mechanical pump. I-V measurements were performed by a computer controlled system including Keithley source measure unit 236. Voltage was applied across the circular diode pattern with a radius of 700μm and swept between -2.5V to 2V, and current was measured at each 10mV. The temperature inside the cryostat was controlled by Joule-Thomson cooling using ultra-high purity N_2 gas and the heater controlled by MMR K-20

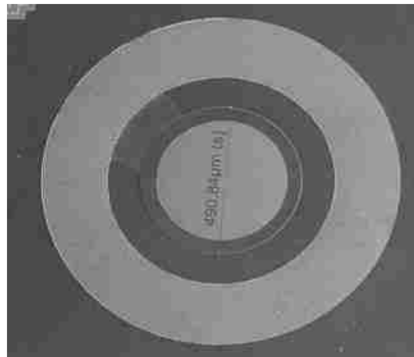

programmable temperature controller as described in Section 4.3.2. I-V characteristics were measured between 200K and 395K in steps of 15K.

TABLE 4.3. Details of lithography to fabricate circular diode structures for I-V measurements.

	Step Description	Details
1	Surface Cleaning	Acetone, Methanol, and IPA in 5mins each with ultrasonication
2	Photoresist Application	AZ4330 with 5000rpm (Thickness=3.4μm)
3	Baking	110°C for 3mins
4	Exposure	9.5s with a mask of Diode (Ohmic) for metallization
5	Development	AZ400K:H_2O (1:3) in 1min 45s
6	Etching	HCl:H_2O (1:1) for 15s (surface oxide)
7	Metallization	AuGe/Ni/Au (100nm/20nm/200nm)
8	Lift off	Acetone at 40°C for 40mins with ultrasonication
9	Annealing	390°C for 1min 30s under N_2 ambient
10	Photoresist Application	AZ4330 with 5000rpm (Thickness=3.4μm)
11	Baking	110°C for 3mins
12	Exposure	9.5s with a mask of Diode (Schottky) for metallization
13	Development	AZ400K:H_2O (1:3) in 1min 45s
14	Metallization	Ti/Au (200nm/200nm)
15	Lift off	Acetone at 40°C for 20mins with ultrasonication

4.4.3. Results and Analysis

Before analyzing results of I-V measurements, E_{00} should be calculated to check which transport mechanisms contribute electron transport in the measurements. Using $N_d=3\times10^{18}\text{cm}^{-3}$, which is the doping density for the GaAs cap layer, E_{00}=34.58meV from Eq. 4.36. Since k_BT=34.04meV even at 395K, the thermionic emission is probably dominant for the temperature range in which the measurements was conducted. However, the GaAs cap layer is just 2.5nm, and thus, the depletion layer probably reaches the doped AlGaAs layer. Since E_{00}=30.93meV for the AlGaAs barrier layer whose doping density is $2.4\times10^{18}\text{cm}^{-3}$, there may be some contribution in the current due to thermionic emission as well. Therefore, I will consider both currents due to thermionic-field and thermionic emission for the analysis of I-V measurements.

An example of I-V measurements for SF120, SF121, SF122, and SF123 in semi-long scale are shown in Fig. 4.23. For the entire temperature range, the I-V characteristics of all

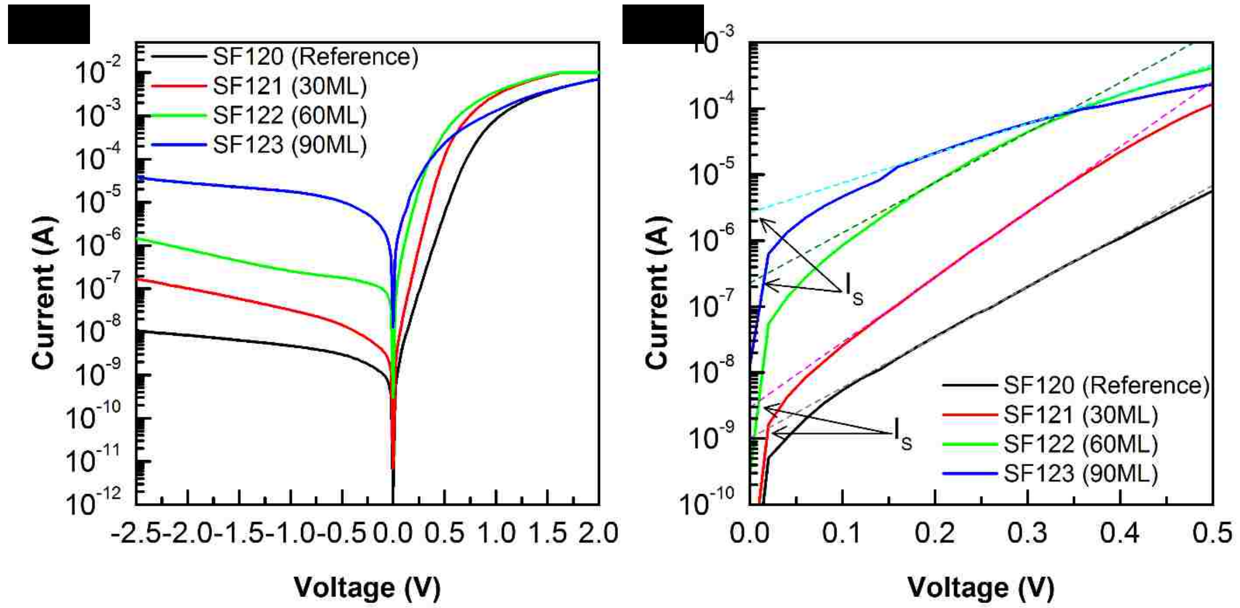

samples have similar features as shown in Fig. 4.23. In the forward bias, a linear I-V characteristic is observed in the low voltage range around 0.25V. According to Eq. 4.30, the current should be linear with a slope of q/nk_BT in the semilog scale for thermionic emission if $qV \gg k_BT$. If only thermionic-field emission is dominant, the current also is linear with a slope q/E_0 if $qV \gg k_BT$ from Eq. 4.33. Therefore, the linearity in the low voltage range stems from either thermionic or thermionic-field emission whichever is dominant at each temperature. The deviation from the linearity in high forward voltage range above 1V is caused by a series resistance from the contact resistance and the resistance of the device itself [93]. This series resistance causes non-negligible voltage drop at high current regime above 0.1mA.

In the reverse bias conditions, the thermionic emission is usually dominant since the depletion layer expands and the tunneling current is almost negligible [146]. In Fig. 4.23(a), the reverse bias currents clearly increase with the depth of nanoholes. If the reverse biased current is

mainly due to thermionic emission, the increases in the reverse current means the reduction of the Schottky barrier from Eq. 4.31. The results of the Hall effect and noise measurements showed that the nanoholes create a new deep level. If the deep level is present in the middle of the band gap of the semiconductor, the tunneling of the carrier with participation of the deep state can be enhanced, and thus, the Schottky barrier height and transport mechanisms will be affected. As a result, the reverse biased current increases although it is not clear if the lowering of the Schottky barrier height or the increase in the tunneling current due to the deep level increases for the case of reverse biased Schottky diode.

If the currents due to both thermionic and thermionic-field emission appear in the conduction across the Schottky contact, for $qV \gg k_B T$, the total current is expressed as

$$\begin{aligned} I &= C_{TE} I_{TE} + C_{TFE} I_{TFE} = C_{TE} I_{S,TE} (\exp(\frac{qV}{nk_B T} - 1)) + C_{TFE} I_{S,TFE} \exp(\frac{qV}{E_0})(1 - \exp(-\frac{qV}{k_B T})) \\ &\approx C_{TE} I_{S,TE} \exp(\frac{qV}{nk_B T}) + C_{TFE} I_{S,TFE} \exp(\frac{qV}{E_0}) \end{aligned} \tag{4.37}$$

where C_{TE}, C_{TFE} are arbitrary constants for thermionic current and thermionic field current, respectively. The saturation current at V=0 for the total current is determined by extrapolating the I-V plot in the semilog scale as in Fig. 4.23(b) and given by

$$I_S \approx C_{TE} I_{S,TE} + C_{TFT} I_{S,TFE} \tag{4.38}$$

assuming $E_0 \approx nk_B T$, where $I_{S,\,TE}$ and $I_{S,\,TFE}$ are given by Eq. 4.31 and 4.35, respectively.

Plots of I_S/T^2 versus 1000/T, which are called Richardson plots, for all samples are shown in Fig. 4.24. Then, these plots were fitted by using Eq. 4.38 with C_{TE}, C_{TFE}, and E_C-E_F as variables. The theoretically calculated values for A^* and E_{00}, and previously reported values for m^*, ϕ_B, and ε_S were used. The results of fitting are summarized in Table 4.4. It is quite difficult to find any meaningful trends in change of these parameters, but the Fermi level positions with

respect to the conduction band minimum are shifted, especially in SF121 and SF123. As explained in Section 4.4.1, the surface states affect the Schottky barrier formation through Fermi level pinning. If nanoholes affect the surface states, then the Fermi level is pinned at different energy. For these reasons, each sample has different Fermi levels. However, in order to validate this assumption, further characterization such as capacitance-voltage measurements and

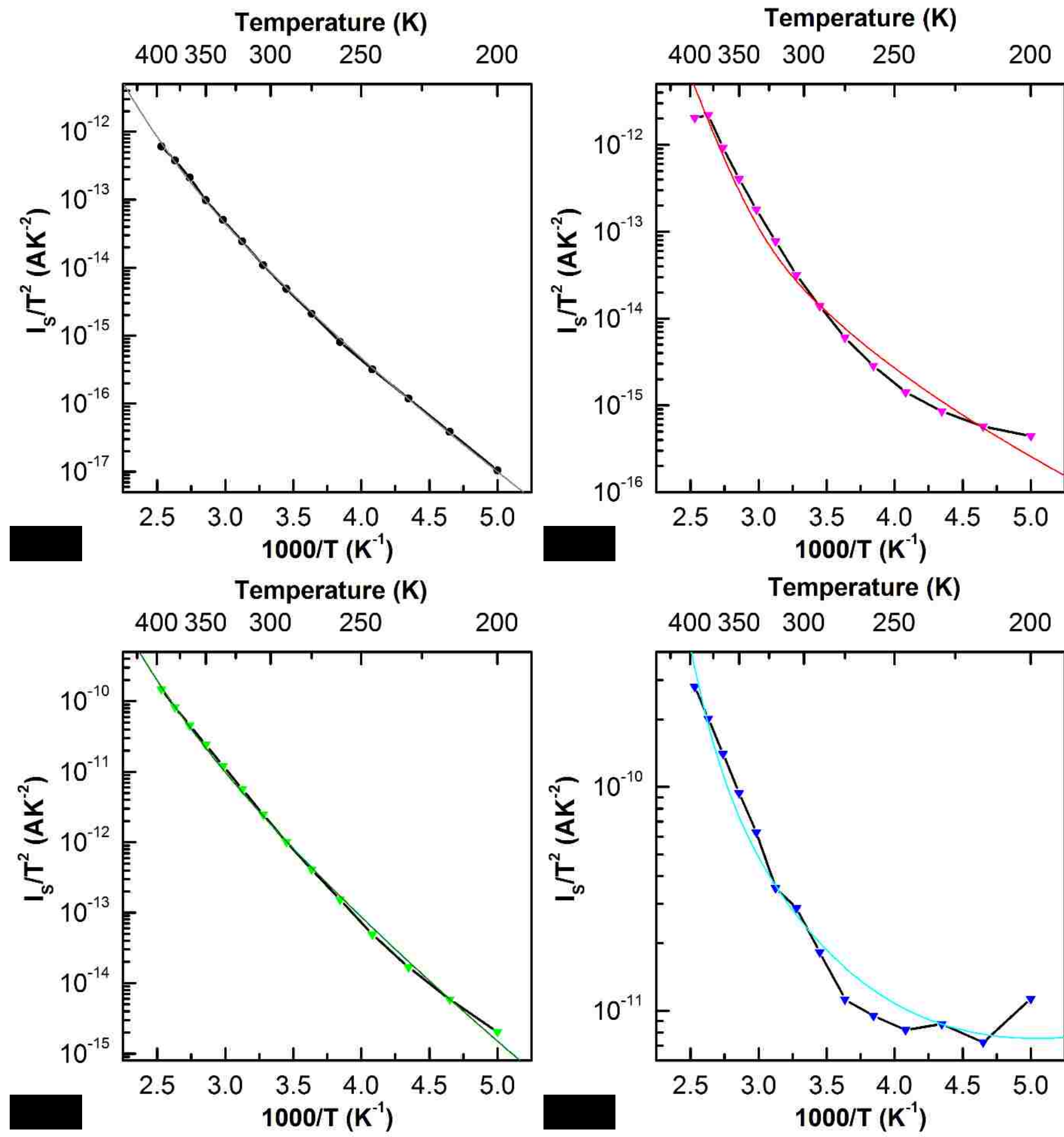

photocurrent measurements are required to measure the Schottky barrier height accurately. Moreover, we can measure I-V characteristic in different temperature ranges so that one of thermionic and thermionic field emission is dominant to make analysis simpler.

TABLE 4.4. Fitting parameters for all samples.

Sample Name	C_{TFE}	C_{TE}	C_{TE}/C_{TFE}	E_C-E_F
SF120	5.742×10^{-4}	0.2094	3.647×10^{3}	0.2582
SF121	1.877×10^{-4}	5.246	2.795×10^{4}	0.1133
SF122	0.1568	48.23	3.076×10^{3}	0.2780
SF123	1.743×10^{-2}	209.9	1.204×10^{4}	-0.0775

In conclusion of this section, it was found that the dark current measured in the reverse biased Schottky junction increases with the depth of the nanoholes compared to the reference sample. The analysis of the transport mechanism at the metal-semiconductor interface suggests the presence of both thermionic and thermionic field emission processes. These studies suggest that the nanoholes affect the transport mechanism at the Schottky junction. However, to obtain a more accurate picture, further detailed studies involving additional techniques, such as capacitance measurements, are required.

Chapter 5: Conclusion

Effects of nanoholes grown using droplet epitaxy on the InGaAs QWs were investigated for the first time by the temperature dependent Hall effect, noise, and I-V measurements. To fabricate the nanoholes with different depth but the same density, the growth conditions of the nanoholes were optimized. The results of the optimization confirm that the density of the nanoholes can be controlled by the growth temperature of the nanoholes while the depth of the nanoholes depends on the coverage of the Ga droplets. Using a solid source MBE, four InGaAs pseudomorphic QWs were prepared. One of them is just a QW without the nanoholes for the reference, and the other three have the nanoholes with different depth but similar density.

The temperature dependent Hall effect measurements were employed to measure the mobility and carrier density of the samples The samples with the nanoholes show higher mobility than the reference samples. The mobility of the samples decreases as the depth of the nanoholes increases, and the sample with the deepest nanoholes has almost the same mobility as the reference sample over the entire temperature range. The carrier density in the 2DEG increases with the depth of the nanoholes. The carrier density in the samples with the nanoholes is almost twice as that of the reference sample eve at 8K. The activation energy of the carriers was calculated from the slope of the Arrhenius plots of the carrier density for all samples and increases with the depth of the nanoholes.

Noise studies were carried out to study deep levels in the samples. Applied bias dependent noise studies at room temperature were conducted to calculate the Hooge parameter for all samples. The results of the room temperature noise study reveal that 1/f noise is suppressed in the samples with the nanoholes due to a decrease in the Hooge parameter and an increase in the carrier density.

The GR noise was examined using the temperature dependent noise studies. All four samples exhibit four distinct peaks between 85K and 445K. The contribution of Peak 2 stays the same for all samples, but Peak 3 is significantly suppressed in the samples with the nanoholes. Instead, Peak 4 is enhanced in the samples with the nanoholes. Based on the noise spectrum analysis at different temperature and frequencies, Peak 2 and Peak 3 are identified as the GR noise due to the DX center and EL2 center, respectively.

The temperature dependent I-V measurements were executed between 200K and 395K. The dark current in the reverse biased Schottky junction consistently increases with the depth of the nanoholes. An increase in the reverse current is attributed to the existence of a new deep level which possibly enhances the tunneling of the carriers at the metal-semiconductor interface. The analysis of the transport mechanism at the Schottky junction suggests the presence of both thermionic and thermionic field emission processes.

To explain physical mechanisms of the effects of the nanoholes on the 2DEG and the QW heterostructures, several hypotheses were proposed. The increase in the carrier density was attributed to the effects of the surface states. In addition, the possibilities of Ga metal left inside the nanoholes contributing to the increase in the carrier density were considered. The previously reported results showed that an increase in the carrier density lead to an increase in the mobility up to about $8\times10^{11}cm^{-2}$. Therefore, the increase in the mobility is associated with the increase in the carrier density. However, if the nanoholes are too deep and too close to the 2DEG, they cause more scattering and degrade the mobility. Furthermore, the results of the activation energy calculation, noise studies, and I-V measurements confirm that the nanoholes modify the energy spectrum of the samples.

What we have learned that is new from this research, based on these results and analysis, is that by simply introducing the nanoholes and controlling their depth, the mobility, carrier density, and the noise can be modulated. Moreover, the energy spectrum of the system can be engineered. To understand the physics behind the effects of nanoholes and to take advantage of the nanoholes to their fullest extent, additional research is required. For example, samples with passivated surface help to validate our hypothesis about the effects of the surface states to the increase in the carrier density. Also, the crystallization of the Ga droplets should be optimized to make sure there is no Ga left inside the nanoholes. Even with the set of the samples used in this thesis, additional characterization can provide more information about the effects of the nanoholes. Levinshtein *et al.* modified DLNS using band-to-band illumination to obtain the entire picture of the energy spectrum even in the case in which the Fermi level overlaps with the deep levels [130,131]. By illuminated DLNS, calculation of E_0 as well as E_1 of each deep level is possible. The Shubnikov-de Haas effects provide the most accurate measurements of the carrier density, which verify the validity of the Hall effect analysis. Additionally, optical characterization can provide further insights about effects of the nanoholes.

An alternative application of the nanoholes as well as modulation of material properties is described here. In this thesis, ***deep nanoholes whose depth is 34.72nm (SF123) were fabricated successfully for the first time.*** Hence, if the nanoholes are filled with metal, we can fabricate metal nanostructures on the surface. This new material system is quite interesting for plasmonic studies. Furthermore, we can expect to be able to control the dimensionality of the confinement of electrons if the nanoholes are growth at the interface between the gate electrode and the surface of field effect transistors. ***This is the direction of our future work***.

In conclusion, characterization of only depth dependent nanoholes, these results ensure that the nanoholes are promising for the modulation of material properties and can bring ideas for new types of devices.

Chapter 6: References

[1] J. Barden, in *Nobel Lect. Phys. 1942-1962* (Elsevier, Amsterdam, 1964).

[2] W. Shockley, IEEE Trans. Electron Devices **23**, 597 (1976).

[3] J. S. Kilby, IEEE Trans. Electron Devices **23**, 648 (1976).

[4] R. Hall, G. Fenner, J. Kingsley, T. Soltys, and R. Carlson, Phys. Rev. Lett. **9**, 366 (1962).

[5] R. D. Dupuis and M. R. Krames, J. Light. Technol. **26**, 1154 (2008).

[6] S. Sze, *Physics of Semiconductor Devices*, 2nd ed. (Wiley, New York, NY, 1981).

[7] S. Dimitrijev, *Principles of Semiconductor Devices*, 2nd ed. (Oxford University Press, New York, 2011).

[8] M. Henini and M. Bugajski, Microelectronics J. **36**, 950 (2005).

[9] P. Bhattacharya, S. Ghosh, and A. D. Stiff-Roberts, Annu. Rev. Mater. Res. **34**, 1 (2004).

[10] D. Bimberg and C. Ribbat, Microelectronics J. **34**, 323 (2003).

[11] A. van Die and J. I. Dijkhuis, J. Appl. Phys. **74**, 1143 (1993).

[12] Y. Haddab, B. Deveaud, H.-J. Bühlmann, and M. Ilegems, J. Appl. Phys. **78**, 2509 (1995).

[13] A. Rastelli, R. Songmuang, and O. . Schmidt, Phys. E Low-Dimensional Syst. Nanostructures **23**, 384 (2004).

[14] Z. M. Wang, K. Holmes, J. Shultz, and G. J. Salamo, Phys. Status Solidi **202**, R85 (2005).

[15] C. Heyn, C. Strelow, and W. Hansen, New J. Phys. **14**, 053004 (2012).

[16] J. Wu, Y. Hirono, X. Li, Z. M. Wang, J. Lee, M. Benamara, S. Luo, Y. I. Mazur, E. S. Kim, and G. J. Salamo, Adv. Funct. Mater. **24**, 530 (2014).

[17] B. Liang, Z. M. Wang, X. Wang, J. H. Lee, Y. I. Mazur, C.-K. Shih, and G. J. Salamo, ACS Nano **2**, 2219 (2008).

[18] C. Heyn, A. Stemmann, T. Köppen, C. Strelow, T. Kipp, M. Grave, S. Mendach, and W. Hansen, Appl. Phys. Lett. **94**, 183113 (2009).

[19] B. L. Liang, Z. M. Wang, J. H. Lee, K. Sablon, Y. I. Mazur, and G. J. Salamo, Appl. Phys. Lett. **89**, 043113 (2006).

[20] N. W. Strom, Z. M. Wang, J. H. Lee, Z. Y. AbuWaar, Y. I. Mazur, and G. J. Salamo, Nanoscale Res. Lett. **2**, 112 (2007).

[21] M. Henini, *Molecular Beam Epitaxy: From Research to Mass Production* (Elsevier Science, Amsterdam, 2012).

[22] C. T. Foxon, J. Cryst. Growth **251**, 1 (2003).

[23] A. Y. Cho and J. R. Arthur, Prog. Solid State Chem. **10**, 157 (1975).

[24] R. F. C. Farrow, *Molecular Beam Epitaxy - Applications to Key Materials* (Noyes Publications, Park Ridge, N.J., 1995).

[25] J. R. Arthur, Surf. Sci. **500**, 189 (2002).

[26] J. R. Arthur, J. Appl. Phys. **39**, 4032 (1968).

[27] A. Y. Cho, J. Appl. Phys. **41**, 2780 (1970).

[28] L. Esaki, Rev. Mod. Phys. **46**, 237 (1974).

[29] K. von Klitzing, Rev. Mod. Phys. **58**, 519 (1986).

[30] H. Stormer, Rev. Mod. Phys. **71**, 875 (1999).

[31] D. Tsui, Rev. Mod. Phys. **71**, 891 (1999).

[32] H. Kroemer, Rev. Mod. Phys. **73**, 783 (2001).

[33] Z. Alferov, Rev. Mod. Phys. **73**, 767 (2001).

[34] P. Grünberg, Rev. Mod. Phys. **80**, 1531 (2008).

[35] G. Tauber and H. Viefhaus, Vacuum **27**, 41 (1977).

[36] J. W. Robinson and M. Ilegems, Rev. Sci. Instrum. **49**, 205 (1978).

[37] K. Kanisawa, J. Osaka, S. Hirono, and N. Inoue, Appl. Phys. Lett. **58**, 2363 (1991).

[38] N. Inoue, M. Tanimoto, K. Kanisawa, S. Hirono, J. Osaka, and Y. Homma, J. Cryst. Growth **127**, 956 (1993).

[39] C. T. Foxon and B. A. Joyce, Surf. Sci. **50**, 434 (1975).

[40] E. S. Tok, J. H. Neave, J. Zhang, B. a. Joyce, and T. S. Jones, Surf. Sci. **374**, 397 (1997).

[41] J. A. Venables, G. D. T. Spiller, and M. Hanbucken, Reports Prog. Phys. **47**, 399 (1984).

[42] F. C. Frank and J. H. van der Merwe, Proc. R. Soc. A Math. Phys. Eng. Sci. **198**, 205 (1949).

[43] J. H. Neave, B. A. Joyce, P. J. Dobson, and N. Norton, Appl. Phys. A Solids Surfaces **31**, 1 (1983).

[44] I. N. Stranski and L. Krastanow, Sitzungsber. Akad. Wiss. Wien, Math.-Naturwiss. Kl., Abt. 2B **146**, 797 (1938).

[45] A. Ichimiya and P. I. Cohen, *Reflection High-Energy Electron Diffraction* (Cambridge University Press, New York, NY, 2004).

[46] Y.-W. Mo, D. Savage, B. Swartzentruber, and M. Lagally, Phys. Rev. Lett. **65**, 1020 (1990).

[47] D. Leonard, M. Krishnamurthy, C. M. Reaves, S. P. Denbaars, and P. M. Petroff, Appl. Phys. Lett. **63**, 3203 (1993).

[48] J. M. Moison, F. Houzay, F. Barthe, L. Leprince, E. André, and O. Vatel, Appl. Phys. Lett. **64**, 196 (1994).

[49] M. Grundmann, O. Stier, and D. Bimberg, Phys. Rev. B **52**, 11969 (1995).

[50] A. Fissel, R. Akhtariev, and W. Richter, Thin Solid Films **380**, 42 (2000).

[51] B. Daudin, F. Widmann, G. Feuillet, Y. Samson, M. Arlery, and J. Rouvière, Phys. Rev. B **56**, R7069 (1997).

[52] M. Volmer and A. Weber., Z. Phys. Chem. **119**, 227 (1926).

[53] N. Koguchi, S. Takahashi, and T. Chikyow, J. Cryst. Growth **111**, 688 (1991).

[54] N. Koguchi and K. Ishige, Jpn. J. Appl. Phys. **32**, 2052 (1993).

[55] K. Watanabe, N. Koguchi, and Y. Gotoh, Jpn. J. Appl. Phys. **39**, L79 (2000).

[56] R. a. Stall, J. Vac. Sci. Technol. B Microelectron. Nanom. Struct. **3**, 524 (1985).

[57] J. Osaka, N. Inque, Y. Mada, K. Yamada, and K. Wada, J. Cryst. Growth **99**, 120 (1990).

[58] A. Ohtake, Surf. Sci. Rep. **63**, 295 (2008).

[59] V. P. LaBella, M. R. Krause, Z. Ding, and P. M. Thibado, Surf. Sci. Rep. **60**, 1 (2005).

[60] S. Sanguinetti, K. Watanabe, T. Tateno, M. Gurioli, P. Werner, M. Wakaki, and N. Koguchi, J. Cryst. Growth **253**, 71 (2003).

[61] C. Heyn, A. Stemmann, A. Schramm, H. Welsch, W. Hansen, and Á. Nemcsics, Phys. Rev. B **76**, 075317 (2007).

[62] C. Heyn, A. Stemmann, A. Schramm, and W. Hansen, J. Cryst. Growth **311**, 1825 (2009).

[63] K. A. Jackson, *Kinetic Processes* (Wiley-VCH Verlag GmbH & Co. KGaA, Weinheim, FRG, 2004).

[64] Z. M. Wang, B. L. Liang, K. a. Sablon, and G. J. Salamo, Appl. Phys. Lett. **90**, 113120 (2007).

[65] A. Stemmann, C. Heyn, T. Köppen, T. Kipp, and W. Hansen, Appl. Phys. Lett. **93**, 123108 (2008).

[66] T. Mano, K. Watanabe, S. Tsukamoto, H. Fujioka, M. Oshima, and N. Koguchi, J. Cryst. Growth **209**, 504 (2000).

[67] Z. Y. Zhou, C. X. Zheng, W. X. Tang, J. Tersoff, and D. E. Jesson, Phys. Rev. Lett. **111**, 036102 (2013).

[68] Z. Gong, Z. C. Niu, S. S. Huang, Z. D. Fang, B. Q. Sun, and J. B. Xia, Appl. Phys. Lett. **87**, 093116 (2005).

[69] Z. M. Wang, K. Holmes, Y. I. Mazur, K. A. Ramsey, and G. J. Salamo, Nanoscale Res. Lett. **1**, 57 (2006).

[70] M. Yamagiwa, T. Mano, T. Kuroda, T. Tateno, K. Sakoda, G. Kido, N. Koguchi, and F. Minami, Appl. Phys. Lett. **89**, 113115 (2006).

[71] T. Mano, T. Kuroda, S. Sanguinetti, T. Ochiai, T. Tateno, J. Kim, T. Noda, M. Kawabe, K. Sakoda, G. Kido, and N. Koguchi, Nano Lett. **5**, 425 (2005).

[72] C. Somaschini, S. Bietti, S. Sanguinetti, N. Koguchi, A. Fedorov, M. Abbarchi, and M. Gurioli, IOP Conf. Ser. Mater. Sci. Eng. **6**, 012008 (2009).

[73] K. A. Sablon, J. H. Lee, Z. M. Wang, J. H. Shultz, and G. J. Salamo, Appl. Phys. Lett. **92**, 203106 (2008).

[74] J. H. Lee, K. Sablon, Z. M. Wang, and G. J. Salamo, J. Appl. Phys. **103**, 054301 (2008).

[75] J. H. Lee, Z. M. Wang, and G. J. Salamo, IEEE Trans. Nanotechnol. **8**, 431 (2009).

[76] J. S. Kim, M. Kawabe, and N. Koguchi, Appl. Phys. Lett. **88**, 072107 (2006).

[77] J. H. Lee, Z. M. Wang, K. Sablon, and G. J. Salamo, Cryst. Growth Des. **8**, 690 (2008).

[78] W. Ostwald, Z. Phys. Chem. Stoechiom. Verwandtschaftsl. **22**, 289 (1897).

[79] G. B. Galiev, I. S. Vasil'evskii, E. A. Klimov, S. S. Pushkarev, A. N. Klochkov, P. . Maltsev, M. Y. Presniakov, I. N. Trunkin, and A. L. Vasiliev, J. Cryst. Growth **392**, 11 (2014).

[80] D. J. Carrad, A. M. Burke, O. Klochan, A. M. See, A. R. Hamilton, A. Rai, D. Reuter, A. D. Wieck, and A. P. Micolich, Phys. Rev. B **89**, 155313 (2014).

[81] J. Schuster, T. Y. Kim, E. Batke, D. Reuter, and A. D. Wieck, J. Phys. Condens. Matter **24**, 165801 (2012).

[82] M. Daoudi, F. Hosni, N. Khalifa, I. Dhifallah, K. Farah, A. H. Hamzaoui, A. Ouerghi, and R. Chtourou, Phys. B Condens. Matter **440**, 113 (2014).

[83] G. Snider, (n.d.).

[84] G. Binnig and C. F. Quate, Phys. Rev. Lett. **56**, 930 (1986).

[85] J. Thornton, *SPM Training Notebook*, Rev. E (Veeco Instruments Inc., Plainview, NY, 2003).

[86] Anonymous, *Technical Specifications Sheet: Probe Model ACTA* (Applied nanoStructures, Inc., Mountain View, CA, 2013).

[87] Z. Wang and G. Salamo, Phys. Rev. B **67**, 125324 (2003).

[88] J. D. Plummer, M. Deal, and P. D. Griffin, *Silicon VLSI Technology: Fundamentals, Practice, and Modeling* (Prentice Hall, Upper Saddle River, NJ, 2000).

[89] F. Braun, Ann. Der Phys. Und Chemie **229**, 556 (1875).

[90] W. Schottky, Zeitschrift Für Phys. **118**, 539 (1942).

[91] D. Sodini, A. Touboul, G. Lecoy, and M. Savelli, Electron. Lett. **12**, 42 (1976).

[92] A. Goetzberger and R. M. Scarlett, *Research and Investigation of Inverse Epitaxial UHF Power Transistors : Technical Documentary Report* (NTIS Distributor, Palo Alto, CA, 1964).

[93] D. K. Schroder, *Semiconductor Material and Device Characterization*, 3rd ed. (John Wiley & Sons, Inc., Hoboken, NJ, USA, 2005), p. 800.

[94] D. C. Look, *Electrical Characterization of GaAs Materials and Devices* (Wiley, Chichester, NY, 1989).

[95] A. G. Baca and C. I. H. Ashby, *Fabrication of GaAs Devices* (Institution of Electrical Engineers, London, 2005).

[96] Anonymous, *Data Sheet of AZ4330* (Hoechst Celanese, n.d.).

[97] Y. Mori, J. Electrochem. Soc. **125**, 1510 (1978).

[98] W. Patrick, W. S. Mackie, S. P. Beaumont, and C. D. W. Wilkinson, Appl. Phys. Lett. **48**, 986 (1986).

[99] N. Braslau, J. B. Gunn, and J. L. Staples, Solid. State. Electron. **10**, 381 (1967).

[100] A. Zussman, J. Appl. Phys. **59**, 3894 (1986).

[101] M. Kniffin, J. Vac. Sci. Technol. A Vacuum, Surfaces, Film. **5**, 1511 (1987).

[102] E. H. Hall, Am. J. Math. **2**, 287 (1879).

[103] T. J. Seebeck, Ann. Phys. **82**, 1 (1826).

[104] A. v. Ettingshausen and W. Nernst, Ann. Der Phys. Und Chemie **265**, 343 (1886).

[105] G. E. Stillman and C. M. Wolfe, Thin Solid Films **31**, 69 (1976).

[106] P. Yu and M. Cardona, *Fundamentals of Semiconductors: Physics and Materials Properties*, 4th ed. (Springer, New York, 2010).

[107] C. J. Sandroff, R. N. Nottenburg, J.-C. Bischoff, and R. Bhat, Appl. Phys. Lett. **51**, 33 (1987).

[108] W. Walukiewicz, H. Ruda, J. Lagowski, and H. Gatos, Phys. Rev. B **30**, 4571 (1984).

[109] J. J. Harris, J. A. Pals, and R. Woltjer, Reports Prog. Phys. **52**, 1217 (1989).

[110] T. Ando, J. Phys. Soc. Japan **51**, 3900 (1982).

[111] T. Ando, Rev. Mod. Phys. **54**, 437 (1982).

[112] J. L. Thobel, L. Baudry, F. Dessenne, M. Charef, and R. Fauquembergue, J. Appl. Phys. **73**, 233 (1993).

[113] M. H. Somerville, D. R. Greenberg, and J. A. del Alamo, Appl. Phys. Lett. **64**, 3276 (1994).

[114] S. R. Lunt, G. N. Ryba, P. G. Santangelo, and N. S. Lewis, J. Appl. Phys. **70**, 7449 (1991).

[115] C. J. Sandroff, M. S. Hegde, L. a. Farrow, C. C. Chang, and J. P. Harbison, Appl. Phys. Lett. **54**, 362 (1989).

[116] N. Chand, T. Henderson, J. Klem, W. Masselink, R. Fischer, Y.-C. Chang, and H. Morkoĉ, Phys. Rev. B **30**, 4481 (1984).

[117] E. Schubert and K. Ploog, Phys. Rev. B **30**, 7021 (1984).

[118] D. C. Tsui and R. A. Logan, Appl. Phys. Lett. **35**, 99 (1979).

[119] D. C. Tsui, Appl. Phys. Lett. **38**, 550 (1981).

[120] E. Mendez, L. Esaki, and L. Chang, Phys. Rev. Lett. **55**, 2216 (1985).

[121] B. M. Wilamowski, *Fundamentals of Industrial Electronics* (CRC Press, Boca Raton, FL, 2011).

[122] J. Johnson, Phys. Rev. **32**, 97 (1928).

[123] H. Nyquist, Phys. Rev. **32**, 110 (1928).

[124] A. Einstein, Ann. Phys. **324**, 289 (1906).

[125] J. B. Johnson, Phys. Rev. **26**, 71 (1925).

[126] A. L. McWhorter, in *Semicond. Surf. Phys.*, edited by R. H. Kingdton (University of Pennsylvania Press, Philadelphia, PA, 1957), pp. 207–228.

[127] F. N. Hooge, Phys. Lett. A **29**, 139 (1969).

[128] F. N. Hooge, IEEE Trans. Electron Devices **41**, 1926 (1994).

[129] M. E. Levinshtein and S. L. Rumyantsev, Semicond. Sci. Technol. **9**, 1183 (1994).

[130] M. E. Levinshtein and S. L. Rumyantsev, Semiconductors **29**, 74 (1995).

[131] N. V Dyakonova, M. E. Levinshtein, and S. L. Rumyantsev, Semicond. Sci. Technol. **11**, 177 (1996).

[132] W. A. Little, Adv. Cryog. Eng. **35**, 1305 (1990).

[133] W. A. Little, Adv. Cryog. Eng. **35**, 1325 (1990).

[134] R. L. Paugh, Cryogenics (Guildf). **30**, 1079 (1990).

[135] Anonymous, *Operation Manual and Programming Reference: Model SR785 Dynamic Signal Analyzer*, 1.4 ed. (Stanford Research Systems, Sunnyvale, CA, 2006).

[136] V. P. Kunets, Micro-Hall Devices Based on High-Electron-Velocity Semiconductors, Humboldt-University, 2004.

[137] T. A. Morgan, Electronic Noise Spectroscopy of Indium Gallium Arsenide Quantum Dots, University of Arkansas, 2008.

[138] N. Andrushchak, Investigation of Negative Differential Resistance Phenomena in Quantum Well Heterostructures, University of Arkansas, 2012.

[139] P. M. Mooney, J. Appl. Phys. **67**, R1 (1990).

[140] P. M. Mooney, N. S. Caswell, and S. L. Wright, J. Appl. Phys. **62**, 4786 (1987).

[141] M. O. Watanabe, K. Morizuka, M. Mashita, Y. Ashizawa, and Y. Zohta, Jpn. J. Appl. Phys. **23**, L103 (1984).

[142] J. R. Kirtley, T. N. Theis, P. M. Mooney, and S. L. Wright, J. Appl. Phys. **63**, 1541 (1988).

[143] P. Alonso-González, D. Fuster, L. González, J. Martín-Sánchez, and Y. González, Appl. Phys. Lett. **93**, 183106 (2008).

[144] D. . Look and Z.-Q. Fang, Solid. State. Electron. **43**, 1317 (1999).

[145] P. A. Martin, K. Hess, M. Emanuel, and J. J. Coleman, J. Appl. Phys. **60**, 2882 (1986).

[146] E. Rhoderick and R. H. Williams, *Metal-Semiconductor Contacts*, 2nd ed. (Oxford University Press, New York, NY, 1988).

[147] E. H. Rhoderick, IEE Proc. I Solid State Electron Devices **129**, 1 (1982).

[148] I. Vurgaftman, J. R. Meyer, and L. R. Ram-Mohan, J. Appl. Phys. **89**, 5815 (2001).

[149] F. A. Padovani and R. Stratton, Solid. State. Electron. **9**, 695 (1966).

[150] C. R. Crowell and V. L. Rideout, Solid. State. Electron. **12**, 89 (1969).